

The impact of Holocene deglaciation and glacial dynamics on the landscapes and geomorphology of Potter Peninsula, King George Island (Isla 25 Mayo), NW Antarctic Peninsula

Pablo A. Heredia Barión^{1,2,3}, Jorge A. Strelin^{3,4}, Stephen J. Roberts^{5*}, Cornelia Spiegel², Lukas Wacker⁶, Samuel Niedermann⁷, Michael J. Bentley⁸, Emma J. Pearson⁹, Nadia T. Manograsso Czalowski^{10,11}, Sarah J. Davies¹¹, Bernhard Schnetger¹², Martin Grosjean¹³, Stephanie Arcusa¹³, Bianca Perren⁵, Emma P. Hocking¹⁴, Gerhard Kuhn^{1,2}

¹Alfred-Wegener-Institut Helmholtz-Zentrum für Polar- und Meeresforschung, Geosciences Division, Am Alten Hafen 26, 27568 Bremerhaven, Germany.

²University of Bremen, Department of Geosciences, Klagenfurter Str. 2-4, 28359 Bremen, Germany.

³Centro de Investigaciones en Ciencias de la Tierra (CONICET-UNC), Vélez Sársfield 1611, X5016GCA, Córdoba, Argentina.

⁴Instituto Antártico Argentino, Convenio MREC - Universidad Nacional de Córdoba, Vélez Sársfield 1611, X5016GCA, Córdoba, Argentina.

⁵British Antarctic Survey (BAS), Natural Environmental Research Council (NERC), High Cross, Madingley Road, Cambridge CB3 0ET, UK.

⁶ETH Zürich, Laboratory of Ion Beam Physics, Schafmattstr. 20, 8093 Zürich, Switzerland.

⁷Deutsches GeoForschungsZentrum GFZ, Telegrafenberg, 14473 Potsdam, Germany.

⁸Department of Geography, Durham University, Durham DH1 3LE, UK.

⁹School of Geography, Politics and Sociology, Newcastle University, Newcastle-upon-Tyne, NE1 7RU, UK.

¹⁰Instituto Antártico Argentino (I.A.A.), Av. 25 de Mayo. San Martín. Provincia de Buenos Aires (CP1650), Argentina.

¹¹Aberystwyth University, Department of Geography and Earth Sciences, Aberystwyth, SY23 3DB, UK.

¹²Institute for Chemistry and Biology of the Marine Environment (ICBM), Carl-von-Ossietzky-Str. 9-11, 26133 Oldenburg, Germany.

¹³Institute of Geography and Oeschger Centre for Climate Change Research, University of Bern, Switzerland.

¹⁴Department of Geography, Northumbria University, Ellison Building, Newcastle-upon-Tyne NE1 8ST, UK.

*Corresponding author: Stephen J. Roberts (sjro@bas.ac.uk)

This is a pre-print version of a paper published in *Frontiers in Earth Science*

<https://doi.org/10.31223/X5606J>

The final version may be different and will be available via the peer-reviewed publication doi link and in EarthArXiv <https://eartharxiv.org/repository/view/4587/>

We welcome all comments and feedback, posted on EarthArXiv or sent to the corresponding author, Stephen Roberts (sjro@bas.ac.uk).

Abstract

The timing and impact of deglaciation and Holocene readvances on the terrestrial continental margins of the Antarctic Peninsula have been well-studied but are still debated. Potter Peninsula on King George Island (Isla 25 de Mayo), South Shetland Islands (SSI), NW Antarctic Peninsula has a detailed assemblage of glacial landforms and stratigraphic exposures for constraining deglacial landscape development and glacier readvances. We undertook new morphostratigraphic mapping of the deglaciated foreland of the Warszawa Icefield, an outlet of the Bellingshausen (Collins) Ice Cap on Potter Peninsula, using satellite imagery and new lithofacies recognition and interpretations, combined with new chronostratigraphic analysis of stratigraphic sections, lake sediments, and moraine deposits. Results show that deglaciation on Potter Peninsula began before c. 8.2 ka. Around c. 7.0 ka, the Warszawa Icefield and the marine-facing Fourcade Glacier readvanced across Potter Peninsula and to the outer part of Potter Cove. Evidence of further readvances on Potter Peninsula is then absent until the Warszawa Icefield margin was landward of its present position on three occasions, c. 1.7–1.4 ka, after c. 0.7 ka (most likely c. 0.5–0.1 ka), and by 1956 CE. The timing of Holocene deglaciation and glacier fluctuations on Potter Peninsula are broadly coeval with other glacier- and ice-free areas on the South Shetland Islands and the northern Antarctic Peninsula, and likely driven by interactions between millennial-to-centennial-scale changes in solar insolation and irradiance, the southern westerlies, and the Southern Annular Mode.

Keywords

Deglaciation; geomorphological mapping; radiocarbon dating; South Shetland Islands; stratigraphy; glacier readvance

1. Introduction

The average annual temperature of the northern Antarctic Peninsula (AP) and South Shetland Islands (SSI) region (Figure 1A) has increased by almost 3°C (from -2.5 °C) since the middle of the last century (Vaughan et al., 2003; Meredith and King, 2005; Turner et al., 2016), exceeding average global warming by ~1.5-1.8°C (Sánchez-Lugo et al., 2018; Kaufman et al., 2020), leading to enhanced ice sheet thinning, glacier retreat, and permafrost thawing (Steig et al., 2009; Serrano et al., 2012; Vaughan et al., 2013; Bockheim et al., 2013; Osmanoglu et al., 2013).

Past ice sheet, ice cap, and outlet glacier behaviour provides important long-term context for recent changes and allows us to assess of whether current rates of change are beyond the range of natural variability (Bentley et al., 2014). During the global Last Glacial Maximum (g-LGM; 23-19 cal. ka BP – calibrated radiocarbon age in thousands of years before present – Hughes et al. (2013)), the

AP ice sheet extended towards the shelf edge and a secondary, smaller ice cap covered the northwest AP/SSI region, reaching the outer continental shelf ~50 km north of its present location in the inner fjords of Maxwell Bay, King George Island (KGI), SSI (Figure 1B, 1C) (John and Sugden, 1971; Curl, 1980; Ó Cofaigh et al., 2014; Nývlt et al., 2020). Deglaciation on KGI began broadly after 15.4 ± 2.5 ka (Seong et al., 2008) and Maxwell Bay was deglaciated between c. 14.8 and 14.1 cal. ka BP as the LGM ice sheet decoupled from the sea floor (Simms et al., 2011) and became ice-free by 9.1 cal. ka BP (Simms et al., 2011; Watcham et al., 2011). On land, lakes formed in deglaciated ice-free areas above the Holocene marine limit at ~16 m above present mean sea-level (henceforth, m a.s.l.) on Fildes and Barton Peninsula provide minimum age constraints on deglaciation at, or before, c. 8.1 ka (Watcham et al., 2011; Oliva et al., 2019).

While the deglaciation of the AP and SSI by Termination 1 (the start of the Holocene at 11,700 years b2k – before CE 2000; Gibbard and Head, 2020) has been broadly established (Ó Cofaigh et al., 2014), more field data from glacier-free terrestrial areas of the northern AP continental margin are required to assess how natural warming during the transition into the current (Holocene) interglacial drove further local-regional deglaciation, and how millennial-centennial scale changes in climate during the Holocene impacted glacier dynamics (Spada et al., 2013; Bentley et al., 2014). Furthermore, evaluating the sensitivity of small ice caps and outlet glaciers of the AP and SSI to smaller-scale amplitude atmospheric and oceanographic forcing during the Holocene is of particular importance for constraining past rates of grounding-line retreat and relative sea level (RSL) change (Hall, 2007; Bentley et al., 2014; Johnson et al., 2022).

Changes in the behaviour of the Bellingshausen (Collins) Ice Cap (BIC) on King George Island/Isla 25 de Mayo (KGI), the largest island and ice cap in the SSI archipelago, can be constrained using field evidence from its deglaciated peninsulas, such as Potter Peninsula (Figure 1C, 2). Detailed geomorphological mapping and establishing robust chronologies for geomorphological landforms, stratigraphic sections and lake sediments from glacier- and ice-free areas on these peninsulas can help refine existing models of AP and SSI continental margin deglaciation and allow us to examine the impacts and underlying mechanisms of post-LGM deglaciation and outlet/tidewater glacier readvance(s).

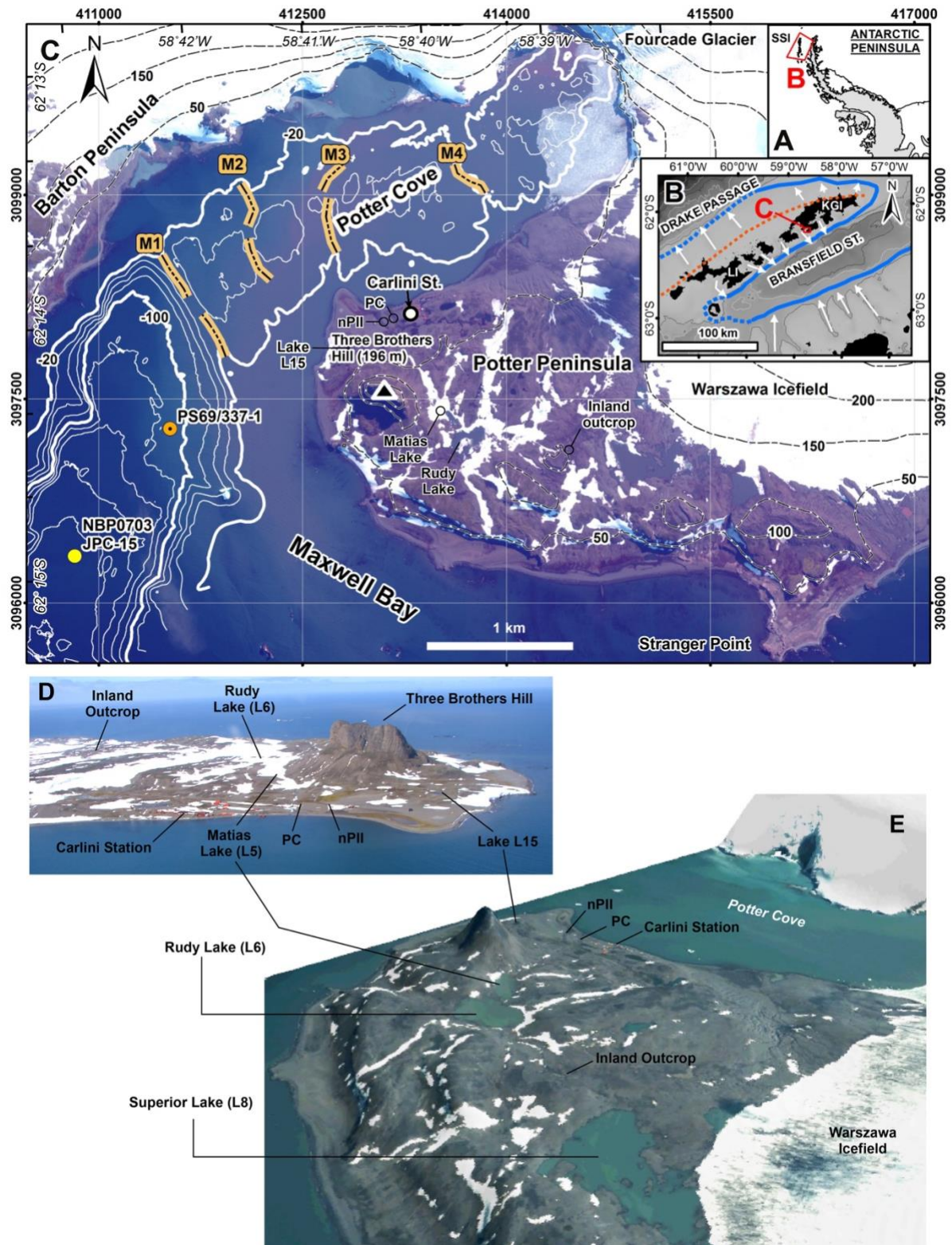
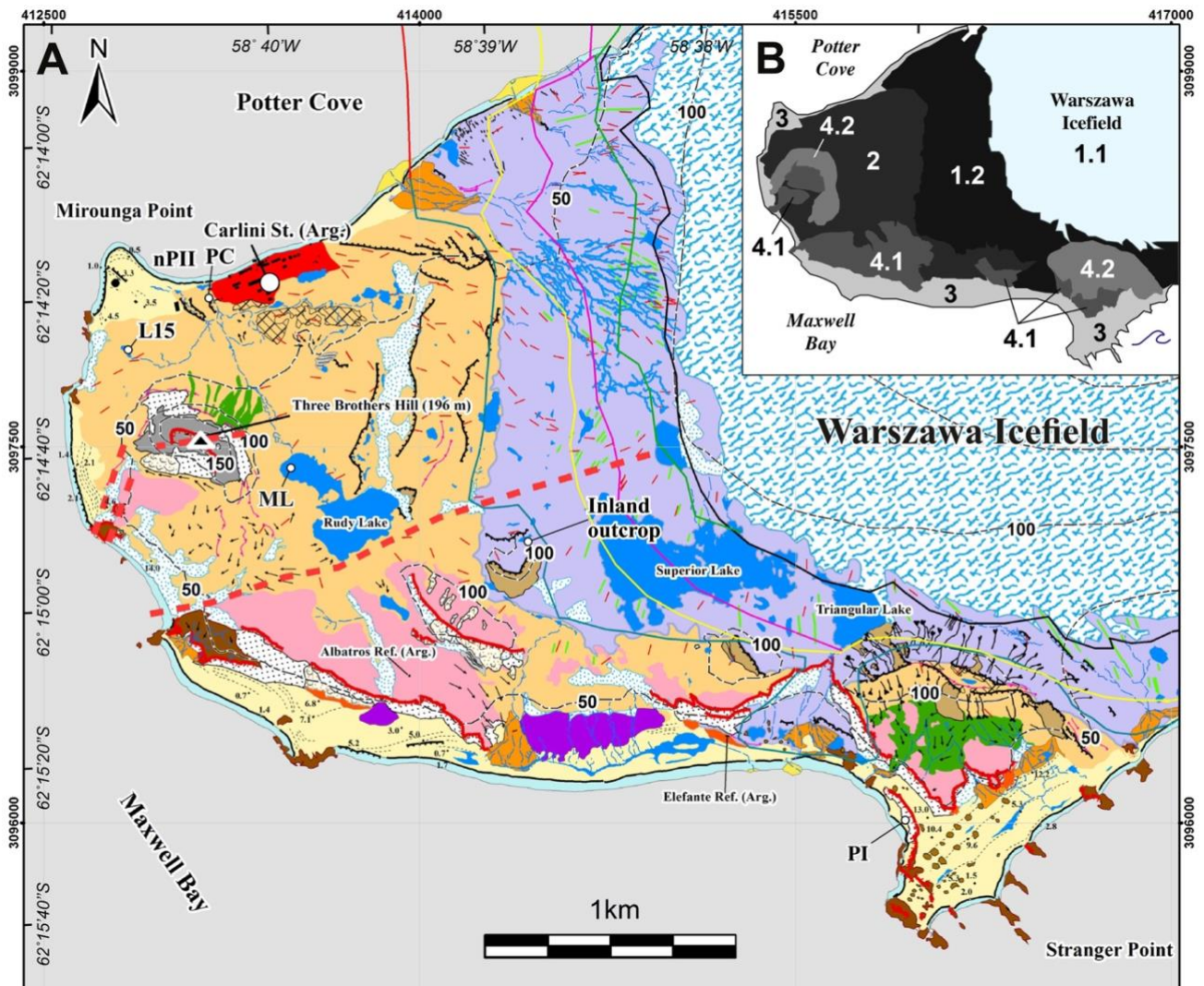


Figure 1. Location and geographic context of the study area. (A) Location of the South Shetland Islands (SSI) and (B) King George Island (KGI) and Livingston Island (LI). Bathymetric contours every 500 m (Weatherall et al., 2015). Note the extension of the LGM ice cap (blue full and dotted line) and its axis (red dotted line; after Simms et al., 2011). (C) Location and topography of Potter Peninsula and bathymetry of Potter Cove (adapted from Deregibus et al., 2015) and the positions of sedimentary cores and the position of moraine complexes (NBP0703_JPC-15, Majewski et al., 2012; PS69/337-1, Wöfl et al., 2016). Moraine complex M4 represents the position of Fourcade Glacier in 1956 (Wöfl et al., 2016). The position of the ice front on land in 1956 CE is also shown in Figures 2 and 3. New stratigraphic sections excavated in this study are nPII, PC and the ‘Inland Outcrop’; new lakes cored are Matias Lake (L5) and Lake L15. Projection used is an equal

area/distance UTM coordinate system based on the WGS84 ellipsoid (zone 21E) to minimise distortion over short distances. (D) Oblique view of Potter Peninsula looking towards Three Brothers Hill (image taken in 02/2008 by Peter Fretwell). (E) 3D-DEM drape of the satellite image looking approximately west from the Warszawa Icefield across the deglaciated landscape of Potter Peninsula (scene ID: 1010010004C1B200; pixel resolution 0.67 m; Maxar Products. Quickbird satellite image acquired 16/01/2006 © 2022 Maxar technologies). The positions of the new stratigraphic sections nPII, PC, and the ‘Inland Outcrop’, and lakes L5 (Matias Lake) and L15 examined in this study are shown. Superior Lake (L8) and Rudy Lake (L6) are also shown for orientation.

In common with other deglaciated peninsulas bordering Maxwell Bay (e.g., Oliva et al., 2019; Oliva et al., 2020) and across the northern Antarctic Peninsula (Ruiz-Fernández et al., 2019), Potter Peninsula is covered by till and other glacial, periglacial, proglacial, and paraglacial morphostratigraphic deposits, containing datable organic remnants (Sugden and John, 1973; Birkenmajer, 1998; Ballantyne, 2002; Ruiz-Fernández et al., 2019). Fourcade (1960), González-Ferrán and Katsui (1970), John and Sugden (1971), Sugden and John (1973) and Birkenmajer (1998) undertook pioneering work on Potter Peninsula, published geomorphological sketch maps and reconstructed its glacial history, yet no comprehensive and up-to-date geomorphological synthesis exists. Moreover, in recent decades, the retreat of BIC glacier outlets has exposed new coastlines, landforms and stratigraphic exposures, and a new assessment of the landform assemblages and their chronologies is now required.

Here, we present a new geomorphological synthesis for Potter Peninsula comprising of the first comprehensive geomorphological map constructed using satellite imagery and digital mapping techniques and new chronological data from sediment-landform assemblages recording glacier fluctuation on Potter Peninsula (Figure 2, 3). We test the hypothesis that Holocene deglaciation on Potter Peninsula from offshore LGM limits was a continuous process, and combine all available evidence to answer the following questions: 1) When did the deglaciation of Potter Peninsula begin? 2) Did readvances from the Warszawa Icefield occur and what was their extent? 3) What were the wider regional–global drivers and impact of deglaciation and glacier readvance(s) on Potter Peninsula and the SSI?



Lithology

- Bedrock (basalts and andesites)
- Columnar jointed volcanic conduit

Tectonics and structural landforms

- Rock scarp
- Fault (Kraus and del Valle, 2008b)

Glacial landforms and deposits

- Glacier (2013 CE limit)
- Vegetated till/glacial deposit
- Poorly/non-vegetated till/glacial deposit
- Morainic crest
- Till ridge
- Flute
- Stria

Periglacial and nival landforms and deposits

- Frost shattered rock/debris covered by lichens
- Protalus lobe
- Stone sorted circles and polygons
- Snow bank
- Solifluction lobes
- Stone stripe
- Mudflow

Hillslope landforms and deposits

- Talus accumulation
- Landslide
- Resedimented till as debris flow
- Cliff
- Rockfalls

Marine landforms and deposits

- Raised beach
- Present day beach
- Delta
- Beach ridge
- Active berm
- Elevation in m a.s.l.

Alluvial landforms and deposits

- Alluvial fan
- Inactive alluvial zone/fan

Anthropogenic landforms and deposits

- Building/refuge/heliport
- Zone of high anthropogenic impact

Biological landforms and deposits

- Penguin mound

Hydrography

- Lake
- Streams in V-shaped valley
- Stream
- Sea

Position of ice front

- Inland ice front (1956) from aerial photographs (see Fig. 3A)
- Ice front (2008)
- Ice front (2000)
- Ice front (1995)
- Ice front (1988)
- Ice front (1956) after Rückamp et al. (2011)

Figure 2. (A) Geomorphological map of Potter Peninsula showing landform assemblages in the main text and the location of key sites in this study: nPII = new Pingfo II section; PC = Potter Cove section (Sugden and John, 1973) and new Potter Cove section; L15 = Lake L15, ML = Matias Lake, connected to Rudy Lake. PI is the Pingfo I section (del Valle et al., 2002). (B) Summary map of landform assemblage zones 1-4, subdivided as follows: 1.1) Glacier and snow assemblage; 1.2) Active glacial and proglacial sediment landform assemblage (deglaciated since 1956 CE); 2) Moss and lichen vegetated inactive glacial landforms and deposits, including till deposits and inactive glaciofluvial fans, deglaciated before 1956 CE; 3) Paraglacial assemblage: Glaciomarine and glaciofluvial landforms and deposits, including raised beaches, deltas and active (proglacial) glaciofluvial fans; 4.1) Periglacial assemblage, nival landforms and deposits; 4.2) Hillslope landforms and deposits, including redeposited till. These zones are referred to in the results section and Table 1. The geomorphological map of Potter Peninsula was constructed by comparing geomorphological features identified and interpreted in the field with the study of a high resolution WorldView2, DigitalGlobe satellite image (scene ID: 103001001F612100; pixel resolution 0.5 m; Maxar Products. Quickbird satellite image acquired 07/03/2013 © 2022 Maxar technologies). Topography is based on the King George Island digital elevation model (KGI-DEM) with a spatial resolution of 3 m pixel-1 (Kraus and del Valle, 2008b), with georeferenced landforms mapped from their surveyed localities. The mapping projection used in (A) was an equal area/distance UTM coordinate system based on the WGS84 ellipsoid (zone 21E) which minimises distortion over short distances within a single UTM zone at the poles.

2. Geology, climate, and glaciological setting of Potter Peninsula

2.1 Study area and geology

Potter Cove is an inner fjord of Maxwell Bay, bordering the Fourcade Glacier, a marine-terminating glacier located on the northeastern side of the fjord (Figure 1C). The Warszawa Icefield to the south of the Fourcade Glacier defines the eastern border of the deglaciated Potter Peninsula (Figure 1C). Both glaciers are outlets of the BIC (Collins Ice Cap) that covers approximately 90% of the surface of KGI, to a maximum thickness of about 400 metres (Blindow et al., 2010). Aerial and satellite imagery shows that the Warszawa Icefield and the Fourcade Glacier retreated rapidly between 1956 and 2013 CE, with ~40 % of the present-day deglaciated area of Potter Peninsula becoming ice-free during that time (Figure 3).

Lava flows, pyroclastic rocks and related hypabyssal intrusives are exposed on Potter Peninsula and the basalts of the peninsula have been potassium-argon dated at 49 ± 1 to 42 ± 1 Ma (Smellie et al., 1984; Kraus and del Valle, 2008a, b). Three Brothers Hill (196 m a.s.l.), an andesitic plug with transverse faults and columnar jointing, formed during the final stages of a Palaeogene stratovolcano and is the most prominent topographic feature on Potter Peninsula (Figure 1D, E) (Birkenmajer 1998).

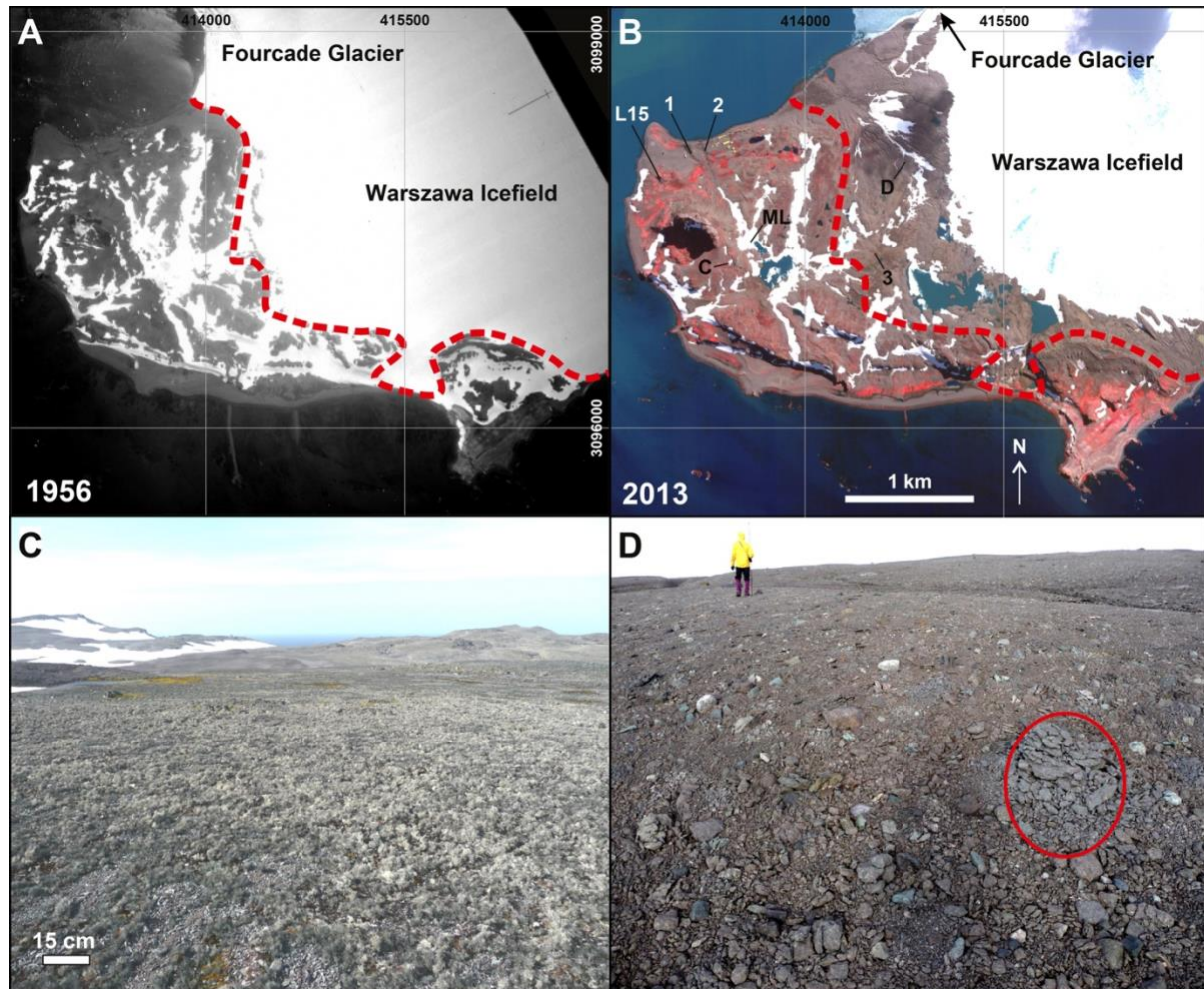


Figure 3. (A) Comparison between the positions of the tidewater Fourcade and inland Warszawa glaciers in 1956 CE (aerial photograph) and B) 2013 CE (satellite image). Due to the extended snow cover season, locating the position of the terrestrial glacier margin is challenging and retreat limits should be viewed as maxima. (B) Composite satellite image (NIR-G-B) of Potter Peninsula in 2013 with red areas reflecting the vegetation cover (mostly lichens). (C) and (D) Vegetated and recently deglaciated glacial deposits, respectively, of the glacial landform assemblages. Note the action of freeze-thaw processes causing laminated cracking in pyroclastic lithologies (red circle in D). In (A) and (B) Stratigraphic sections and new lake records are labelled as follows: 1 = new Pingfo II, 2 = new “Potter Cove” section, 3 = Inland glacial deposits, L15 = Lake L15, ML = Matias Lake. See Figs. 5, 6 and 7 for stratigraphic profiles. The locations of photographs shown in Figure 3C, and 3D are marked. To infer the area deglaciated in recent decades, we used an orthorectified panchromatic aerial image of 1956 CE (Falkland Island Dependency Aerial Survey Expedition, FIDASE; image ID X26FID0039076; pixel resolution 0.9 m; acquired 1956/12/20).

2.2 Climate

The mean annual air temperature on KGI between 1948 and 2011 CE was -2.5°C and Austral summer temperatures are often above zero (Kejna et al., 2013). A warming trend observed since the 1950s has paused, with a slight cooling occurring between 1999 and 2015 CE (Oliva et al., 2017). In contrast to the high interior atmospheric pressure of the West and East Antarctic plateau, climate of the northern AP and SSI is influenced by the mid-latitude and/or the polar atmospheric cells (Bentley et al., 2009). Atmospheric cells and the Southern Hemisphere Westerly winds (SHW)

bring warm and moist air masses formed at lower latitudes over the surrounding oceans and ~ 1000 mm yr⁻¹ of precipitation (Turner et al., 2002; Bentley et al., 2009; Falk et al., 2018), which drives snow accumulation, glaciofluvial erosion, and surface- and groundwater discharge into Potter Cove (Falk and Silva-Busso, 2020). Potter Peninsula becomes largely snow-free during the Austral spring/summer, but ephemeral snow patches persist well into late summer. The wind flow in Potter Cove is predominantly from SW to NW with a mean annual wind speed of ~ 15 m s⁻¹, and a weaker katabatic component (Falk et al., 2018).

Between 1996–2005 CE, increased cyclonic activity in the Drake Passage associated with more poleward-focused SHW and an increasingly more positive phase of Southern Annular Mode (SAM), drove sea-ice poleward, increasing the advection of warm air across southern Patagonia, the northern AP and SSI during winter (Kaplan et al., 2016, 2020; Oliva et al., 2017; Marshall et al., 2017; Reynhout et al., 2019). Conversely, between 2006–2015 CE colder winters pushed sea ice north, increasing snowfall across the northern AP and doubling snow cover on some SSI islands between 2009 and 2014 CE (Oliva et al., 2017; de Pablo et al., 2017).

The SAM is the primary mode of interannual and decadal to centennial scale atmospheric circulation variability in the Southern Ocean and reflects the zonal mean sea level pressure difference between Antarctica ($>65^\circ\text{S}$) and the mid latitudes (40°S) (Marshall, 2007; Moreno et al., 2018; Kaplan et al., 2020). The SAM index is a measure of the longitudinal mean SHW strength, with positive phases characterised by stronger, and poleward-shifted SHW (Marshall, 2007; Charman et al., 2018; Kaplan et al., 2020). Negative phases are characterised by generally colder, and in some places, more humid conditions, and weaker (and/or more diffuse), possibly equatorward shifted SHW (Marshall, 2007).

Interactions between the SAM and a deepening Amundsen Sea low during positive SAM phases can also bring warmer air from the Atlantic and north-easterly winds with cooler air from the Weddell Sea gyre, leading to colder/wetter conditions on the northern AP and low-lying SSI and increased glacier mass (Liu et al., 2005; Thomas et al., 2008; Goodwin et al., 2016; Oliva et al., 2017; Falk et al., 2018; Kaplan et al., 2020). These processes are intensified further in the Pacific sector that feeds the Antarctic Peninsula by interactions between SAM and the (sub)decadal-scale El Niño Southern Oscillation (ENSO). Positive (enhanced) phases of ENSO (El Niño) drive warmer interannual global mean temperature variability and negative phases of the SAM (Wang and Cai, 2013; Turner et al., 2016). Decadal scale variability in temperature measured at stations on the AP and SSI has been linked to changes in ENSO (Oliva et al., 2017).

2.3 Glaciological setting

Observations, numerical simulations and ground-penetrating radar data indicate that the BIC is a partly temperate ice cap, with cold ice at higher elevations and temperate ice at lower elevations (Blindow et al., 2010; Rückamp et al., 2010, 2011). The Warszawa Icefield margin is a polythermal, debris-covered glacier and ice-cored and thrust moraines can be found at Stranger Point (Figure 2A). Increased precipitation on the western AP over the last five decades (Thomas et al., 2008; Goodwin et al., 2016) has resulted in a slightly positive glacier mass balance on northern AP islands and the SSI overall (Oliva et al., 2017). From 1970–90 CE, the BIC had a stable to slightly negative glacier mass balance and an equilibrium line altitude (ELA) at ~ 150 m a.s.l. (Curl, 1980, Turner et al., 2002; Bentley et al., 2009; Falk et al., 2018). By 2015 CE, the ELA had risen to ~260 m a.s.l. and glacier flow rates had accelerated (Falk et al., 2018). Across the SSI, permafrost is discontinuous between 0 and 30 m a.s.l. Colder conditions between ~30 and 50 m a.s.l. favour the formation of continuous permafrost. Above 50 m a.s.l., permafrost dominates periglacial processes, but permafrost is less common above 90 m a.s.l. (Serrano et al., 2012; Oliva et al., 2020).

The deglaciation of Potter Peninsula left behind numerous glacial landforms. Inland moraines are surrounded by a coastal environment with older (Holocene-age) raised beaches and marine deposits (John and Sugden, 1971; Lindhorst and Schutter, 2014; Heredia Barión et al., 2019). Holocene relative sea level (RSL) curves for the SSI are more complex than in other locations on the AP, and several different RSL curves have been constructed (Pallàs et al., 1997; Bentley et al., 2005; Hall, 2010; Roberts et al., 2011; Watcham et al., 2011; Simms et al., 2012; 2021; Johnson et al., 2022). Bentley et al. (2005), and Johnson et al. (2022) thereafter, proposed an early-mid Holocene marine limit of ~16–18 m a.s.l. for the SSI. Based on the ages of marine-freshwater transitions and altitude of isolation basins on nearby Fildes Peninsula, Watcham et al. (2011) built on pioneering work Mäusbacher et al. (1989) and refined this to a more conservative estimate of ~16 m a.s.l. On Potter Peninsula, del Valle et al. (2002) constrained the onset of the deglaciation and raised beach formation between 17.1–14.4 m a.s.l. at Stranger Point (Pingfo-I, PI in Figure 2) with a minimum age of 5.5–5.4 cal. ka BP from elevated coastal sediments, although Fretwell et al. (2010) and Lindhorst and Schutter (2014) later revised the maximum raised beach altitude on Potter Peninsula to 12.2 m a.s.l.

There are several low altitude sedimentary sections close to present day sea level along the south side of Potter Cove are ~200 m west of the Argentinian Carlini station, ~2 km from the front of the modern glacier terminus, and ~1 km from its 1956 CE position (Figures 2 and 3). They are

composed of marine intertidal sands with remnants of algae and marine molluscs, bivalves, and the bones of penguins, seals and cetaceans, deposited in an ice-free environment, and capped by a till that represents the last time a local glacier readvanced over the outer part of Potter Cove/Peninsula (Sugden and John, 1973).

Radiocarbon dating of the deepest buried shells and seaweed in these sections provide a maximum age constraint for deglaciation (Strelin et al., 2014). By analogy with observations from modern beaches on Potter Peninsula, seaweed was probably deposited as large trash, subfossil deposits close to the high tide level (Fretwell et al., 2010; Strelin et al., 2014). Sugden and John (1973) first dated shells from a 2.5 m thick stratigraphic section of the “Potter Cove section” (located close to PC in Figure 2) and proposed the oldest age for the onset of the deglaciation and marine transgression from the outer part of Potter Peninsula of $9,670 \pm 230$ ^{14}C years, or $9,570 \pm 650$ cal. a BP (S&J Birm-48a in Table 2, recalibrated in this study). Del Valle et al. (2007) used these ages to constrain the age of a stratigraphic profile named “Pingfo II” (Location 1 in Figure 3B) 60 m to the west in the same moraine, but the ages obtained by Sugden and John (1973) have not been replicated.

3. Methods

3.1 Geomorphological mapping

Detailed geomorphological mapping is an essential first step in assessing the deglacial history of continental margins around Antarctica (Figure 2, 3). Using a glacial landsystems approach (e.g., Davies et al., 2013), we distinguished, landforms and sediment exposures associated with glacier advance and retreat, to understand how the landscape on Potter Peninsula evolved during the Holocene (Table 1). Mapping was undertaken in ARC-GIS v.2.5, with final layouts achieved in Adobe Illustrator v. 26.2.1 or CorelDRAW v. 2020.

3.2 Stratigraphic profile, sampling, and lithofacies analysis

Morphostratigraphic descriptions and sampling for radiocarbon dating were undertaken at an outer peninsula stratigraphic profile site excavated in a similar location to the “Pingfo II” profile (del Valle et al., 2007). We refer to the new profile as “new Pingfo II” (nPII in Figure 2 and Location 1 in Figure 3). We also excavated, described and radiocarbon dated a new river section adjacent to the ‘Potter Cove section’ sampled by Sugden and John (1973). Henceforth, we refer to this as the ‘new Potter Cove section’. Both sections are located at ‘PC’ in Figure 2 and Location 2 in Figure 3. Following recommendations in Björck et al. (1991c), we also radiocarbon dated terrestrial moss samples embedded in a recently exposed ‘Inland outcrop’ ~700 m from the active glacier front and

inside the 1956 CE limit, to constrain glacier readvance(s) on the inner peninsula area (Figure 2 and Location 3 in Figure 3B). Depositional units in the stratigraphic sections were characterised using lithofacies textural (grain size and fabric), composition, sedimentary structures and stratigraphic relationship criteria (Supplementary Materials for additional methods). Summary results were digitised in Figures 5 and 6 using SedLog 3.0 (Zervas et al., 2009) and grain size data are shown in Table S1.

3.3 Lake sediment analysis

After mapping, classifying, and assessing the suitability of the numerous lakes on Potter Peninsula for sediment coring (Supplementary Material; Figure S2), we cored and present here summary results from two foreland lake basins: Matias Lake (ML in Figure 2 and 3B; Lake L5 in Figure S2) and Lake L15 (aka GPS Lake).

Matias Lake (Lake L5, Figure 2 and 3B; 62.2450°S, 58.6655°W) is a small lake sub-basin up to ~6 m deep (del Valle et al., 2004) formed in the moraine deposits of the glacier foreland, adjacent and connected to Rudy Lake (Lake L6) in the mid-foreland area (Figure 2, S2). Located on the eastern, glacier-facing side of Potter Peninsula at the base of, and shaded by Three Brothers Hill, lake-ice often persists into January or February. In contrast, Rudy Lake and Lake L15 are largely free of lake ice by November-December. The southern basin, Rudy Lake, is a larger but shallower basin, ~4 m at its deepest point (del Valle et al., 2004). Both lakes (L5 and L6) are located outside of the 1956 CE glacier limit of the Warszawa Ice Field (Figure 1, 2), ~500 m NW of the 'Inland outcrop'. Following a ground penetrating radar (GPR) survey to locate the depocentre in Matias Lake, 13 sediment cores were extracted from a solid lake-ice platform in November 2011 using a 50 mm wide, 1 m long Livingston corer and a 50 mm wide, 0.5 m long Russian corer.

Lake L15 (62.24056°S S, 58.67757°W) is a small shallow bedrock basin (<1–2 m deep) inland from the new Pingfo II section (L15 in Figure 2, 3). It is a seasonally lake-ice free basin and the furthest permanent water body from the active glacier front on Potter Peninsula (Figure 1, 2, S2). Eight cores were taken from a lake-ice platform over the depocentre using a 50 mm wide, 1 m long Livingston corer and a 50 mm wide, 0.5 m long Russian corer.

Livingston cores were split, and all cores were described in the laboratory. Non-destructive ITRAXTM (Cox Analytical) X-ray fluorescence (XRF) core scanning (XRF-CS) and Bartington Magnetic Susceptibility High Resolution Surface Scanning Sensor (MS2E) measurements were undertaken at Aberystwyth University and on a Geotek® multi-sensor core logger (MSCL) at

Durham University following standard procedures (Gunn and Best, 1998, Davies et al., 2015; Roberts et al., 2022). Contiguous bulk, wet sediment geochemical Energy Dispersive XRF-CS (Energy Dispersive Spectroscopy) data were obtained using a chromium (Cr) X-ray tube (X-radiography image settings: 40 kV, 40 mA, 200 ms; XRF-CS_{Cr} settings: 30 kV, 40 mA, dwell time of 10 seconds, at 100 µm (MAT1) and 2 mm (L15-H2, L15-H16) intervals). Machine and sample calibration were undertaken using a synthetic glass standard and XRF fused glass discs of sediment samples from the nearby Yanou Lake and Ardley Lake records on Fildes Peninsula at the start and end of each analytical phase. Raw count per second (cps) data were analysed using the Cox Analytical Q-spec software.

To account for downcore variations in count rate, density, water and organic content, XRF-CS data are presented as relative changes in percentages of the Total Scatter Normalised ratio sum (%TSN, equivalent to the %cps sum – Saunders et al., 2018; Roberts et al., 2022), and as natural log ratios and centred log ratios (clr). Log ratios have been shown to produce similar downcore patterns to more traditional, and fully quantitative, Wavelength Dispersive Spectroscopy, WDS-XRF, dry subsample analysis (Kylander et al., 2011; Davies et al., 2015; Roberts et al., 2017; Dunlea et al., 2020). Data were filtered to remove the small number of downcore spectra with kcps less than mean minus two-SD, caused mainly by small gaps in the core, and MSE values greater than mean plus four-SD, which represents a poor fit of the measured to theoretical energy spectra. ‘Measurable’ elements were determined by autocorrelation, with significant zones, and their boundary positions, defined by constrained cluster analysis (CONISS) with broken stick analysis applied to square-root-transformed %TSN values of key elements using the R packages Vegan and Rioja (Juggins, 2012; Oksanen, 2014).

Hyperspectral image (HSI) scanning analysis, which measures reflected optical properties between wavelengths from 400 to 1000 nm (Butz et al., 2015), was undertaken at the University of Bern using the Specim Ltd. single core scanner (PFD-CL-65-V10E line scan camera, 400–1000 nm) following the protocol of Butz et al. (2015). The spatial resolution (pixel size) was set at 69 µm x 69 µm and the spectral resolution is 2.8 nm sampled at an interval of 0.78 nm. Raw data were normalised with a BaSO₄ reference and spectral endmembers were calculated using the software ENVI 5.03. Quantitative estimates of pigments were obtained using the Relative Absorption Band Depth (RABD) method, which uses ratios and normalised reflectance data from distinct wavelengths. The spectral index RABD_{660;670} (RABD at 660-670 nm) was calculated from the continuum between 590 and 730 nm (Butz et al., 2015) with I-band wavelengths between 660 and 670 nm using equations $RABD_{660;670} = (6 \cdot R_{590} + 7 \cdot R_{730}) / 13 / R_{\min}(660;670)$ and $RABD_{660;670}$

[I-Band] = $(6 \cdot R_{590} + 7 \cdot R_{730}) / 13 \cdot R_{\min}(660;670) / R_{\text{mean}}$ (Rein and Sirocko, 2002). The spectral index RABD660;670 is proportional to the concentration of sedimentary chlorophyll-a, chlorophyll-b and related coloured diagenetic pheopigments (referred to as total chlorophylls TChl), which are generally interpreted as aquatic primary production indicators (Leavitt and Hodgson, 2001; Butz et al., 2017; Schneider et al., 2018; Makri et al., 2020).

3.4 Chronology and Chronostratigraphy

3.4.1 Radiocarbon dating: Twenty-one Accelerator Mass Spectrometry (AMS) radiocarbon (^{14}C) ages were obtained from seaweed, marine mollusc shells, penguin bones, bones from undetermined species, remnants of terrestrial mosses embedded in marine coastal proximal and terrestrial moraine sediments, and from freshwater subaquatic moss in the uppermost unit (0–6 cm depth) of the Lake L15-H16 (Figure 3E, S6; Table 2). To reduce the risk of contamination with modern material, samples for radiocarbon dating from the stratigraphic sections were taken from freshly cleaned outcrops and stored in zip-lock plastic bags at 4°C. Samples were prepared at the Alfred Wegener Institute Helmholtz Centre for Polar and Marine Research, Durham University, and the British Antarctic Survey. AMS and $^{13}\text{C}/^{12}\text{C}$ isotope ratios measurements undertaken at ETH Zürich, the NERC Radiocarbon Laboratory, East Kilbride, and by Beta Analytical, Miami, were used to calculate Conventional Radiocarbon Ages following established procedures (^{14}C years; Table 2; Supplementary Materials for details).

Calibration of marine sample radiocarbon ages (marine shells, penguin bones, bones from undetermined species, and seaweed) was undertaken in Oxcal v. 4.4 using the Marine20 calibration curve (Gordon and Harkness, 1992; Bronk Ramsey, 2009; Heaton et al., 2020, 2022). We used a newly recalculated local marine reservoir age offset (ΔR) of 666 ± 76 ^{14}C years that represents the weighted mean ΔR of the four closest, and most applicable, radiocarbon-dated marine samples collected prior to 1950 CE from the northern Antarctic Peninsula and Signy Island in the online Marine20 database (<http://calib.org/marine/>) (Table 2; Supplementary Materials for details). Terrestrial and freshwater subaquatic moss samples were calibrated using the Southern Hemisphere SHCal20 (Hogg et al., 2020) calibration curve in Oxcal v. 4.4 (Bronk Ramsey, 2009). Post-bomb (>1950 CE) ages were corrected according to $^{13}\text{C}/^{12}\text{C}$ isotopic ratios from measured pMC with the ‘present day’ pMC value defined as 107.5% (2010 CE) and calibrated using the SHCal13 SH Zone 1-2 Bomb curve in CALIBomb (Reimer and Reimer, 2004; Hua et al., 2013). Median and mean calibrated ages and their 2σ (95.4% confidence level) maximum to minimum error ranges are presented as thousands of years before present (cal. ka BP). Calibrated ages have been rounded to the nearest 10 years in Table 2, and to the nearest hundred years in the text to reflect realistic total

(i.e., all internal and external) uncertainties. Post-bomb ages are presented as Year CE and have been rounded to the nearest year.

Bayesian age-depth models for the new Pingfo II sedimentary sequence and the lake sediment records were constructed using the Bacon R package (Blaauw and Christen, 2011) (Figure 6B, S5). Summed probability density analysis of the new Potter Peninsula radiocarbon data was undertaken using the Rcarbon package v. 1.4.2 (Bevan, 2021) and compared to non-parametric phase modelling (i.e., a probabilistic version of the Oxcal SUM command) using the Bchron v. 4.7.6 R package (Haslett and Parnell, 2008; Parnell, 2021). New radiocarbon data from Potter Peninsula were then incorporated into a new compilation of existing maximum age constraints on glacier readvance from across King George Island and non-parametric phase modelling was undertaken (Figure 6C, D).

3.4.2 Lead-210 (^{210}Pb), Caesium-137 (^{137}Cs) and Americium-241 (^{241}Am) analysis: ^{210}Pb ^{137}Cs and ^{241}Am dating of the uppermost 10 cm of the lake sediment records was undertaken using ~4 g of homogenised dried sediment, added into tubes to a predefined level and sealed gas-tight. After at least 21 days of storage to obtain radioactive equilibrium between ^{226}Ra and ^{222}Rn , activities of radionuclides were measured by well-type gamma spectrometry (Ge-detector, GWC 2522-7500 SL, Canberra Industries Inc., USA) and processed with GENIE 2000 3.0 (Canberra Industries Inc., USA). Data analysis and dating model calculations followed standard procedures defined in Appleby and Oldfield (1978). Lead-210 age estimates were derived using the constant rate of supply (CRS) method (Appleby and Oldfield, 1978) and incorporated into Bayesian age-depth models (Figure 6B, S5) (Supplementary Material for details).

3.4.3 Cosmogenic Helium-3 (^3He) nuclide surface exposure dating: Stable cosmogenic ^3He accumulates in pyroxene and olivine phenocrysts in the upper few cm of basaltic boulders on the Three Brothers Hill moraine system, recording the total time that the rock surface has been exposed to cosmic rays. Using a hammer and chisel to remove the upper few centimetres of exposed surfaces, we collected five samples from boulders perched on moraines between 35-100 m a.s.l. (Figure S1). The sampled boulders were >50 cm in diameter and the most suited for cosmogenic dating analysis as they showed no signs of sediment cover or significant erosion. Their size and shape meant it is very unlikely they had been overturned and post-depositional movement was minimized by sampling boulders on locally flat and stable surfaces, away from steep slopes and cliffs (Figure S1). Differential GPS (dGPS) measurements were undertaken using a Trimble Pathfinder ProXH to determine the precise location and altitude of boulders in relation to the DALL

66019M002 (S62°14'16.335", W58°39'52.364", ellipsoidal height 39.376 m) triangulation station located on the Argentine Carlini base, a few hundred metres away from the sampled erratics. dGPS precision is better than 10 cm in all axes, but ellipsoid correction errors are larger.

Sampling and processing methods are described in detail in the Supplementary Materials (Table 3, Figure S1). Exposure ages were calculated using the CRONUScalc calculator (Version 2.0; Marrero et al., 2016) with the time-dependent Lal (1991)/Stone (2000) scaling model (Lm) for altitude at Antarctic pressure conditions and the primary calibration data set for ^3He in pyroxene, which yields a long term sea-level high latitude (SLHL) scaled production rate of 122 ± 13 at $\text{g}^{-1} \text{a}^{-1}$ (Borchers et al., 2016). We report internal and external uncertainties in Table 3. External age uncertainties include production rate uncertainties and exposure ages determined with other scaling models (e.g., Lifton et al., 2014) vary by up to ~6%. Following Balco et al. (2008), external uncertainties are used for comparison with calibrated AMS radiocarbon ages and error ranges.

All statistical analysis was undertaken, and figures constructed using R v. 4.1.0/RStudio v. 1.4.1717 and packages *Tidyverse*, *ggplot2*, *Vegan*, *Rioja*, *Ggally* v. 2.1.2, *RBacon*, *Rcarbon*, *Bchron*, and *Sigmaplot* v. 14.0, C2 (Juggins, 2007), with final figure layouts achieved in Adobe Illustrator v. 26.2.1 or CorelDRAW v. 2020.

4. Results

We identified four distinct altitudinal and glacially-impacted environments on Potter Peninsula: 0–15 m a.s.l. (Holocene-age and active beaches); 15–50 m a.s.l. (vegetated (perma)frost-affected bedrock plateaus); 50–100 m a.s.l. (fresh-looking, recent glacial deposits); >100 m a.s.l. (Three Brothers Hill) (Figure 2).

To provide a process-oriented, land-systems based assessment, we divided our new geomorphological map of Potter Peninsula shown in Figure 2 into the following four sediment-landform assemblages (LA):

LA-1. Glacier ice and snow, active glacial sediment-landforms.

LA-2. Glacial assemblage of inactive glacial landforms and deposits.

LA-3. Paraglacial and proglacial assemblage, marine/alluvial landforms, and deposits.

LA-4. Periglacial assemblage, hillslope and structural landforms and deposits.

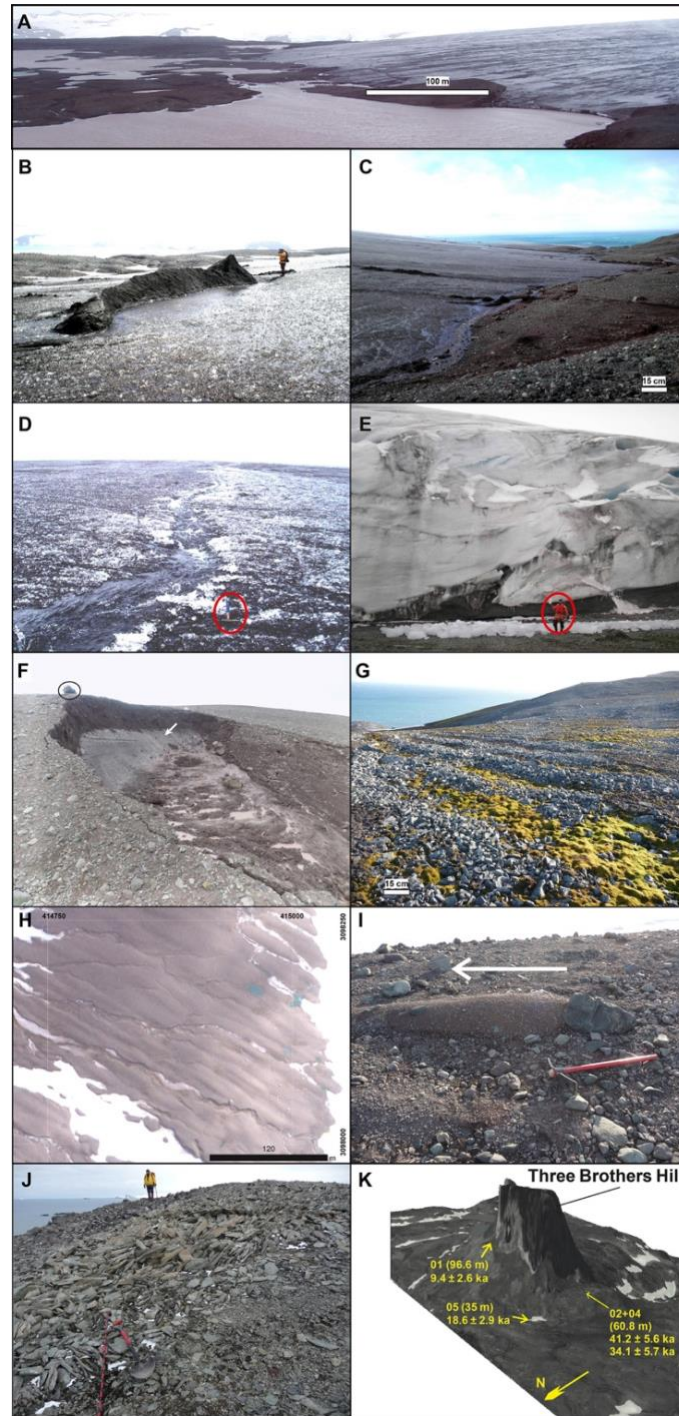


Figure 4. Examples of the active glacial landform assemblages of the Warszawa Icefield on Potter Peninsula: (A) Transverse structures and radial longitudinal foliation. (B) and (C) Transverse foliation related to englacial thrusts and longitudinal foliation associated to melt-out till on the ice surface on the Warszawa Icefield foreland. (D) A supraglacial meltwater channel. (E) Folded layers of subglacial debris in the snout of the icefield, towards the Fourcade Glacier. Components of the glacial and periglacial landform assemblages observed on Potter Peninsula. (F) Slump on glacial deposits showing the collapsing ice-cored moraine (white arrow) at the Warszawa Icefield foreland; bag on top as scale. (G) Vegetated large stone stripes above Stranger Point. (H) Satellite image showing flutings in recently deglaciated glacial deposits, being eroded by glaciofluvial activity. (I) Flutes at a smaller scale, indicating former ice movement direction. (J) Frost shattered bedrock covered to some extent with lichens. (K) Summary of ^3He cosmogenic nuclide surface exposure ages from the Three Brothers Hill area superimposed on a satellite image drape on the KGI-DEM. See Supplementary Material and Table 3 for details.

The main features of these landform assemblages are summarised and interpreted in Table 1 and illustrated in Figures 3, 4, 5. In the following sections, we have organised results obtained from the stratigraphic sections, lake records and chronological analysis according to the landform assemblages described above:

4.1 Landform Assemblage LA-1: Active glacial sediment-landforms

4.1.1 Inland Outcrop on the recently deglaciated inner Warszawa Icefield foreland

The contact between the Warszawa Icefield and its proglacial area is shallow and contains many active glacial sedimentary landforms (Figure 4A; Table 1, Section 1 for further details). In 2013, we discovered a new exposure ~700 m away from the present-day glacier limit (62.2473°S, 58.6466°W). This ‘Inland Outcrop’ is a partly degraded, non-vegetated, 2.3 m-thick massive matrix-supported sandy diamicton. Two radiocarbon ages from basal moss fragments incorporated into the base of a diamicton have mean $\pm 2\sigma$ ages of 1.7 ± 0.1 and 1.8 ± 0.1 cal. ka BP, with a density phase model 95% probability range of 2.2–1.4 cal. ka BP (Figure 5, 6, Table 2, nos. 26, 27). This section represents glacier bulldozing of moss that grew on previously glacier-free areas, and the youngest of the moss radiocarbon ages provides a maximum age constraint on glacier readvance across the mid-upper glacier foreland.

4.2 Landform Assemblage LA-2: Inactive Glacial assemblage

4.2.1 Stratigraphic river sections from northern mid-outer Potter Peninsula

The new Pingfo II (nPII) section (62.2389°S, 58.6729°W; Figure 2A and Location 1 in Figure 3) and “Potter Cove” (PC) river sections (62.23895°S, 58.67113°W; Figure 2 and Location 2 in Figure 3) are part of a small lateral moraine ridge running obliquely to the southern coastline of Potter Cove.

The nPII section is composed of five units of shell-bearing marine sand, and terrestrial sand, sand gravel and gravel (Lithofacies 1–5 in Figure 6A) overlain by a sandy diamicton unit composed of matrix-supported pebble to cobble-sized clasts (Lithofacies 6; Figure 6A) as follows: Lithofacies 1 is a laminated silt/very fine sand with remnants of shells of bivalve *Laternula elliptica* and algae; Lithofacies 2 are composed of beds of massive, matrix to clast supported gravels, ~10–15 cm thick, with subangular to angular clasts up to 5 cm embedded in a sandy matrix; Lithofacies 3 is composed of horizontally-laminated very fine to silty sand, with brownish to orange algae and shelly remains with sporadic subangular clasts up to 7 cm; Lithofacies 4 is composed of horizontally-laminated fine to medium sand, with silty-clay and sporadic sub-angular clasts up to 10 cm, shells of *Laternula elliptica*, penguin bones, and a distinctively compacted brownish (algae)

deposit at 1.60 m covering fine pebbles; Lithofacies 5 is a stratified matrix and clast-supported gravel intercalated with sand and laminated silt, subrounded and subangular clasts up to 10 cm and larger ‘dropstones’ up to 30 cm diameter and has a contorted upper boundary; Lithofacies 6, which is a sandy-clay, matrix-supported, clast rich, massive to weakly laminated diamicton, with striated angular to sub-angular clasts up to 50 cm. The upper surface of the nPII and PC sections is a flat terrace at 6 m a.s.l. littered with larger clasts on the surface facing Potter Cove and forms part of the inactive vegetated glacial assemblage (Figure 3, 6A; Table 1).

Twenty-one samples analysed for AMS radiocarbon dating included remains of different marine organisms, seaweed, with *Laternula elliptica* shells and bones (Figure 6A; Table 2, nos. 1–21). Their mean and median calibrated radiocarbon ages cluster between 7.7–7.2 cal. ka BP, with a density phase model 95% probability range of 8.2–7.0 cal. ka BP. Shells in the lowermost sand unit are small fragments and unlikely to be *in situ* but also imply that the intertidal sand were accumulating between c. 8.2–6.9 cal. ka BP (2 σ calibrated age range). All new ages obtained from the nPII section are distinct (at 95% probability) from older radiocarbon ages of similar marine shells measured by Sugden and John (1973) that have a density phase model 95% probability range of 10.1–9.4 cal. ka BP (Figure 6C; Table 2). Bayesian age-depth modelling shows that deposition of Lithofacies 1 to 4 was broadly in stratigraphic order, with a homogenous sedimentation rate of ~10 mm a⁻¹ (Figure 6B).

Four new AMS radiocarbon ages from marine shells, and a ~2-10 mm thick filamentous seaweed (brown algae) layer collected from between the marine sand unit and the overlying diamicton in the nearby PC river section (Table 2, nos. 22–25; Figure 6C), were dated independently and have mean calibrated ages of c. 7.5±0.2 cal. ka BP, respectively (2 σ range 7.7–7.0 cal. ka BP) (Table 2). Their density phase model 95% probability age range is in close agreement with new ages from the nPII section (Figure 6B, C).

4.2.2 Lake sediment records from the central mid-outer area of Potter Peninsula

Lake L5 (Matias Lake): We extracted 13 short cores from the depocentre in Matias Lake and along a surface transect towards Rudy Lake. Sediment recovery depth ranged from 20 to 60 cm before encountering an impenetrable diamicton layer. Cores MAT1 (L5-H1) (27 cm) and MAT2 (L5-H2) (29 cm) shown in Figure 7 were extracted from the deepest part of Matias Lake (5.8 m; 62° 14’ 42.054”S, 58° 39’ 53.82”W; Figure 2, S2).

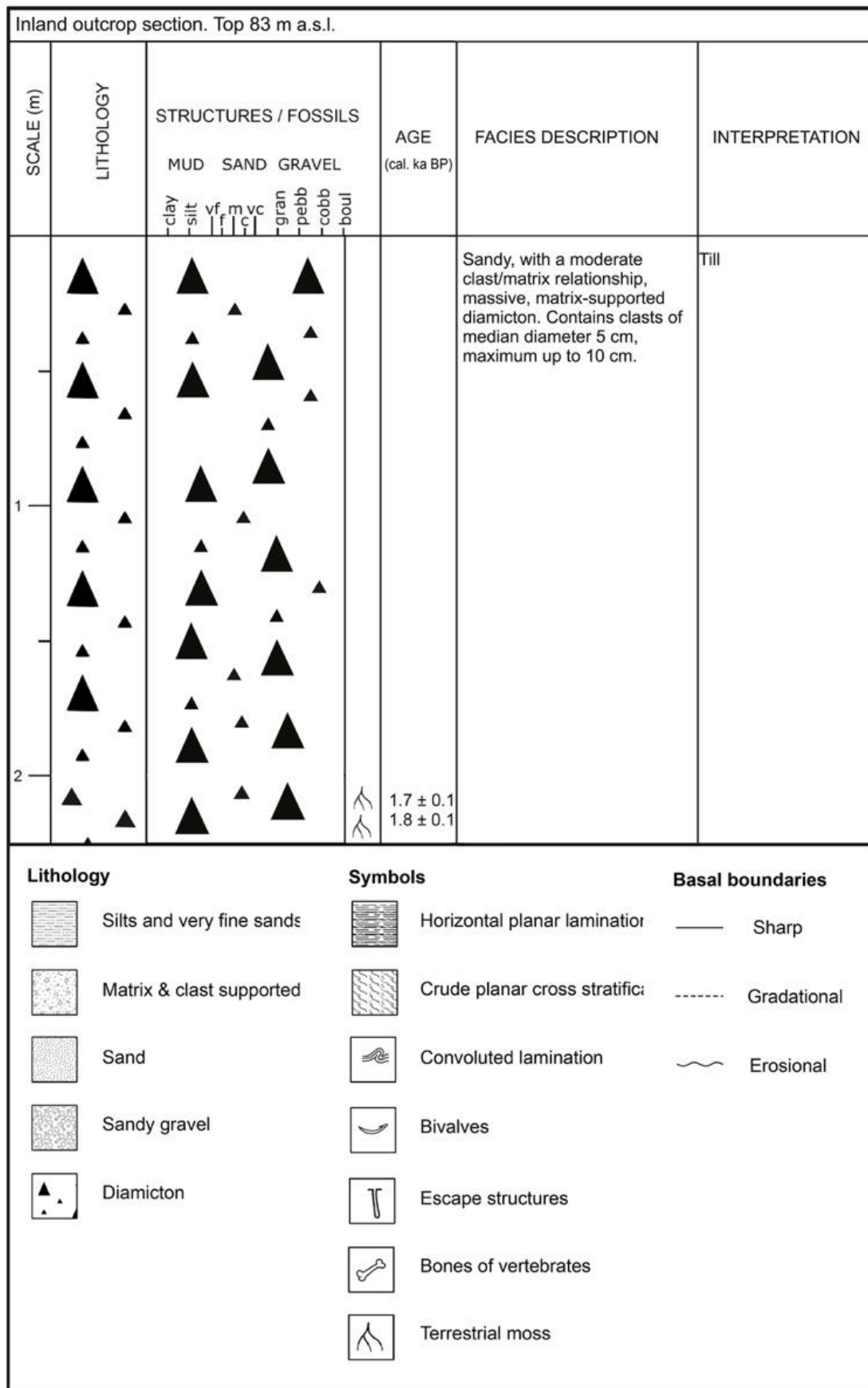


Figure 5. Stratigraphic profile of recently exposed (2013 CE) ‘Inland Outcrop’ glacial deposits, location 3 in Figure 3

Table 1. Summary descriptions of landform assemblages and local geomorphological units identified in this study on Potter Peninsula.

Assemblage	Landforms and moraine systems	Characteristics, distribution, dimensions landforms and geomorphological features	General observations and interpretations
1. Glacier ice and snow, active glacial sediment-landform assemblage	<p>Polished and striated blocks</p> <p>Till ridges (squeeze-crevasse-ridges)</p> <p>Moraine ridges</p> <p>Deltas</p> <p>Lakes</p> <p>Alluvial fans</p> <p>Landslides</p>	<p>Linear and continuous glacial scratches and polish on boulder surfaces, distributed across different volcanic lithologies.</p> <p>Aligned longitudinal diamicton ridges, ~0.3 m high and ~15-50 m long.</p> <p>Linear and curvilinear ridges with gentle lee-flanks and steep stoss-flanks.</p> <p>Fan-shaped features resulting from the discharge of proglacial streams carrying sediments to the sea. 70 m long and 200 m wide. Supraglacial streams aligned with radial structures were visible during warm summer days when snow had melted (Figure 4D). Numerous snowbanks are present in the lee of rock scarps and hill slopes, feeding ephemeral streams flowing on warm summer days (Figure 2).</p> <p>Semi-permanent intra-moraine water bodies. Triangular Lake has an outflow towards the south. Infilled hollows with water source from snowpacks, thawing of permafrost/ice core and seasonal proglacial streams. Many lakes in this zone have developed in the last few decades as the glacier front retreated (Figure 3B).</p> <p>Fan-shaped deposits of decametric dimensions built from sediment discharge in proglacial streams and connected to deltas downstream.</p> <p>Erosive scars and convex accumulation of debris triggered by water saturation of the active layer resting on permafrost. 225 m wide, 70 m long.</p>	<ul style="list-style-type: none"> • Transverse structures recently revealed at the snout of the Warszawa Icefield follow the ice margin, with longitudinal foliation showing radial ice flow patterns (Figure 2, 4A, C). They are associated with glacial debris, suggesting a structural control (e.g., englacial thrusts) and melt-out debris release (Figure 2, 4B, C, E). • Mudflows reworking the unconsolidated glacial sediments exist at the contact between ice-core/permafrost and the active layer . • The recently deglaciated area bordering the Warszawa Icefield is waterlogged and composed of glacial deposits and till without vegetation cover (Figure 2, 3B, 4A). <p>Interpretation: The Warszawa Icefield is an active glacier with structural glaciological controls on landform and sediment development, typical of polythermal glaciers in wet high-latitude maritime environments (Glasser and Bennett, 2004; Hambrey and Glasser, 2012).</p>
2. Glacial assemblage: inactive glacial landforms, deposits, and moraine systems	<p>Lakes</p> <p>Stone sorted circles and polygons</p>	<p>Intra-moraine water bodies. There are also infilled hollows whose water source is from snowpacks; water also comes from mass movements after the degradation of moraines</p> <p>Features on gentle surfaces (3-5°) with thick-grained (i.e., cobbles) sediments towards the periphery. Mainly developed in water saturated areas along streams.</p>	<ul style="list-style-type: none"> • Vegetated glacial deposits, containing predominantly mosses and lichens, occupy the western and southeast sector of the peninsula, which have been ice-free since at least 1956 CE (Figure 2, 3B, 3C, 4G). • Large polished and striated boulders of coarse-grained pyroclastic lithologies and andesitic and basaltic blocks are common in these deposits (Figure 8E).

	Stone stripes	Features with classified sediments of several cm width and several metres length. Developed in slopes up to 10° and between 20 and 50 m a.s.l.	<ul style="list-style-type: none"> ● At the east of Rudy Lake, debris flows have developed on the interface between the active layer and permafrost/ice-core (Figure 4F). In some areas, partially vegetated bedrock plateau surfaces are still relatively fresh and exhibit polished surfaces and striae. ● Recent ice retreat has exposed fluted glacial deposits (flutings) (Figure 2; 4H, I). On the north of the peninsula, flutes are oriented NW-SE, whereas west of Superior Lake they are oriented NNE-SSW, and towards Stranger Point N-S and NW-SE orientations dominate. ● Several till ridges are located along the north coast Potter Peninsula, between two alluvial fans, former deltas, nourished by glacial-lateral meltwater channels (Figure 2). ● Moraine ridges of 80 m length are located southeast of the till ridges. Intensely polished and striated cobbles and boulders of coarse-grained pyroclastics and basaltic and andesitic lithologies are dominant. <p>Interpretation: The Stranger Point moraine system has many features typically associated with ice-cored moraines. The ice proximal slope of the moraine is covered with flutings, indicative of glacier overriding and deformation (Evans and Hiemstra, 2005). These features were most likely formed through proglacial or englacial thrusting and pushing of polythermal ice at the glacier margin. On Potter Peninsula, these features largely manifest as landslides, superficial debris flows, steep slopes and scars showing permafrost as well as stratified glacier ice, thrusts, a pond bordered by asymmetric ridges, and striated boulders and clasts (Figure 8A–E, cf. Davies et al., 2013).</p> <p>As mudflows and landslides are generated at the contact between the permafrost (upper frozen till) and the active layer (Figure 4F, 8A), the permafrost table acts as the sliding surface for the downslope mobilisation of the water-saturated overlying sediments (Oliva and Ruiz-Fernández, 2017). Landslides are triggered by water saturation of the active layer. Melting of ice-cored moraines observed in this and other studies provides sufficient meltwater to trigger debris flows (Figure 4F, 8A) (John and Sugden, 1971; Sugden and John, 1973; Hochschild, 1995; Davies et al., 2013).</p> <p>Flutes formed parallel to the ice-flow are the product of combined erosional and depositional processes of subglacial origin in a water-saturated (warm-based) bed of deformable till (Glasser and Bennett, 2004; Benn and Evans, 2010). Till ridges resemble crevasse-squeeze ridges formed by pressing of saturated basal till during stagnation phases transverse to glacial flow (Benn and Evans, 2010), especially on inter-ice stream ridges (Klages et al., 2013). Till ridges emerging on the glacier front were also most likely formed by ice-thrusting (Figure 4B).</p>
	Inactive protalus lobe	Feature with tongue-like form, conformed of angular boulders. 75 m long, 70 m width. Located at 30 m a.s.l., vegetation implies these landforms are inactive	
	Landslides	Erosive scars and shallow convex accumulation of debris triggered by water saturation of the active layer of permafrost.	
	Flutes	Streamlined, attenuated, lineal hills, associated or not with bedrock obstacles and boulders. Length: width—from 20:1 to 10:1	
	Striated and polished blocks and bedrock	Linear, continuous glacial polish and scratches on some bedrock outcrops and boulder surfaces. Present in mostly basaltic and andesitic lithologies.	
	Stranger Point moraine system, SE Potter Peninsula	<ul style="list-style-type: none"> ● North of Stranger Point a moraine ~200 m from the ice margin, rises to ~105 m a.s.l. and over 1.25 km long and elevated ~40 m above the adjacent bedrock plateau. Its eastern flank descends smoothly towards the present-day beach, while the western side descends to 50 m a.s.l. bordering Triangular Lake. A discontinuous moraine borders the ice on its northern flank directly on the bedrock plateau and is exposed to the south. ● At Stranger Point, a moraine rests up to ~25 m above relict raised beaches ~5–12 m a.s.l. Relatively few morainic crests are preserved due to slumping and debris flows, but the two most prominent morainic ridges enclose a small pond (Figs. 2, 8B). The moraine is composed of unconsolidated, and matrix-supported, basaltic, and andesitic gravels, and boulders. Some boulders show striae and polished surfaces (Figure 8D). Coarse-grained volcanics (pyroclastics) are generally intensely cracked (reworked) by cryoturbation processes, generating stone sorted polygons and stone stripes several metres long (Figure 4G, J). ● The northern morainic ridges are highly degraded by debris flows, which have redeposited unconsolidated moraine sediments downslope. The northern, ice facing slope of the Stranger Point moraine declines towards the glacier at ~20°. More sunshine on the northern slope means snow does not accumulate and the active layer thaws deeper and faster. For this reason, periglacial mass movement processes (mudflows and landslide) are reworking unconsolidated sediments faster on the northern slopes (Figure 2). 	

	Three Brothers Hill moraine system, central Potter Peninsula	<ul style="list-style-type: none"> • The Three Brothers Hill moraine system is located between 100 and 10 m a.s.l. It is partly vegetated by lichens and mosses and has a similar bedrock composition to the Stranger Point moraine (Figure 2). Its topography is most pronounced around the northern flank (up to 40° N–NW slope inclination). In contrast, the south-eastern flank only has a slope of 5° S-SE, with gently sloping moraine ridges spaced more than 100 m apart (Figure 2). • Talus accumulations and rock falls, from frost action weathering on Three Brothers Hill, partially cover preserved morainic ridges on the northern side (Figure 2). Centimetre-scale stone stripes have formed on the surface of the southern sector, which is heavily degraded. 	As morainic ridges surround Three Brothers Hill (Figure 2), these moraines most likely formed by ice pushing against the hill. Degraded and re-deposited morainic till has been reworked by solifluction on inclined surfaces, creating stone stripes at the Stranger Point and Three Brothers Hill moraine systems.
3.1 Paraglacial, Proglacial landforms and Moraine systems	<p>Kettle-lakes</p> <p>Polished and striated blocks</p> <p>Stone sorted circles/polygons</p> <p>Landslides</p> <p>Stone stripes</p> <p>Mudflows/slumps</p> <p>Clast-supported, rounded, and sub-rounded cobbles</p> <p>Resedimented till as debris flows</p>	<p>Water filled hollow created by water of seasonal snowpacks and fusion of ice-core or active table.</p> <p>Linear and continuous glacial scratches and polishing on boulder surfaces.</p> <p>Features on gentle surfaces (3-5°) with coarse-grained (i.e., cobbles) sediments towards the periphery. Located at 90 m a.s.l.</p> <p>Accumulation of debris triggered by water saturation of the active layer resting on permafrost and ice cored moraines. Distributed on the slopes of the moraine, 20/80 m width, 120/180 m length.</p> <p>Features with classified sediments of several cm width and several metres length. Developed on slopes up to 10°, located between 20 and 70 m a.s.l.</p> <p>Rapid mass movements of variable size in fine grained sediments transporting material down-valley onto the Stranger Point moraine system. The sliding surface corresponds to the limit of the active layer in contact with the permafrost table. More abundant on the northern (sun-facing) slope of the Stranger Point moraine.</p> <p>Deposits of clast-supported, rounded, and sub-rounded cobbles facing the northern flank of Three Brothers Hill at ~110 m a.s.l. have diameters up to 30 cm and are protected from falling scree by an overhanging cliff.</p> <p>Degraded moraines surrounding Three Brothers Hill with slopes of 22-27° reworked into several channelized shallow debris flows. On moraines, slopes of 12°, the debris flows are not channelized and are wider with stone stripes developed on top.</p>	<p>Several meltwater channels and related deposits (glaciofluvial fans) resting on the coast are a product of the discharge of moraine sediments from debris flows and sediments transported by snow and ice-melting streams on raised beaches. For example, discharge from Triangular Lake to the sea has formed an alluvial fan and a small delta between its southern outlet and the beach (Figure 2). Inactive glaciofluvial fans cover raised beaches, which terminate against a lagoon at the south coast of the peninsula, next to Elefante Refugee (Figure 2).</p> <p>NW of Warszawa Icefield, meltwater channels from its glacier front cut steep interfluvies up to 4 m high into the fluted glacial deposits and run parallel to the axes of the flutes (Figure 4H) and discharge into the cove forming two glaciofluvial fans and deltas (Figure 2). The Rudy–Matias Lake system developed within these deposits and has an outflow into Potter Cove that cuts through the moraine in which the Potter Cove and Pingfo II sections are located.</p> <p>Interpretation: Clast-supported, rounded, and sub-rounded cobbles facing the northern flank of Three Brothers Hill were originally interpreted in John and Sugden (1971) as pockets of in situ beach material composed of prolate to spheroid clasts. These “residual beaches” were deposited by glaciomarine and/or glaciofluvial processes in a previous (Pleistocene) interglacial or interstadial period but subsequently overridden by ice. Alternatively, they could be interpreted as early Holocene kame terrace deposits.</p>

<p>3.2 Paraglacial landforms:</p> <p>Raised beaches, present-day beaches and proglacial / glaciofluvial landforms</p>	<p>Raised beaches</p> <p>Present-day beach (PDB)</p> <p>Deltas</p> <p>Alluvial fans</p> <p>Inactive alluvial zone/fans</p> <p>Penguin mounds</p> <p>Lake/lagoon</p>	<p>The highest raised beaches are found at Stranger Point at ~12 m a.s.l. Their elevation and their surface grain-size decrease along the south coast in the direction of Potter Cove to the PDB east of Carlini Station. Beach ridges are well developed, and most are poorly vegetated, except for those next to inactive lagoons and those at Stranger Point.</p> <p>The PDB surrounds the Peninsula, with an active berm mean elevation range of 2.4 m a.s.l. at Stranger Point to up to 1 m a.s.l. at Mirounga Point. There is biological activity (penguins, sea lions, elephant seals and stranded algae).</p> <p>Features resulting from the discharge of fluvial sediments in the sea. Up to 50 m long and 70 m wide.</p> <p>Fan-shaped deposits of decametric dimensions. Built up from moraine material, basically through debris flow and sediments transported by snow-melting streams.</p> <p>Deposits of debris of alluvial origin are no longer active. They cover raised beaches.</p> <p>Approximately circular, dome-shaped features up to 20-25 m in diameter and 3 m in height. Principally distributed in raised beaches of Stranger Point and next to the present-day beach along the southeast coast.</p> <p>Permanent water body distributed in flat areas present between a series of raised beaches and the active berm.</p>	<p>Interpretation: The southern and west coast of the peninsula is occupied by a series of raised beaches composed of gravel beach-ridge systems that developed on top of a prograding strand plain (Lindhorst and Schutter, 2014). The northern coast exhibits modern gravel ridges up to 2 m a.s.l., gently sloping seawards. The rest of the coastline is composed of beach ridge-systems at ~11.5, 9.5, 7.5 and ≥ 5.5 m a.s.l. (Lindhorst and Schutter, 2014), with a well-developed spit system at Mirounga Point in the mouth of Potter Cove (Heredia Barión et al., 2019) (Figure 2). At Stranger Point, numerous abandoned and still populated penguin rookeries are situated on top of the penguin-formed pebble-mounds, which are up to 35 m in diameter and up to 2 m higher than underlying raised beach ridges at 12.2 m a.s.l. (Fretwell et al., 2010). The present-day beach is ~ 2 m a.s.l., depending on exposure to prevailing waves (Fretwell et al., 2010; Lindhorst and Schutter, 2014).</p>
<p>4. Periglacial and Hillslope landforms</p>	<p>Polished bedrock (striae)</p> <p>Talus accumulations</p> <p>Solifluction lobes</p>	<p>Linear and continuous scratches and polish of glacial origin on bedrock surfaces.</p> <p>Located from sea-level up to 100 m a.s.l. on Potter Peninsula, these accumulations of coarse sediments at the foot of rock cliffs have been intensely affected by frost shattering. Poorly lichenized sediments suggest they are active or recently dynamic, an exception being around Three Brothers Hill.</p> <p>Generally, solifluction lobes are densely covered by vegetation and located between 80 and 40 m a.s.l. on the bedrock plateaus without vegetation cover. Their width depends on whether they are associated with rock scarps or located on the plateau. They appear as step-like landforms at Three Brothers Hill on south facing talus slopes, often with concentration of clasts in the risers varying from 30 cm up to 1 m in lobes, which appear as tongue-like features ~5 m width in slopes of up to 20°.</p>	<ul style="list-style-type: none"> • Active periglacial processes, such as frost cracking and freeze thaw, occur in some cobbles and boulders of coarse-grained pyroclastic lithologies (Figure 3D), while large boulders of the same lithologies are more resistant to such processes and remain intensely polished and striated. • Basaltic lithologies are, generally, more resistant to periglacial processes. Two tilted bedrock plateaus landward of the south coast of the peninsula between 40–95 m a.s.l. and a near-horizontal plateau at Stranger Point at ~45-50 m a.s.l. are intensely gelifRACTED and frost shattered (Figure 4J). • In some areas, the bedrock is relatively fresh and exhibits polished surfaces and striae. One of the tilted plateaus has a slope of 10° and solifluction processes have evacuated debris by frost shattering and creep to form stone stripes. Protalus lobes, solifluction lobes and talus accumulations at the foot of rock scarps of the bedrock plateaus descend to raised beaches (Figure 2A). Vegetated solifluction lobes in the shade on the south side of the Three Brothers Hill, and a small-sized protalus lobe at 30 m a.s.l. several hundred metres away, southeast of Carlini Station, have been overprinted by sorted polygons and stone stripes deposits.

	Rock falls	Accumulation of large blocks fallen from the margin of bedrock outcrops, adjacent to sea-level up to 14 m a.s.l.	Interpretation: Protalus lobe landforms move down-slope through frost creep and have been associated with deglaciation and transition from a glacial to a periglacial environment on the SSI (Serrano and López-Martínez, 2000). The vegetation cover on the protalus lobes and the absence of a basal talus imply they are inactive (Serrano and López-Martínez, 2000; Kääb, 2007).
	Stone stripes	Features with classified sediments of several cm width and several metres length. Developed on slopes up to 10°.	
	Frost shattered rock/debris/lichens	Highly gelifracted and vegetated bedrock plateaus between 45 and 90 m a.s.l.	
	Protalus lobes	Feature with tongue-like form at 50 m a.s.l., composed of angular boulders, ~120 m long, 50 m wide. The vegetation cover on the protalus lobes and the absence of a basal talus imply they are inactive.	

Table 2. Radiocarbon dating results. Samples 1–21 are from the new Pingfo II section (62.2389°S, 58.6729°W), samples 22–25 from the new “Potter Cove” section (62.23895°S, 58.67113°W), 26–27 from the inland outcrop (62.2473°S, 58.6466°W) and 28–30 from the uppermost freshwater subaquatic moss-dominated Unit 3 in the Lake L15-H16 sediment record (62.2405°S, 58.6772°W). Samples labelled S&J are from Sugden and John (1973); * indicates data not measurable due to small sample size; # indicates an average depth value. Data output produced in Oxcal v. 4.4 using Marine20 and ShCal20 calibration curves (see Methods) (Bronk Ramsey, 2009).

No.	Lab ID	Material dated	Section or Core Depth (m)	Unit	$\delta^{13}\text{C}$ (‰)	AMS ^{14}C age (^{14}C years)	Calibrated age (cal. a BP)												Matrix dated, context, interpretation
							Max.	–	Min.	1 σ %	Max.	–	Min.	2 σ %	Mean	±	2 σ	Median	
1	Beta-441402	Bone (penguin)	1.50	4	–21.6	7860 ± 40	7590	–	7400	68.3	7680	–	7280	95.4	7490	±	200	7490	Fine sed. below till; max. readvance age
2	Beta-441403	Bone (penguin)	1.55	4	–22.2	7890 ± 40	7610	–	7420	68.3	7710	–	7310	95.4	7520	±	200	7520	Fine sed. below till; max. readvance age
3	ETH-67269	Bivalve shell	1.60	4	–1.6	8010 ± 85	7760	–	7500	68.3	7910	–	7400	95.4	7630	±	250	7630	Fine sed. below till; max. readvance age
4	ETH-67267	Bivalve shell	1.70	4	0.0	7805 ± 85	7560	–	7320	68.3	7670	–	7180	95.4	7440	±	240	7440	Fine sed. below till; max. readvance age
5	Beta - 431964	Bone (penguin)	1.85	3-4	–23.1	7780 ± 30	7510	–	7320	68.3	7610	–	7220	95.4	7410	±	190	7420	Fine sed. below till; max. readvance age
6	ETH-67270	Bivalve shell	2.05	3	–1.3	8170 ± 85	7920	–	7660	68.3	8030	–	7520	95.4	7780	±	250	7780	Fine sed. below till; max. readvance age

7	ETH-67272	Bivalve shell	2.10	3	-13.4	8115 ± 80	7850	-	7600	68.3	7970	-	7490	95.4	7730	±	250	7730	Fine seds. below till; max. readvance age
8	ETH-71994	Bivalve shell	2.56	3	2.0	7920 ± 20	7630	-	7450	68.3	7740	-	7350	95.4	7540	±	190	7540	Fine seds. below till; max. readvance age
9	ETH-67268	Bivalve shell	2.70	3	-13.6	7705 ± 80	7470	-	7230	68.3	7580	-	7090	95.4	7340	±	250	7350	Fine seds. below till; max. readvance age
10	ETH-67273	Bivalve shell	2.95	1	-4.4	8005 ± 85	7750	-	7500	68.3	7900	-	7400	95.4	7630	±	250	7630	Fine seds. below till; max. readvance age
11	ETH-67275	Bivalve shell	3.05	1	-12.1	7950 ± 70	7680	-	7450	68.3	7810	-	7340	95.4	7570	±	230	7570	Fine seds. below till; max. readvance age
12	ETH-67274	Seaweed trash layer	3.05	1	-2.3	8020 ± 90	7770	-	7510	68.3	7920	-	7410	95.4	7640	±	260	7640	Fine seds. below till; max. readvance age
13	ETH-67276	Bivalve shell	3.10	1	-10.5	8145 ± 70	7880	-	7640	68.3	7990	-	7530	95.4	7760	±	230	7760	Fine seds. below till; max. readvance age
14	ETH-72000	Bivalve shell	3.11	1	1.3	8015 ± 20	7730	-	7540	68.3	7830	-	7440	95.4	7630	±	200	7630	Fine seds. below till; max. readvance age
15	ETH-67277	Bivalve shell	3.30	1	-1.0	8300 ± 75	8030	-	7770	68.3	8170	-	7660	95.4	7910	±	260	7910	Fine seds. below till; max. readvance age
16	ETH-71996	Bivalve shell	3.41	1	2.9	8005 ± 20	7720	-	7520	68.3	7820	-	7430	95.4	7620	±	200	7620	Fine seds. below till; max. readvance age
17	ETH-71997	Bivalve shell	3.46	1	0.8	7995 ± 20	7700	-	7510	68.3	7810	-	7420	95.4	7610	±	190	7610	Fine seds. below till; max. readvance age
18	Beta - 441404	Bone	3.50	1	-23.8	8100 ± 40	7820	-	7610	68.3	7930	-	7510	95.4	7720	±	210	7720	Fine seds. below till; max. readvance age but possible transport by birds
19	ETH-67278	bivalve shell	3.50	1	-9	8090 ± 75	7830	-	7580	68.3	7950	-	7470	95.4	7710	±	240	7710	Fine seds. below till; max. readvance age
20	ETH-72001	Bivalve shell	4.00	1	2.1	7995 ± 65	7730	-	7500	68.3	7860	-	7400	95.4	7620	±	230	7620	Fine seds. below till; max. readvance age
21	ETH-71995	Bivalve shell	4.47	1	8.0	8195 ± 25	7910	-	7710	68.3	8000	-	7600	95.4	7800	±	200	7800	Fine seds. below till; max. readvance age
22	SUERC-14413	Seaweed trash layer	2.79 [#]	-	-25.3	7831 ± 39	7570	-	7370	68.3	7660	-	7260	95.4	7460	±	200	7460	Fine seds. below till; max. readvance age
23	SUERC-14414	Seaweed trash layer	2.79 [#]	-	-25.6	7883 ± 39	7610	-	7420	68.3	7700	-	7300	95.4	7510	±	200	7510	Fine seds. below till; max. readvance age
24	SUERC-14416	Shell fragment	2.79 [#]	-	1.4	7853 ± 38	7580	-	7390	68.3	7670	-	7280	95.4	7480	±	200	7480	Fine seds. below till; max. readvance age
25	SUERC-14417	Shell fragment	2.79 [#]	-	0.2	7842 ± 37	7570	-	7380	68.3	7660	-	7270	95.4	7470	±	200	7470	Fine seds. below till; max. readvance age
S&J	Birm-23	Seaweed trash layer	2.50	C	-	7863 ± 86	7460	-	7200	68.3	7570	-	7060	95.4	7320	±	260	7330	Fine seds. below till; max. readvance age

S&J	Birm-48a	Shells	2.50	A-B	-	9670 ± 230	9900	-	9240	68.3	10220	-	8950	95.4	9570	± 650	9560	Fine seds. below till; max. readvance age
26	Beta-441400	Terrestrial moss	2.20	1	-20.9	1880 ± 30	1820	-	1770	47.4	1870	-	1860	1.8	1770	± 80	1780	Reworked moraine seds.; max. readvance age
							1750	-	1730	20.8	1840	-	1700	93.7				
27	Beta-441401	Terrestrial moss	2.20	1	-22.1	1850 ± 30	1810	-	1770	23.2	1830	-	1700	84.4	1740	± 110	1740	Reworked moraine seds.; max. readvance age
							1750	-	1700	45.1	1660	-	1610	11.1				
28	Beta-384259	Lake L15 Freshwater moss	0-0.01	2	-22.6	-1017±21	-43.2	-	-44.4	66.9	-45.1	-	-42.9	66.6	-44.0	± -1.1	-44.0	Freshwater subaquatic moss in lake seds.
							-9.1	-	-9.5	26.0	-9.6	-	-9.1	21.2	-9.3	± -0.3	-9.3	
29	Beta-384260	Lake L15 Freshwater smoss	0.035-0.04	2	-20.2	-1213±28	-39.2	-	-41.1	69.5	-38.3	-	-43.1	92.4	-40.7	± 2.4	-40.7	Freshwater subaquatic moss in lake seds.
							-9.7	-	-9.8	4.1	-9.9	-	-9.6	4.0	-9.8	± -0.1	-9.8	
30	Beta-386311	Lake L15 Moss	0.06-0.065	2	*	710 ± 40	660	-	630	33.6	670	-	560	95.4	620	± 70	610	Freshwater subaquatic or littoral moss in lake seds.
							600	-	570	34.7								

Table 3. (A) Sampling information for cosmogenic ^3He nuclide surface exposure dating samples collected around Three Brothers Hill, Potter Peninsula, KGI. All surfaces were dipping less than 10 degrees. Sample 01-Potter, a cobble sitting on top of a morainic crest facing Three Brothers Hill, was taken in its entirety (Figure S1). This sample and 05-Potter have a striated, more weathered upper surface, suggesting that it was glacially transported and preserved in-situ. Samples 02–05-Potter have boulder shapes, sizes and positions that suggest that a recent turnover would be highly unlikely. Topographic shielding of each sample was measured with a clinometer and compass. (B) Results of helium measurements at GFZ Potsdam in pyroxene separates from the Three Brothers Hill samples. ^4He concentrations are in units of $\text{cm}^3 \text{ STP g}^{-1}$, ^3He concentrations in atoms g^{-1} ; all error limits are 2σ . Erosion rate of 0 and rock density of 2.7 g cm^{-3} was assumed. (C) Data for each heating step. The total $^3\text{He}_{\text{cosmo}}$ concentrations have been calculated by summing the ^3He excesses from all heating steps. ¹Altitudes were measured with a Differential GPS Trimble Pathfinder ProXH. Accuracy of 10 cm in all axes; ² The height (h) of the sample means cm above moraine surface; ³Calculated using the online geometric shielding calculator v1.1 (http://hess.ess.washington.edu/math/general/skyline_input.php; Balco et al., 2008); ⁴99% of weight of the separates was pyroxenes. The rest is composed of olivine grains; ⁵Weight of the samples used for stepwise heating extraction; ⁶Sum of all heating steps in (C); ⁷Calculated from $^3\text{He}_{\text{cosmo}} = ^4\text{He}_{\text{heat}} \times (^3\text{He}/^4\text{He}_{\text{heat}} - ^3\text{He}/^4\text{He}_{\text{rad}})$, assuming $^3\text{He}/^4\text{He}_{\text{rad}} = (0.028 \pm 0.028) \times 10^{-6}$. See text for explanation of calculation method; ⁸Obtained using the online calculator

CRONUScalc v2.0 (<http://cronus.cosmogenicnuclides.rocks/2.0/>; Marrero et al., 2016), using the primary calibration data set for ^3He in pyroxene (Borchers et al., 2016) and the time-dependent Lal (1991)/Stone (2000) scaling model (Lm) and SLHL scaled production rate of 122 ± 13 atoms $\text{g}^{-1} \text{yr}^{-1}$ (Borchers et al., 2016).

A

Sample ID	Sample type	Latitude (°S)	Longitude (°W)	x (UTM21)	y (UTM21)	Elevation (m a.s.l.) ¹	Dimensions (l; w; h) (m) ²	Thickness (cm)	Topographic shielding correction ³
01-Potter	Cobble	62.2430	58.6715	413154	3097633	96.6	0.15; 0.25; 0.06	5.6	0.887
02-Potter	Boulder	62.2435	58.6767	412887	3097567	60.8	0.90; 0.50; 0.30	1.7	0.970
04-Potter	Boulder	62.2435	58.6766	412887	3097567	60.9	1.00; 0.45; 0.35	2.2	0.970
05-Potter	Boulder	62.2420	58.6758	412927	3097729	35.0	0.70; 0.70; 0.30	1.3	0.974

B

Sample ID	Weight (g) ⁴	Weight (g) ⁵	$^4\text{He}_{\text{heat}}$ (10^{-8}) ⁶	$^3\text{He}/^4\text{He}_{\text{crush}}$ (10^{-6})	$^3\text{He}/^4\text{He}_{\text{heat}}$ (10^{-6}) ⁶	$^3\text{He}_{\text{cosmo}}$ (10^6) ⁷	Exposure age (ka) ⁸	Internal uncertainty (ka)	External uncertainty (ka)
01-Potter	0.827	0.526	45.8 ± 1.6	0.97 ± 0.12	0.129 ± 0.008	1.25 ± 0.32	9.4	2.4	2.6
02-Potter	0.509	0.282	76.4 ± 1.8	0.47 ± 0.03	0.318 ± 0.015	5.96 ± 0.48	41.2	3.3	5.6
04-Potter	0.511	0.426	78.3 ± 2.7	0.44 ± 0.06	0.261 ± 0.015	4.91 ± 0.62	34.1	4.3	5.7
05-Potter	0.985	0.656	38.6 ± 1.3	1.62 ± 0.26	0.283 ± 0.016	2.64 ± 0.29	18.6	2	2.9

C

Sample ID	T°C	$^4\text{He}_{\text{heat}}$ (10^{-8})	$^3\text{He}/^4\text{He}_{\text{heat}}$ (10^{-6})	$^3\text{He}_{\text{cosmo}}$ (10^6)	$^4\text{He}_{\text{heat}}$ (10^{-8}) Total	$^3\text{He}/^4\text{He}_{\text{heat}}$ (10^{-6}) Total	$^3\text{He}_{\text{cosmo}}$ (10^6) Total
01-Potter	900	39.9 ± 1.6	0.106 ± 0.008	0.84 ± 0.31			
	1750	5.93 ± 0.24	0.288 ± 0.034	0.41 ± 0.07	45.8 ± 1.6	0.129 ± 0.008	1.25 ± 0.32
02-Potter	600	30.9 ± 1.2	0.195 ± 0.016	1.39 ± 0.27			
	900	29.9 ± 1.2	0.385 ± 0.028	2.87 ± 0.34			
	1750	15.62 ± 0.63	0.433 ± 0.038	1.70 ± 0.21	76.4 ± 1.8	0.318 ± 0.015	5.96 ± 0.48
04-Potter	900	67.6 ± 2.7	0.244 ± 0.016	3.93 ± 0.60			
	1750	10.71 ± 0.43	0.367 ± 0.036	0.98 ± 0.14	78.3 ± 2.7	0.261 ± 0.015	4.91 ± 0.62
05-Potter	900	29.9 ± 1.2	0.215 ± 0.016	1.50 ± 0.26			
	1750	8.72 ± 0.35	0.515 ± 0.041	1.14 ± 0.12	38.6 ± 1.3	0.283 ± 0.016	2.64 ± 0.29

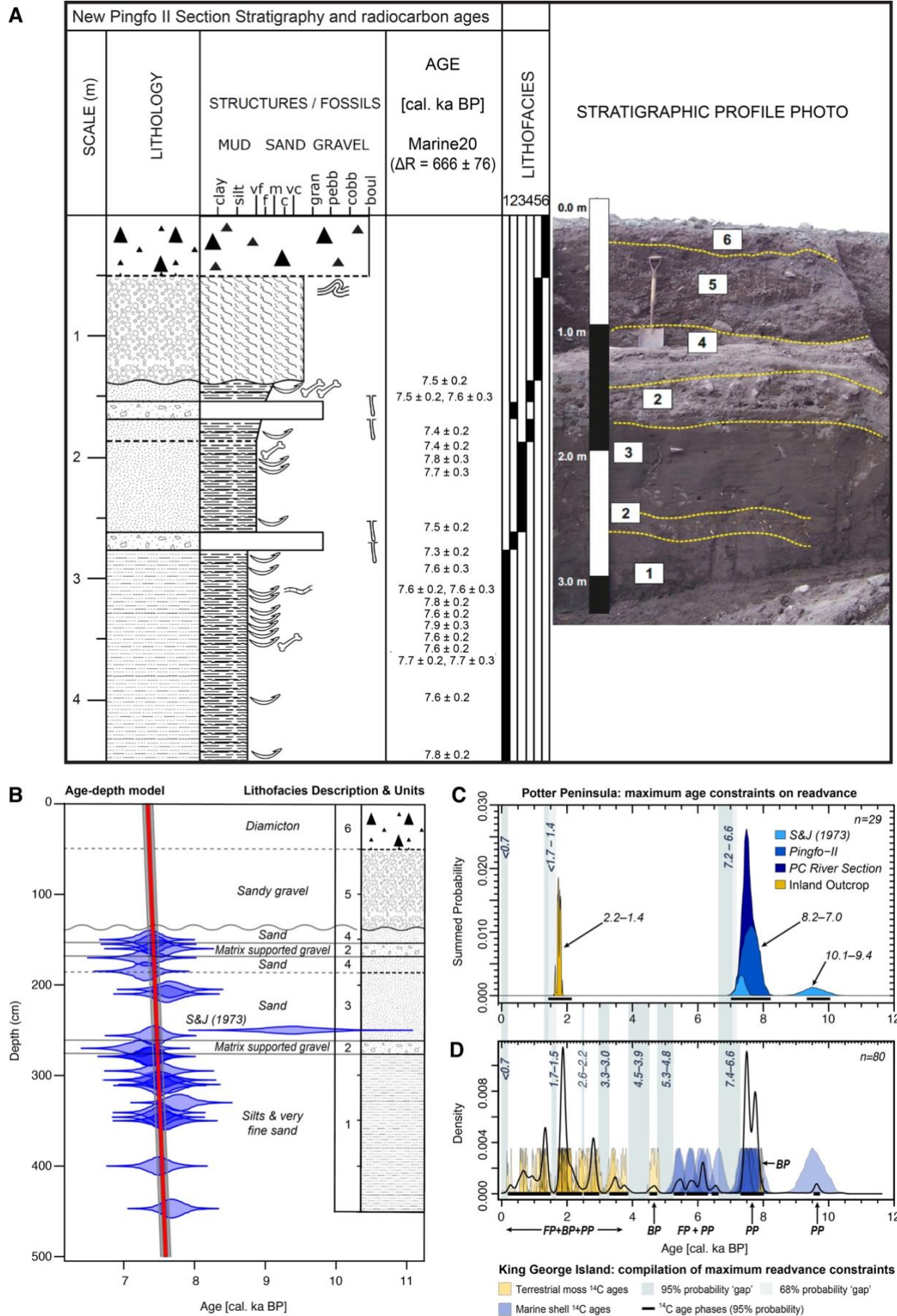


Figure 6. (A) Stratigraphic profile and photograph of new Pingfo II section. Lithofacies units 1 to 6 shown in the photo are described in the main text. Legend is as shown in Figure 5. (B) Bayesian (BACON) age-depth model for the new Pingfo II and River Cut sections showing that new

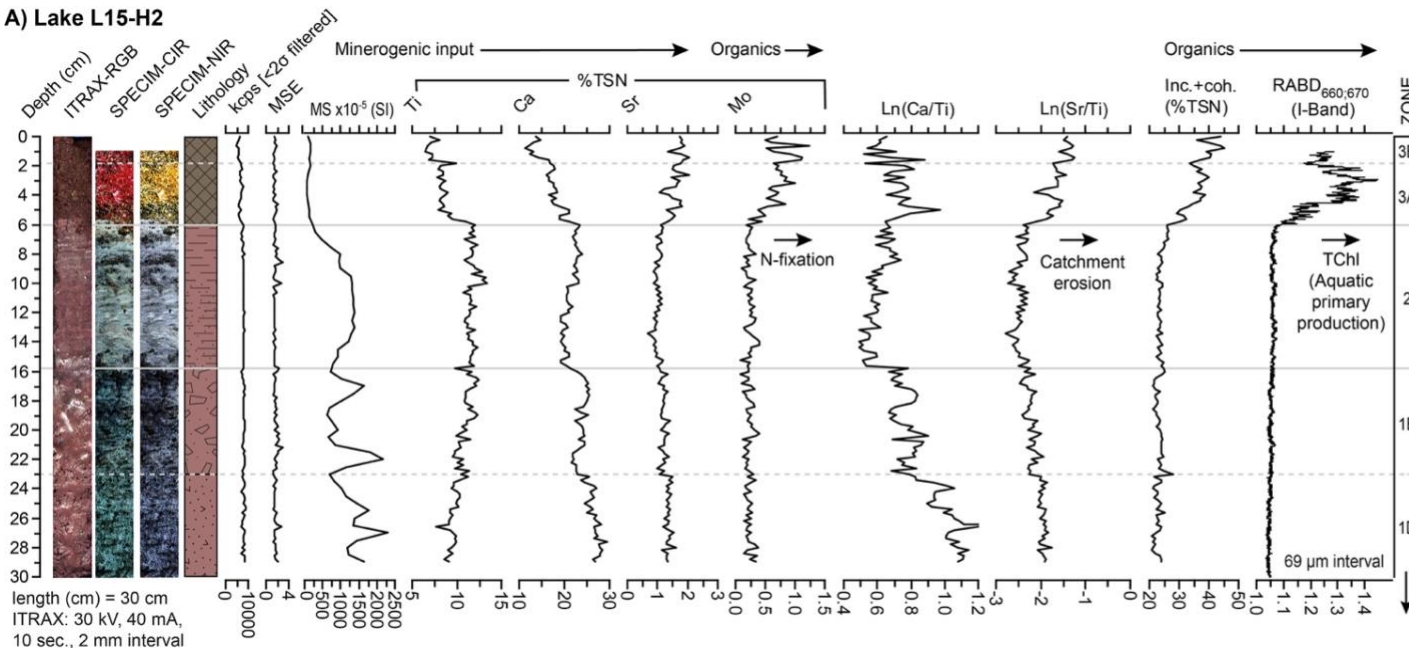
radiocarbon age data are broadly in stratigraphic order, with mean values clustering between 7.8 and 7.5 cal. ka BP (8.0–7.0 cal. ka BP 95% probability density age range). The older age range (10.1–9.4 cal. ka BP 95% probability density age range) based on ages reported by Sugden and John (1973) is a clear outlier. Lithofacies units 1 to 6 are as shown in the photo in A. See Table 2 for radiocarbon data. (C) Summed probability profile of new radiocarbon age data from Potter Peninsula in this study compared with previously published data (S&J = Sugden and John, 1973) in Table 2. (D) Probability density phase model of maximum age constraints on glacier readvance on King George Island between 12–0 cal. ka BP. Dark and light grey shaded zones in (C) and (D) are 95% probability ‘gaps’ when glacier readvances could have occurred. BP=Barton Peninsula; FP=Fildes Peninsula, PP=Potter Peninsula.

Two lithological zones were present across all cores. The basal zone 1 diamicton was predominantly matrix-supported, largely impenetrable, and only retained in some cores. The overlying sediments in zone 2 are composed of fine (mm-scale) grey silty clay and Fe-rich orange clay laminations, probably reflecting periodic (possibly even seasonal) overturning and/or oxidation processes within the lake and glaciolacustrine deposition following the retreat of the Warszawa Icefield landward from Matias Lake and Rudy Lake (Figure 7B).

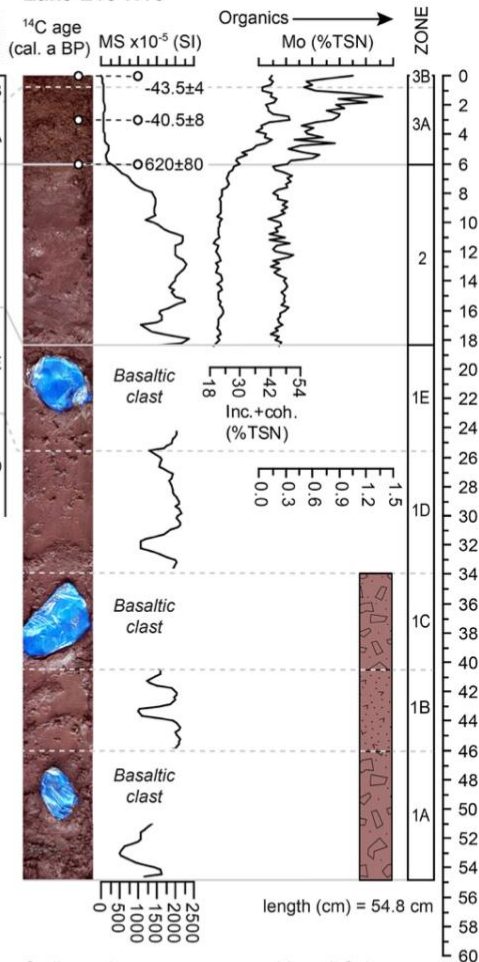
Obtaining basal radiocarbon ages from basal and bulk minerogenic sediments in the Matias Lake cores proved challenging due to a general lack of organic carbon (Figure 7, S5, S6; Table 2). The ^{210}Pb CRS age model shows that the uppermost 10 cm have been deposited since c. 1850 CE, and the well-defined ^{137}Cs peak at 5 cm depth is coherent with the ^{210}Pb age model (Figure 7B; Table S2). A 0.5 cm thick tephra deposit between 8 and 9 cm depth (1908 ± 10 CE) is characterised by elevated Ca and Sr and most likely represents an early C20th eruption from Deception Island, 120 km southwest of Potter Peninsula.

Lake L15 (GPS Lake): We extracted eight cores from a grid of 25 (~1 m spaced) holes drilled through the ~75-100 cm thick lake ice above the deepest accessible point (~2 m) at Lake L15. Core L15-H2 ($62^\circ 14' 26.052''\text{S}$, $58^\circ 40' 39.36''\text{W}$) shown in Figure 7A contained 30 cm of sediment, L15-H4 11 cm, L15-H9 39 cm, L15-H16 55 cm ($62^\circ 14' 26.016''\text{S}$, $58^\circ 40' 39.252''\text{W}$; Figure 7A), L15-H17 45 cm, L15-H19 34 cm, L15-H20 61 cm and L15-H22 49 cm. The same three lithological zones exist in all records. Zone 1 is a fine silt/clay matrix-supported diamicton; zone 2 is a fine silt/clay laminated sediment and zone 3 is a freshwater subaquatic moss. Hyperspectral and XRF-CS profiles show that zones 1 and 2 have very low primary productivity (Figure 7A), with the transition to elevated RABD660;670 values into zone 3 reflecting increased active photosynthesis by subaquatic moss and higher subaquatic primary production. Zone 3A shows a maximum concentration of TChl, which remains high in Zone 3B, but with relatively lower TChl concentrations. This relative decrease might also be related to higher lithogenic sedimentation rates and/or greater porosity.

A) Lake L15-H2



Lake L15-H16



B) Lake L5 -MAT1

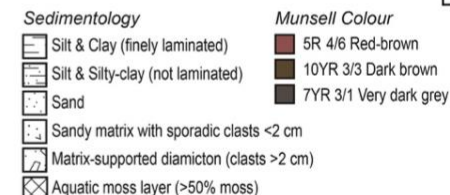
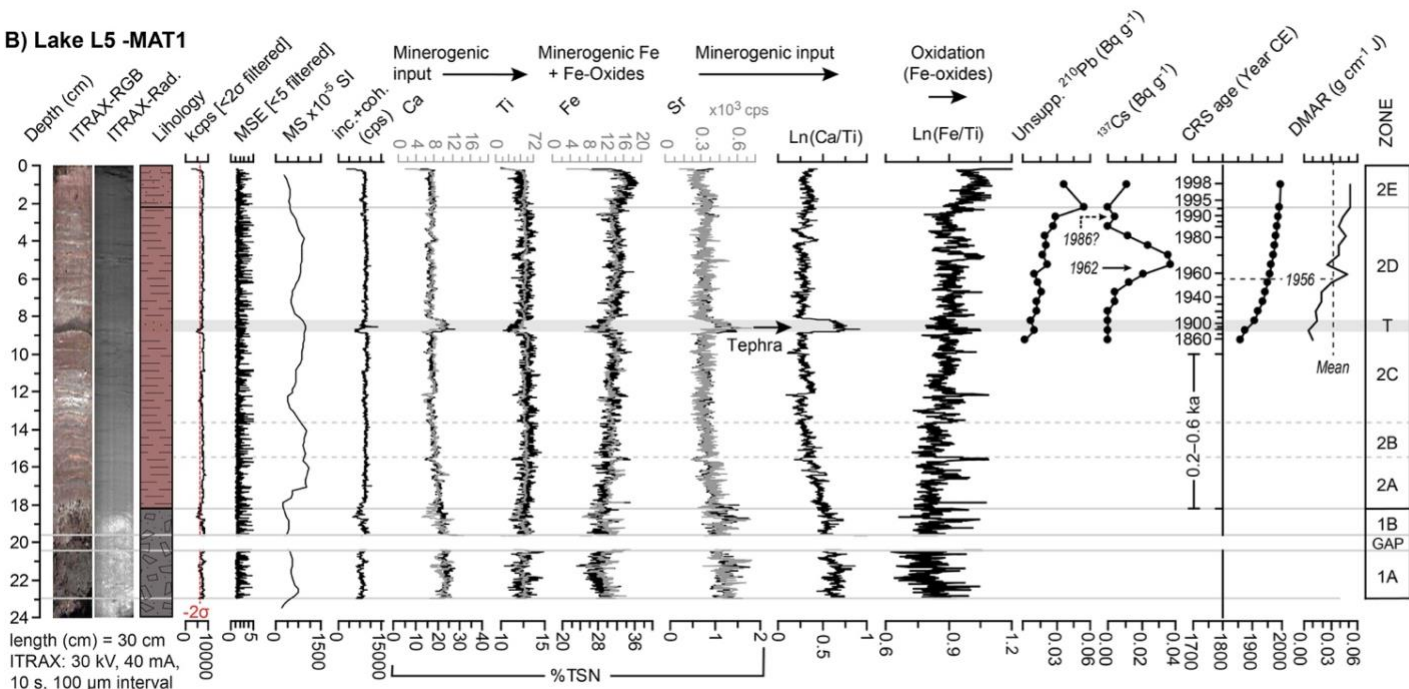


Figure 7. Summary lithological, ITRAXTM XRF-CS, SPECIMTM hyperspectral imagery and data, and chronological data from sediment records from (A) Lake L15 and (B) Matias Lake (ML; L6). A positive correlation between the RABD660;670 (reflecting increased organic productivity) and the XRF-CS molybdenum (Mo) and total scatter profiles in Lake L15 exists because Mo improves the efficiency of nitrogen fixation and the nitrogenase creation process by binding with organic ligands (e.g., tannins) in near surface and sub-aquatic environments (including freshwater moss) and iron oxides and organic matter at depth, preventing it from leaching out of the sediment (Wichard et al., 2009). Conversely, Mo has very low concentrations in mineral-rich sediments as Mo attachment to mineral grains is an insignificant process. Total scatter (inc. + coh.) and scatter ratios (inc./coh.) are also elevated in organic matter as it is less dense and has a higher water content than minerogenic sediments (Davies et al., 2015).

Radiocarbon ages of freshwater moss and macrophytic material from the uppermost lithological Unit 3 in Lake L15 range from post 1950 CE to c. 0.6 cal. ka BP and are statistically distinct from ages obtained from terrestrial moss layers embedded in the ‘Inland Outcrop’ (Figure 2A, 3B, 7, S6; Table 2). The Lake L15 ²¹⁰Pb Constant Rate of Supply (CRS) age model has a low sedimentation rate in the top 10 cm, and the sample at ~4-5 cm is at least 150 years old (Table S3). Although the prerequisite for the CRS model was not fulfilled because the flux of ²¹⁰Pb has changed through time and is not constant, the ²¹⁰Pb data are consistent with the radiocarbon ages that show sediment between 6 and 6.5 cm dates to 620±80 cal. a BP, and 3–3.5 cm and 0–0.5 cm depth were deposited in the ‘post-bomb’ (post-1950 CE) era, most likely between -40 – -44 cal yr BP (1990–1994 CE) (Figure 7; Table 2, S5). The ¹³⁷Cs data are inconsistent with the ²¹⁰Pb CRS age model (Table S3), and it is possible that the steep increase in ¹³⁷Cs in the upper 2 cm relates to a ¹³⁷Cs ‘soil reservoir’, which is leaching ¹³⁷Cs from the catchment into the lake from snow or lake-ice melting.

4.3 Landform Assemblages LA-2, LA-3, and LA-4

4.3.1 *Stranger Point and Three Brothers Hill moraine systems and associated proglacial/periglacial landforms and deposits*

Well preserved morainic crests and glacial erratics are rare in the Three Brothers Hill moraine system mainly because the moraines have been heavily degraded into debris flows and are now covered in talus rock accumulations (Table 1, Figure 8, and Figure S1).

We sampled erratics firmly embedded on the moraine for He-3 cosmogenic nuclide exposure dating to minimise the effect of post-depositional movement. In summary, ages are scattered between 9.4 ± 2.6 ka and 41.2 ± 5.6 ka (Figure 4K, S1, Table 3) and have external uncertainties up to 28% (e.g., sample 01-Potter, Table 3). The two youngest ages from boulders 01-Potter (9.4 ± 2.6 ka) and 05-Potter (18.6 ± 2.9 ka) had striated surfaces indicative of glacial transport and *in-situ* preservation (Table 3). The large age scatter in the ³He cosmogenic nuclide exposure ages and the large individual age errors are due to the low concentration of cosmogenic helium and/or the poorly

known $^3\text{He}/^4\text{He}$ ratio of the non-cosmogenic component. The possibility of previous exposure and complex and poorly understood nuclide inheritance processes cannot be excluded either and, therefore, we consider the ^3He cosmogenic nuclide exposure results to be promising but tentative.

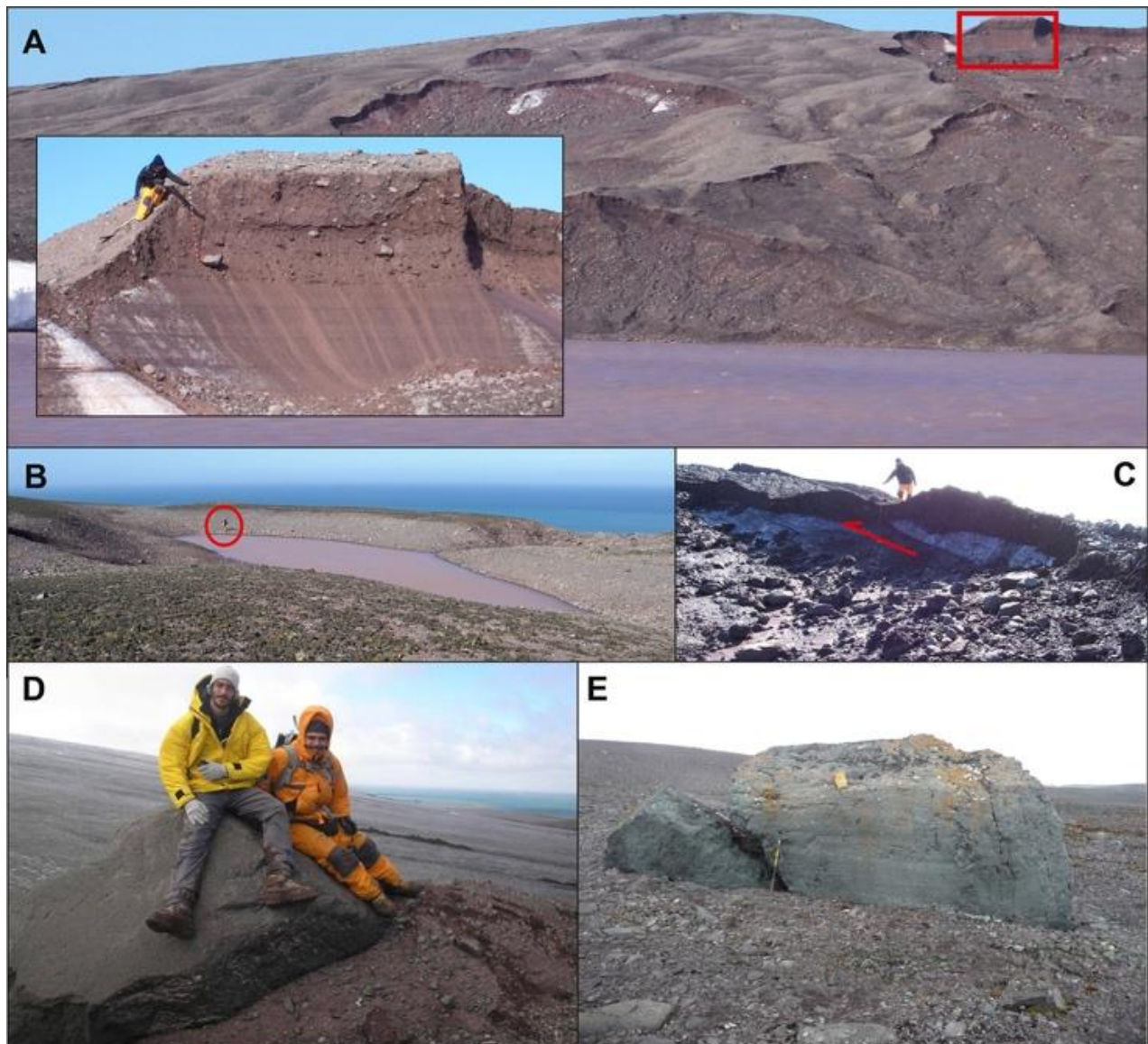


Figure 8. The Stranger Point and Three Brothers Hill moraine landform assemblage and inactive Holocene glacial landforms that have collapsed due to thermoerosion. (A) Debris flows and slumps are reworking the moraine, showing its ice-core. (B) A pond bordered by prominent moraine ridges. (C) A moraine thrust in the direction of the red arrow and mudflows at the foot of the ice-cored moraine. (D) Striated and polished basaltic boulder on the moraine, deposited by thrusting. (E) Polished and striated block in the surroundings of Three Brothers Hill.

5. Discussion

Based on our new geomorphological map and our assessment of the landform assemblages on Potter Peninsula, we propose the following five-stage deglaciation landscape evolution model for Potter Peninsula during the Holocene:

- (1) Early Holocene terrestrial deglaciation began, and a glacier-free environment existed at low altitude in the mouth of Potter Cove, before 8.2 cal. ka BP;
- (2) Deglaciation was interrupted by a readvance that reached outer Potter Cove at, or shortly after, c. 7.0 ka;
- (3) Mid-late Holocene glacier retreat to, or within, present day limits after c. 7.0 ka;
- (4) At least three late Holocene ‘Neoglacial’ readvances to the inner central area of Potter Peninsula between c. 1.7–1.4 ka and small readvances <1 cal. ka BP, similar in extent to the 1956 CE readvance;
- (5) Recent deglaciation (post 1956 CE) and active glacial processes.

We examine the new evidence for these stages in detail in the following sections (Sections 5.1–5.5) in the context of regional environmental change across the SSI and northern AP during the Holocene and suggest possible mechanisms for deglaciation and glacier readvances (Section 5.6).

5.1 Early Holocene terrestrial deglaciation

Ice retreat on land after deglaciation from offshore LGM limits across the South Shetland Islands occurred c. 11–8 cal. ka BP, constrained by ages obtained from glacially polished bedrock surfaces on the Barton and Weaver peninsulas, cosmogenic nuclide exposure ages, and the onset of lake sedimentation on Barton Peninsula, Fildes Peninsulas (KGI), and Byers Peninsula (Livingston Island) (Björck et al., 1996; Seong et al., 2008; Watcham et al., 2011; Toro et al., 2013; Oliva et al., 2016a, b; Nývlt et al., 2020).

Our tentative minimum ^3He cosmogenic nuclide exposure deglaciation age of 9.4 ± 2.6 ka from Three Brothers Hill on Potter Peninsula (Figure 4K) is broadly consistent with the high-altitude deglaciation history of KGI (Seong et al., 2008), and only one of the radiocarbon ages obtained by Sugden and John (1973) (S&J Birm-48a in Table 2: $9,670 \pm 230$ ^{14}C years; $9,570 \pm 650$ cal. a BP), which is clearly an outlier (Figure 6B–D, 9B, 9D). The interpretation of lithofacies assemblages in the nPII and PC stratigraphic sections underpins our revised deglaciation history for Potter Peninsula. Both sections have a lithofacies association typical of polythermal tidewater glaciers (Stewart et al., 1991; Bennett et al., 1999). Lithofacies 1, 3, and 4 were deposited in a distal glaciomarine environment isolated from wave action, with occasional release of ice-rafted debris. Lithofacies 2 is a dense debris flow entering the glaciomarine environment. Escape structures made by *Laternula elliptica* cut across debris flow beds deposited between the glaciomarine sediments suggest the high sedimentation rate caused by the proximity of a glacier likely forced the bivalves to the surface (Figure 6A) (del Valle et al., 2007; Strelin et al., 2014).



Legend for B

KGI terrestrial deglaciation

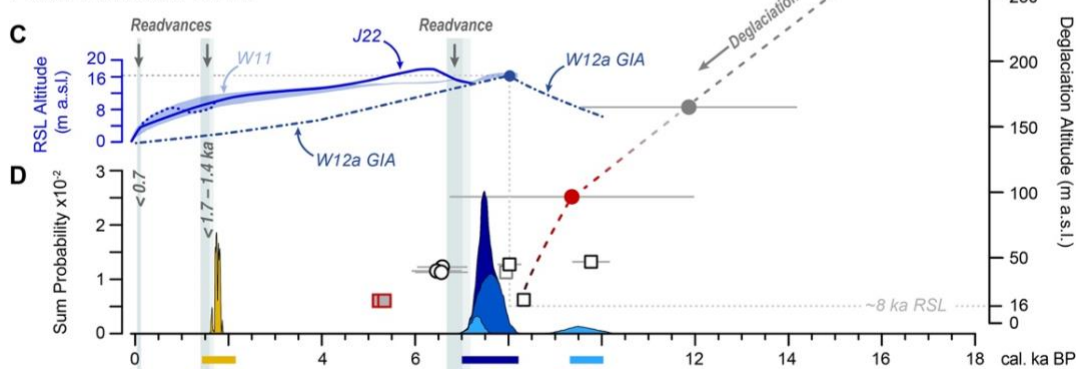
- Cosmo
- Lake
- Beach
- Barton Peninsula
- Fildes Peninsula
- Potter Peninsula

Legend for D

Potter Peninsula ^{14}C 95% probability (n=29)

- S&J
- nPingfo-II*
- PC River Section*
- Inland Outcrop*
- 95% probability 'gap'
- 68% probability 'gap'
- ★ ΔTSI peaks (>10 ka mean)

Potter Peninsula & KGI



Palaeoenvironmental Records

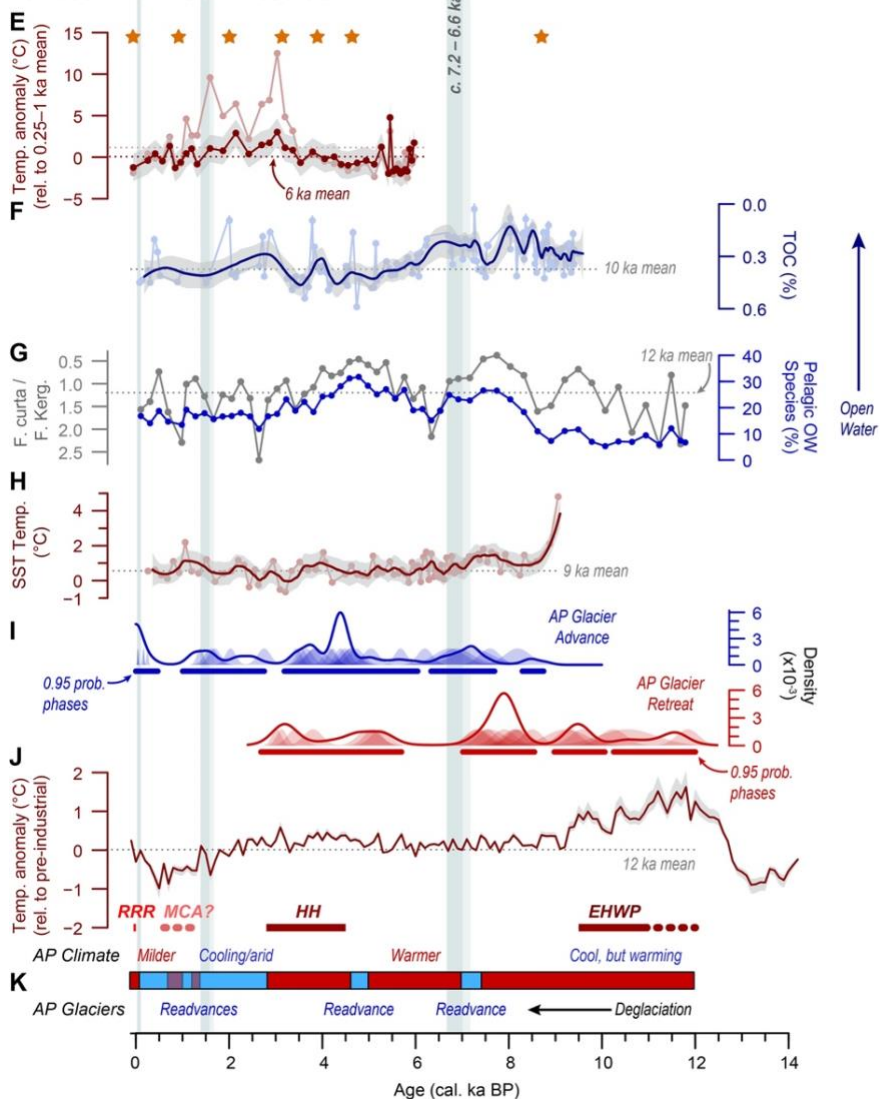


Figure 9. (A) Location map for palaeoenvironmental records in this figure. SHW = Southern Hemisphere Westerly winds. Letters correspond to the records shown below. Dashed white lines are mean modern-day sea ice data (NSIDC 1981–2010 CE; 20% sea-ice coverage from https://nsidc.org/data/seaice_index/) Austral summer minimum (February or Feb.) and winter maximum (September or Sept.) sea-ice limits (solid white lines). The minimum (Feb.) sea-ice extent on the western side of the AP is located off-image further south of the December (Dec.) sea-ice extent. (B) Cosmogenic nuclide exposure ages and key lake basal ages constraining deglaciation on KGI at different altitudes from Barton Peninsula (Seong et al., 2008; Oliva et al., 2019), Potter Peninsula (this study), and Fildes Peninsula (Watcham et al., 2011; Heredia Barión et al., submitted); * = new data (this study). Basal lakes ages constraining early Holocene deglaciation were not obtained from lakes cored on Potter Peninsula as they contained an impenetrable diamicton layer likely due to mid-late Holocene readvances on Potter Peninsula. (C) Summarised relative sea level (RSL) envelope for the SSI (W11; light blue shading; Watcham et al., 2011) compared with the RSL curve in Johnson et al. (2022) (J22; dark solid and dotted blue lines) and the W12a GIA model (Whitehouse et al., 2012a, b); see original references for further details and data. (D) Summed probability profiles and phases (bars) derived from new radiocarbon ages from Potter Peninsula in this study compared with previously published radiocarbon data (S&J = Sugden and John, 1973); readvances shown as vertical grey shaded zones are constrained by data in this plot and Figure 6C, D). (E) Glycerol dialkyl glycerol tetraether (GDGT)–mean summer air temperature (MSAT) anomaly reconstruction (relative to 250–1000 cal. a BP) for the Yanou Lake sediment record, Fildes Peninsula (Foster et al., 2016; Roberts et al., 2017); the dark red plot is a revised MSAT anomaly reconstruction for Yanou Lake based on combining the Pearson et al. (2011) and Foster et al. (2016) datasets, with an RMSE of 1.65 °C shown as grey shading. These new values and its 6 ka mean \pm 1 σ MSAT_{anomaly} of 0.06 \pm 1.50 °C (dark red dotted line) are more realistic than previous values in Roberts et al. (2017) shown in light red; orange stars are Δ TSI peaks greater than the mean Holocene Δ TSI values, see Figure 10A. (F) Maxwell Bay total organic carbon (%TOC) record with lower values interpreted by Milliken et al. (2009) as reduced sea-ice concentration and more open water; the light blue plot is published data; the dark blue line is a 100-yr interval LOESS regression (locally weighted sum of squares with tricube weighting and polynomial regression applied to as published data) with standard errors shaded in grey. (G) Anvers Shelf diatom-based sea-ice reconstruction. Lower species ratio values (grey plot) represent reduced sea-ice concentration and higher pelagic percentage values reflect increased open water (OW) (blue plot) (Roberts et al., 2017). (H) Sea surface temperature (SST) reconstruction from the Palmer Deep (light red plot) (Shevenell, et al., 2011; Etourneau et al., 2013); the dark red line is a 100-yr interval LOESS regression with standard errors shaded in grey. (I) Probability density phase analysis applied to glacier advance (blue) and retreat (red) data in Kaplan et al. (2020) from the northern Antarctic Peninsula. (J) Temperature anomaly data from the James Ross Island (JRI) ice core record, NE Antarctic Peninsula (Mulvaney et al., 2012), with published error limits are shaded in grey. (K) Summary climate syntheses for the Antarctic Peninsula (based on Ingólfsson et al., 2003; Bentley et al., 2009; see Figure S7 for an extended version). EHWP = Early Holocene Warm Period; HH = Holocene Hypsithermal; MCA = Medieval Climate Anomaly; RRR = Recent Rapid Regional warming (after Bentley et al., 2009).

Our oldest sample from a depth of 3.30 m in the nPII and PC sections has a calibrated age of 7,910 \pm 260 cal. a BP and a 2 σ age range of 8170–7660 cal. a BP (Table 2, no. 15), in agreement with more recent studies (Strelin et al., 2014). Similar ages from a further 25 samples from lithofacies 1–4 shows, convincingly, that a glacier-free environment existed at low altitude in the mouth of Potter Cove before 8.2 cal. ka BP (Figure 6A–C, Table 2). This new minimum deglaciation age is younger

than, but consistent with, previous ages from these deposits (cf. Sugden and John, 1973), and our new minimum ^3He cosmogenic nuclide exposure age from Three Brothers Hill of 9.4 ± 2.6 ka.

Our paleoenvironmental interpretations for the nPII and PC sections are in broad agreement with previous studies, but we were unable to replicate older chronologies even though the nPII is 2.5 m deeper than the nearby sections dated by Sugden and John (1973) and del Valle et al. (2007). Our Bayesian age-depth and probability density phase modelling (Figure 6B) reinforces that the older Sugden and John (1973) ages from Lithofacies units 1–5 either represent reworking of an older phase of glacier-free conditions in the outer peninsula or they are statistical outliers, possibly related to improvements in AMS radiocarbon dating since the 1970s.

Our revised early Holocene terrestrial deglaciation history for Potter Peninsula is consistent with evidence for enhanced glacier retreat from Maxwell Bay and sustained deglaciation on the nearby Barton and Fildes peninsulas at low altitude by c. 8.0 cal. ka BP (Figure 9B) (Seong et al., 2008; Milliken et al., 2009; Oliva et al., 2019), and glacier retreat on Livingston Island, c. 8.3–7.5 cal. ka BP (Oliva et al., 2016b). These events followed a period of sustained early Holocene warming across the northern AP region (Figure 9J, K) (Ingólfsson et al., 2003; Strelin et al., 2006; Bentley et al., 2009; Mulvaney et al., 2012).

5.2 A c. 7 ka glacier readvance

Radiocarbon ages from the marine shell bearing horizons of Unit 5 in the nPII section provide a maximum age constraint of c. 7.0 cal. ka BP for a readvance of the former tidewater Fourcade Glacier to the outer mouth of Potter Cove. Glaciodeltaic facies on the surficial morainal bank terrace imply subaqueous discharge close to the calving zone, with contorted deformation structures near the top of Unit 5 most likely resulting from glaciotectonic push and shear (cf. Hambrey and McKelvey, 2000) and indicative of subglacial deformation. Lithofacies 6 represents a period of inter-tidal sand accumulation, and the massive matrix-supported, clast-rich diamicton deposited on top of both sections is interpreted as a subglacial till formed by a readvance at or shortly after c. 7.0 cal. ka BP (Figure 6A, 6D, 9D).

Changes in relative sea level recorded in raised beaches and isolation basins of the SSI provide the most reliable evidence of deglaciation, ice loading and readvance (e.g., Johnson et al., 2022). As isolation basins are less prone to reworking and remobilisation than raised beaches, we attempted to corroborate evidence for a < c. 7 ka readvance in the nPII profile from isolation basins on Potter Peninsula (Figure 2C) below the 8 ka SSI Holocene marine limit at ~16 m a.s.l. (Fretwell et al.,

2010; Watcham et al., 2011) (Figure 9C) by looking for sediment records with marine to terrestrial transitions, but most have gravel (or boulder-strewn) lake beds unsuitable.

RSL curves for the AP and SSI exhibit a regionally coherent shift from rising to falling RSL focused on c. 8.0–7.5 ka, reflecting ice retreat across the northern AP and SSI and isostatic uplift outpacing sea level rise (Watcham et al., 2011; Roberts et al., 2011, Johnson et al., 2022), which possibly prevented further marine-upwelling induced retreat of the Potter Cove glacier. The new c. 7 ka maximum age constraint on glacier readvance for Potter Cove/Peninsula from the nPII section is coeval with a phase of renewed, but comparatively minor, uplift at c. 7.2–7.0 cal. ka BP associated with a standstill or readvance (and/or thickening) of the BIC, first determined from isolation basin studies on Fildes Peninsula (Watcham et al., 2011).

A c. 7 ka readvance is also in broad agreement with surface exposure ages of c. 7.0 cal. ka BP from moraine boulders, which represent a glacier advance on Hurd Peninsula, Livingston Island (Hall, 2007) and land-based glacier readvances on James Ross Island, northeast AP, between 7.3– 7.1 cal. ka BP (Figure 9I) (Strelin et al., 2006; Kaplan et al., 2020). Terrestrial and marine proxies in records from the northern AP indicate extensive glacial melt and open waters without sea-ice in Maxwell Bay, and generally warmer than Holocene average conditions, similar to the present-day shortly after c. 7 ka BP, (Figure 9A, F, G) (Milliken et al., 2009; Watcham et al., 2011; Mulvaney et al., 2012; Peck et al., 2015; Roberts et al., 2017). A precise climate connection between these records and glacier readvance at c. 7 ka on Potter Peninsula therefore remains unclear and is discussed further in Section 5.6.

5.3 Mid–late Holocene deglaciation

Radiocarbon ages from basal lake sediments suggest that glaciers across the SSI and northern AP had receded to within or close to their present-day limits by c. 6 cal. ka BP (Mäusbacher et al., 1989; Watcham et al., 2011; Roberts et al., 2017; Giralt et al., 2020; Gomez et al., 2020). Marine sediment records from Maxwell Bay show decreasing sea surface temperatures and increasing sea-ice cover between c. 5.9 and 2.6 cal. ka BP (Milliken et al., 2009), but we found no evidence for glacier readvance on Potter Peninsula in this period (Figure 6C, 9D).

Hall (2010) and Watcham et al. (2011) both suggested that RSL fall was broadly continuous after 6 cal. ka BP (Figure 9C). Although del Valle et al., (2002) considered abandoned elevated coastal sediments at 17.1–14.4 m a.s.l. at Stranger Point with radiocarbon ages of 5.5–5.4 cal. ka BP to provide a minimum age for beach formation and the onset of the deglaciation on Potter Peninsula, it

seems more likely that these deposits relate to continued uplift following early Holocene deglaciation and retreat after the c. 7 ka readvance. The latter interpretation is consistent with a maximum age of 4.3 cal. ka BP for glacier sediments that overlie the highest continuous raised beach at Stranger Point at ~12 m a.s.l. and RSL curves for the SSI (Fretwell et al., 2010; Lindhorst and Schutter, 2014; Watcham et al., 2011; Johnson et al., 2022).

Jeong (2006) proposed that the diameter of sorted vegetated polygons on KGI is directly related to formation age, with the largest polygon (3.23 m) dated at 5.4 ± 0.1 cal. ka BP. Polygons ~2.5 m in diameter were measured in this study and are tentatively assigned ages >2.6 ka using this method. Deglaciation ages derived using this method have obvious limitations but provide the only available age estimate for the periglacial landform assemblage (LA-4) on Potter Peninsula. Nevertheless, this age is consistent with ages of 4.5 to 2.8 cal. ka BP for a period of sustained mid to late Holocene warming, termed the Mid Holocene Hypsithermal (MHH) in Bentley et al. (2009). Now referred to as the Holocene Hypsithermal, it has been identified in lake sediments from across the northern AP and (sub)Antarctic islands, but glaciers were mostly situated close to, or landward of, their present-day limits (Björck et al., 1991a; Björck, 1991b; Ingólfsson et al., 2003; Sun et al., 2005; Bentley et al., 2009; Strother et al., 2015; Foster et al., 2016; Roberts et al., 2017).

5.4 Neoglaciation in the last 2,000 years

New geomorphological mapping and chronological evidence presented in this paper shows the Warszawa Icefield/Fourcade Glacier advanced beyond present day limits on at least three occasions during the late Holocene: after c. 1.7–1.4 ka, following the return to ‘Neoglacial’ conditions (cf. Ingólfsson et al., 2003; Bentley et al., 2009), after c. 0.7 ka and at 1956 CE.

5.4.1 <1.7–1.4 ka readvances

The ‘Inland Outcrop’, a massive matrix-supported sandy diamicton sequence, ~700 m from the present glacier front was revealed in 2013 following at least ~60 years of retreat of the Warszawa Icefield across inner Potter Peninsula (Figure 2A). This diamicton was probably derived from the foliation of entrained subglacial debris at the glacier front, forming unstable ridges of till with sedimentary characteristics of re-sedimentation from a primary subglacial till by melt out. During melt seasons, its foliation likely collapsed, and any orientation has now been lost (cf. Hambrey et al., 2015).

Warmer and/or more humid conditions that existed prior c. 2.2 cal. ka BP implied by the presence of moss within the ‘Inland Outcrop’ (Figure 6C; 9D) are consistent with similar conditions implied

by the first of two closely-spaced phases of freshwater subaquatic moss deposition in lake records from Fildes Peninsula at c. 2.2–1.9 cal. ka BP and 1.5–1.3 cal. ka BP (Roberts et al., 2017). Remnants of moss layers scattered randomly at its base have median calibrated ages of 1.8 and 1.7 cal. ka BP and a 95% summed probability range of 2.2–1.4 cal. ka BP (Table 2), meaning they were most likely emplaced when the Warszawa Icefield had readvanced further landward by c. 1.7–1.4 cal. ka BP (Figure 6C, 9D).

We link the ‘Inland Outcrop’ to the ice-cored Stranger Point moraine system based on their relative positions to the present glacier margin and the degree of degradation and extent of mass-wasting processes (e.g., landslides and weathering) within the diamicton (Figure 2, 8A-D, F; Table 1). As these sequences are in front of a theoretical former limit of the Warszawa Icefield and form part of the inactive glacial landform assemblage (LA-2) (Figure 2; Table 1), we propose that both sequences were formed by the same glacier advance and subsequent melt-out processes that produced thrusting and deformation of subglacial till at the glacier margin of the Warszawa Icefield (Figure 2, 8C; Table 2).

A readvance sometime after 2.2 cal. ka BP and by c. 1.7–1.4 cal. ka BP in the central foreland of Potter Peninsula is consistent with ages of c. 1.9 cal. ka BP obtained from raised beaches up to 7.3 m a.s.l. overlying volcanic bedrock and till on the south side of Potter Peninsula that imply increased late Holocene ice-loading (Lindhorst and Schutter, 2014). The timing is also consistent with offshore evidence of a glacier readvance dated to c. 2.6–1.6 cal. ka BP from the outermost marine moraine complex, M1, in Potter Cove (Figure 1C; Wöfl et al. 2016) and marine diamictons deposited by ice rafting in Maxwell Bay between c. 1.4 and 1.1 cal. ka BP (Ingólfsson et al., 2003; Yoon et al., 2004). The M1 moraine represents the furthest preserved maximum position of the Fourcade Glacier in the late Holocene (Wöfl et al., 2016).

Although late Holocene ice loading and readvances on Potter Peninsula are too small to be modelled by regional-scale ice sheet and glacio-isostatic adjustment models (e.g., Whitehouse et al., 2012a, b), the most recent RSL curve for the SSI (Johnson et al., 2022) (Figure 9C) hypothesises that the continuous decline from the Holocene marine limit between 8–6 ka was interrupted by increased isostatic uplift between 1.5–0.5 ka BP. Rebound at this time relates to the ‘most significant’ readvance event of the mid-late Holocene (Hall, 2010) and is consistent with published raised beach data and evidence for a post c. 2 ka ‘Neoglacial’ readvance on Potter Peninsula.

Colder ‘Neoglacial’ conditions persisted on the SSI and northern AP from c. 2 ka (2070 ± 50 cal a BP in Čejka et al. (2020)) onwards (Ingólfsson et al., 2003; Bentley et al., 2009; Mulvaney et al., 2012; Hall, 2013; Roberts et al., 2017; Čejka et al., 2020; Palacios et al., 2020). Yet readvance of the BIC on Fildes Peninsula remained restricted close to, or within, present day limits (Hall, 2003; Hall, 2007; Hass et al., 2010; Hall, 2013), while on the Barton Peninsula (KGI), and the Byers Peninsula (Livingston Island), radiocarbon dating of basal lake sediments and exposure ages from bedrock outcrops show that no substantial glacier readvances have occurred in the last 2.4 cal. ka BP (Seong et al., 2008; Oliva et al., 2016a; Oliva et al., 2016b; Oliva et al., 2019). There is also some evidence for short-lived warmer phases in terrestrial records from the northern AP and the sub-Antarctic islands between c. 1.8 and 0.7 cal. ka BP (Bentley et al., 2007, 2009; Hall, 2007; Hall, 2010; Foster et al., 2016; Guglielmin et al., 2016; van der Bilt et al., 2017), and generally warmer sea surface temperatures (SST) on the western AP between c. 2 and 0.8 cal. ka BP (Shevenell et al., 2011; Etourneau et al., 2013).

5.4.2 <0.7 ka readvances

Our new geomorphological mapping revealed vegetated protalus ramparts between 30 and 60 m a.s.l. on Potter Peninsula, approximately 200 m below the current ELA, implying that cooler and drier environmental conditions existed when they were formed. By examining their cross-cutting relationships with raised beaches on Livingston Island, Serrano and López-Martínez (2000) and Kääb (2007) linked their formation to that of low altitude protalus landforms and rock glaciers which advanced between c. 0.8–0.3 ka. Applying a similar principle, the Stranger Point moraine system crosscuts raised beaches at 6 m a.s.l., implying a maximum age of 0.7 cal. ka BP for a readvance at this location (Heredia Barión et al., 2019). This age estimate is consistent with coastal gravel deposits at 6 m a.s.l. that were deposited on top of a till deposit at the west and north coast of Potter Peninsula sometime after 0.65 cal. ka BP (Sugden and John, 1973; Curl, 1980; Clapperton and Sugden, 1988; Lindhorst and Schutter, 2014; Heredia Barión et al., 2019).

Supporting evidence for a readvance after c. 0.7 ka and subsequent retreat also exists in the lake sediment records on Potter Peninsula and includes: 1) The modelled age for the contact between the basal diamicton unit and the uppermost laminated sediments in the Matias Lake record of c. 0.3 cal. ka BP (Figure S5). Del Valle et al. (2004) considered similar laminated sediments in adjacent Rudy Lake to be annual couplets (varves) with sedimentation rates of $1.2\text{--}1.7\text{ mm yr}^{-1}$. This rate is similar to that obtained by ^{210}Pb and ^{137}Cs dating of the uppermost unit of laminated sediments in Matias Lake. The presence of basal gravels with large clasts grading into the uppermost unit of fine ‘varves’ in our new cores from Matias Lake implies the lake was seasonally free of lake-ice, but

with the glacier front nearby. Lead-210 dating of the uppermost laminated sediments of Matias Lake show that glaciers had retreated from the Matias-Rudy Lake area by the mid 1850s; 2) A minimum age of 0.5 ka from Rudy Lake, based on its relationships with adjacent moraines and varve counting of lake sediments above a diamicton deposit (Birkenmajer, 1998; del Valle et al., 2004); 3) The shift to higher productivity and reduced erosion of sediment between zones 2 and 3 in Lake L15, evident in the higher TChl content and lower magnetic susceptibility (MS), Ti and Ca values in zone 3. This is indicative of ice retreat from the outer Potter Peninsula and the establishment of persistent seasonally lake-ice free conditions sometime after 0.6 cal. ka BP (Figure 7A).

Data from marine sediment cores and the submerged moraine complexes M2 and M3 in Potter Cove show that the Fourcade Glacier was located forward of its present position in the inner cove between 0.5 and 0.1 cal. ka BP (Figure 1C) (Hass et al., 2010; Majewski et al., 2012; Wöfl et al., 2016; Munoz and Wellner, 2018). On Fildes Peninsula, ice-cored moraines composed of till, ice-proximal meltwater fan deposits and ice-marginal pond sediments were forming adjacent to present day glacial margins by thrusting processes, incorporating remnants of mosses dated to c. 0.83–0.65 cal. ka BP (Hall, 2007). These mosses represent warmer/milder conditions prior to a <0.7 ka readvance, and their ages are coeval with the timing of the Mediaeval Climate Anomaly (MCA; Figure 9K) c. 1–0.7 cal ka BP, 950–1250 CE (Mann et al., 2009; Kaufman et al., 2020).

More widely, using radiocarbon and optically stimulated luminescence dating of raised beaches, Simms et al. (2012; 2021) showed that the last glacier readvances took place across the SSI and the AP between c. 0.45–0.25 ka BP, and that increased ice loading is consistent with increasing rates of post-MCA RSL decline on KGI in the last 500 years (Bentley et al., 2005; Hall, 2010; Watcham et al., 2011; Johnson et al., 2022) (Figure 9C, K). After this readvance, a short-term and rapid acceleration in rebound occurred between 1700 and 1840 CE (0.2–0.1 cal. ka BP), with a modelled peak uplift rate of 12.5 mm a⁻¹ (Simms et al., 2012). Simms et al. (2012) also showed that RSL curves for the SSI show accelerated fall rates in the last 500 years, indicative of prior increased ice loading, while those from western and north-eastern AP exhibit a gradually decreasing uplift rate, implying continuous deglaciation, despite extensive geomorphological evidence of mid-late Holocene glacier readvance (Bentley et al., 2005; Hall, 2010; Roberts et al., 2011; Watcham et al., 2011; Hodgson et al., 2013; Kaplan et al., 2020).

Evidence for a <0.7 ka readvance on Potter Peninsula is also broadly coeval with: 1) More persistently colder conditions on or around the SSI and the AP (Figure 9E) (Yoon et al., 2004; Liu

et al., 2005; Hall, 2007; Hass et al., 2010; Monien et al., 2011; Angiel and Dąbski, 2012; Majewski et al., 2012; Hu et al., 2013; Roberts et al., 2017; Simms et al., 2021); 2) Generally increased sea-ice in Maxwell Bay and colder conditions in Bransfield Basin between c. 1.4 and 0.1 cal. ka BP (Heroy et al., 2008; Milliken et al., 2009; Mulvaney et al., 2012; Abram et al., 2013); 3) Consistently colder reconstructed sea surface temperatures (SST) in proxy records from the western AP between c. 0.5 and 0.2 cal. ka BP (Figure 9H) (Shevenell et al., 2011; Etourneau et al., 2013); 4) Evidence of a post ‘MCA’ readvance elsewhere on the AP and on some sub-Antarctic Islands (Bentley et al., 2007; Hall, 2007; Bentley et al., 2009; Hall, 2010; Roberts et al., 2010; Davies et al., 2014; Guglielmin et al., 2016; van der Bilt et al., 2017; Verfaillie et al., 2021), at a broadly similar time as the Northern Hemisphere ‘Little Ice Age’ (0.55–0.25 cal. ka BP, 1400–1700 CE) (Mann et al., 2009; Kaufman et al., 2020).

5.5 Recent (post-1956 CE) deglaciation and active geomorphological processes

Aerial photographs show that the Warszawa Icefield was also in an advanced position close to the ‘Inland Outcrop’ in 1956 CE (Figure 3). In 1956 CE, the front of the Fourcade (tidewater) glacier was located 1200 m away from the mouth of Potter Cove (Figure 1, 2), and has since experienced a net retreat of more than 1000 m along the flow line. Aerial and satellite imagery show that the Warszawa Icefield and the Fourcade Glacier then retreated rapidly to its present-day position between 1956 and 2013 CE (Figure 3B), and since 2016 CE, satellite imagery shows that it has terminated on land (Jerosch et al., 2018).

After deglaciation, periglacial/frost action and mass-movement became widespread on Potter Peninsula (Figure 3D, 4J). Rapid mass-movements and rockfalls have transferred the sedimentary products of the periglacial processes down-slope, creating talus accumulation at the foot of bedrock plateaus and around Three Brothers Hill (Figure 2, Table 1). Cryoturbated sorted circles and polygons form on gentle slopes above 50 m a.s.l. and where surficial sediments are saturated with water due to the presence of a permafrost table that inhibits drainage. Repeated freeze-thaw processes, rather than permafrost (Matsuoka, 2001), most likely led to the formation of cryoturbated stone stripes on steeper slopes and gelifluction lobes at the base of the bedrock plateaus.

The inactive Stranger Point moraine system has been actively degraded by mudflows, solifluction and thermokarst processes (Figure 2, 4G, 8A, 8C) (cf. López-Martínez et al., 2012; Oliva and Ruiz-Fernández, 2017). Meanwhile, thermokarst processes are prevalent in active ice-cored moraines close to the glacier margin at Stranger Point and across Potter Peninsula (Figure 4F, 8A, 8C) (John and Sugden, 1971; Sugden and John, 1973; Hochschild, 1995; Lukas, 2011). The large, suspended

sediment load produced by intense glaciofluvial processes at the glacier front and the incision of relict moraines (Figure 4A, H) is forming active glaciofluvial fans and deltas that prograde towards, and into, Potter Cove (Figure 2). Meltwater and suspended sediment change the physical and chemical properties of Potter Cove (Henkel et al., 2013; Henkel et al., 2018; Monien et al., 2017), impacting on the local biological communities, and, ultimately, the biogeochemical cycle of the Southern Ocean (Quartino et al., 2013; Pasotti et al., 2015a, b; Sahade et al., 2015; Monien et al., 2017; Falk et al., 2018; Henkel et al., 2018).

The uppermost 6.5 cm of the Lake L15 and its surrounding environment at the base of Three Brothers Hill is dominated by freshwater subaquatic, littoral and terrestrial mosses and cyanobacterial mats with post-1950 CE ages (Figure S2; see Supplementary Material for further details). Elsewhere on KGI, increased primary productivity and moss colonisation of the lake-water interface is commonplace in seasonally lake-ice free and stable lacustrine environments that are undisturbed by glaciofluvial inputs, and is indicative of warmer and more favourable climatic conditions (Björck et al., 1991c; Roberts et al., 2017).

5.6 Mechanisms of change

After ice retreat from offshore LGM limits (Termination I), early Holocene deglaciation and subsequent glacier fluctuations on Potter Peninsula primarily reflect interactions between changes in climate and relative sea level (Bentley et al., 2009). It seems likely that a c. 7 ka glacier readvance was driven by a combination of changes in glacier stability associated with increased precipitation, regional glacio-isostatic adjustment and/or local relative sea-level variations (Figure 10E-G), rather than major thickening of the glacier front, fjord geometry and fjord depth (Mercer, 1961; Van der Veen, 1995).

Subsequent changes in Holocene glacier mass balance across the SSI were controlled by hemispheric to global scale climate processes and long term (millennial-scale) trends in solar insolation at 62° S (i.e., increasing to c. 5 ka maximum, declining after c. 5 ka) (Bentley et al., 2009). Centennial-millennial scale fluctuations in solar irradiance and interannual to decadal scale changes in the SHW and SAM modulate long-term trends in insolation, driving centennial-millennial changes in temperature, precipitation, wind, sea ice formation, and glacier advance and retreat on the northern AP, the SSI and southern South America (Figure 9, 10) (Bentley et al., 2009; Lamy et al., 2010; Varma et al., 2012; Charman et al., 2018; Moreno et al., 2018; Baggenstos et al., 2019; Reynhout et al., 2019; Kaplan et al., 2020; Verfaillie et al., 2021). The interannual relationship between insolation, temperature ENSO and the SAM is also thought to operate across

decadal to millennial timescales during the Holocene (Perren et al., 2020) (Figure 10B-D), impacting on the AP (e.g., Dickens et al. 2019).

Mechanisms of change

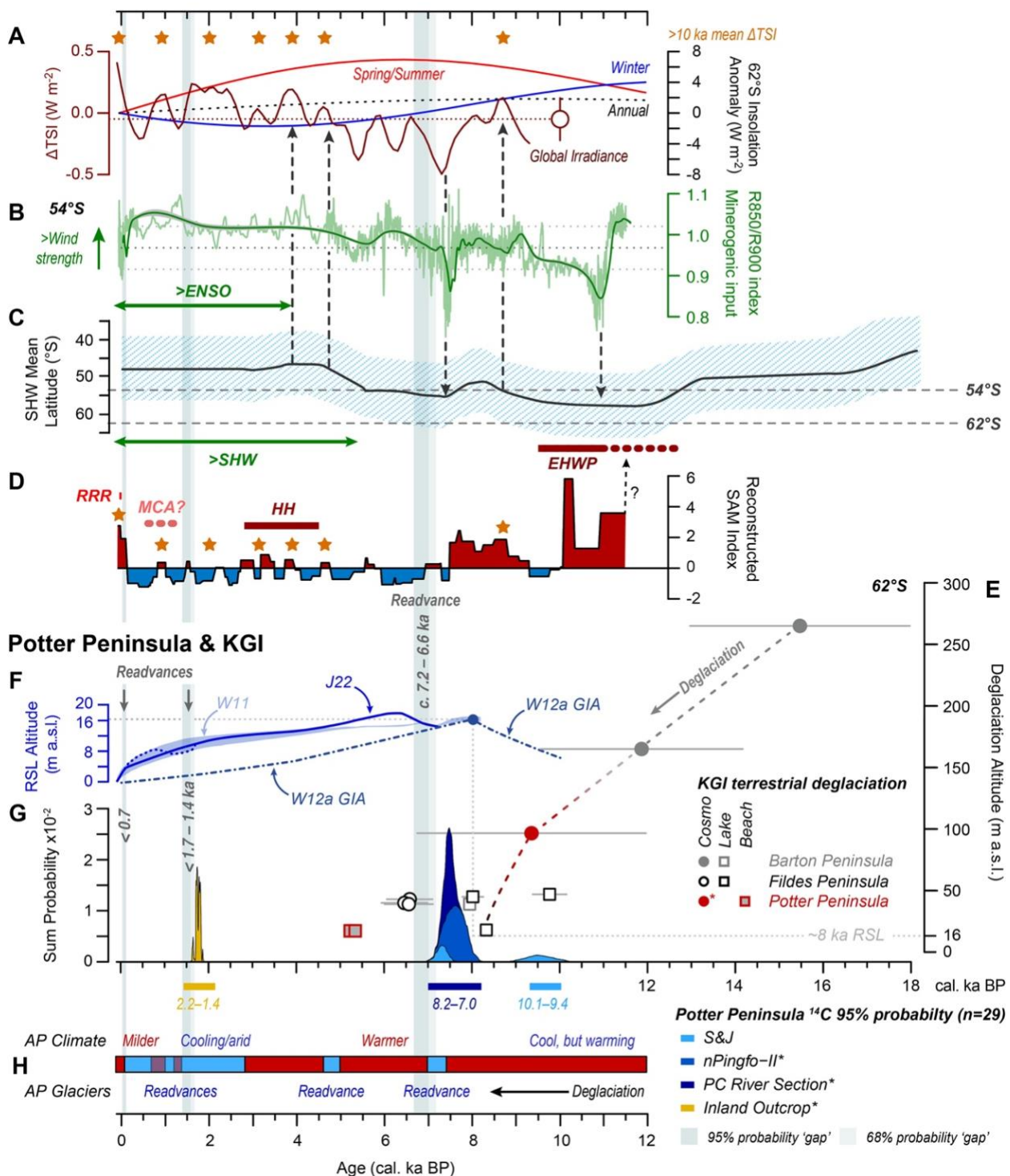


Figure 10 Mechanisms of deglaciation and glacier fluctuations on Potter Peninsula. (A) Total Solar Irradiance, as Δ TSI, which represents the deviation from present day value (Steinhilber et al., 2009), compared with annual (dashed black line), austral spring/summer (SONDJF) (red line), and winter (JJA) (blue line) solar insolation received at 62°S during the Holocene (Laskar et al., 2004). The open red circle is the mean $\pm 1\sigma$ Δ TSI value for the last 10 ka; orange stars mark Δ TSI peaks greater than the 10 ka mean value. (B) Ultra-high resolution (69 μm) hyperspectral (SPECIM)

R850/R900 data, a proxy for mineral input into the Emerald Lake, Macquarie Island at 54°S (Saunders et al., 2018), which reflects changes in the Southern Hemisphere Westerly wind (SHW) strength during the mid–late Holocene; the dark grey horizontal dotted line is the R850/R900 dataset mean; dark green line is 100-year interval LOESS regression analysis of the R850/R900. (C) Hypothetical representation of changes in the mean annual latitudinal position of the core SHW intensity belt (dark grey line) and approximate 1σ latitudinal range of enhanced precipitation (light blue stipple) (Ariztegui et al., 2010; Quade and Kaplan, 2017). In reality, the SHW are more intense and focused during positive (warmer) phases of the SAM, but weaker, latitudinally broader and less focussed during negative (colder) phases of the SAM, shown in D. The light grey horizontal dashes are 54°S (Macquarie Island) and 62°S (South Shetland Islands); vertical dashed lines and arrows highlight the key hypothesised latitudinal shifts of the Holocene and their relationship to the global irradiance profile shown in A; ENSO = El Niño Southern Oscillation. (D) Reconstructed Holocene SAM-index variability between positive (red) to negative (blue) SAM-like states based on Northern Arboreal Pollen data from Southern Chile (Moreno et al., 2018); abbreviations for AP warm phases are defined in Figure 9K. (E) Summarised relative sea level (RSL) envelope for the SSI (W11; light blue shading; Watcham et al., 2011) compared with the RSL curve in Johnson et al. (2022) (J22; dark solid and dotted blue lines) and the W12a GIA model (Whitehouse et al., 2012a, b); see original references for further details and data. (F) Cosmogenic nuclide exposure ages and key lake basal age constraints on the deglaciation of KGI at different altitudes from Barton Peninsula (Seong et al., 2008), Potter Peninsula (this study), and Fildes Peninsula (Heredia Barión et al., submitted) (secondary plot); * = new data (this study). (G) Summed probability profiles and phases (bars) derived from new radiocarbon age data from Potter Peninsula in this study compared with previously published radiocarbon data (S&J = Sugden and John, 1973). (H) Summary climate syntheses for the Antarctic Peninsula (based on Ingólfsson et al., 2003; Bentley et al., 2009; see Figure S7 for an extended version).

Deglaciation of the South Shetland Islands before c. 8.2 ka coincided with a sustained phase of positive SAM-like conditions, increased global irradiance, increasing spring/summer insolation at 62°S, warmth and sustained glacier retreat and more open water on and around the northern AP (Figure 9 F-K, 10A and references therein). A c. 7 ka readvance on Potter Peninsula was initiated during a short-lived period of lower than Holocene average global solar irradiance (Figure 10A) that would have lowered the ELA across the SSI and negative (colder/more humid) SAM-like conditions (Figure 10D), likely leading to increases in year-round precipitation as snowfall (Kaplan et al., 2020). In contrast, after c. 5 ka, a steadily declining trend in insolation at 62°S coupled with more persistently colder/wetter and more negative SAM-like conditions, stronger SHW and an enhanced ENSO (especially during the last 4 ka) likely drove late Holocene readvances after c. 1.7–1.4 cal. ka BP, <0.7 cal. ka BP and by 1956 CE (Figure 10A, D, G) (Charman et al., 2018; Saunders et al., 2018; Yang et al., 2019; Perren et al., 2020).

More recently, the longer-term pattern of interannual variability in the SAM has been altered by the ozone hole over Antarctica, which, combined with increases in greenhouse gases and global temperature, is forcing a more positive trend in the SAM and further enhancing the ENSO (Marshall, 2007). The regionally synchronous retreat of most land-terminating glaciers across the northern AP and SSI since the mid-20th Century provides strong evidence that glacier retreat on

King George Island was initiated by increasing air temperatures (Braun and Gossmann, 2002; Bentley et al., 2009; Kaplan et al., 2020). Recent (post 1956 CE) deglaciation has exposed new onshore areas on Potter Peninsula to intense sediment reworking and redistribution, producing characteristic paraglacial, proglacial, and periglacial landforms on the glacier foreland of Potter Peninsula.

6. Conclusions

Using a glacial landsystems approach, we have produced a new geomorphological map for Potter Peninsula. Based on this and detailed chronostratigraphic analysis of two new stratigraphic profiles and two new lake records on the glacier foreland, we propose the following five stage deglaciation and readvance model for Potter Peninsula:

- (1) Sustained low altitude deglaciation began before 8.2 cal. ka BP.
 - (2) Deglaciation was interrupted by a readvance that reached outer Potter Cove around or shortly after c. 7.0 cal. ka BP.
 - (3) Glacier retreat to or within present day limits likely occurred between 6–2 ka. We found no new terrestrial evidence for readvances across Potter Peninsula in this interval.
 - (4) Evidence of up to three readvances on Potter Peninsula in the last the last 2000 years includes:
 - (i) Radiocarbon ages from mosses embedded in glacial deposits of a recently exposed ‘Inland Outcrop’ close to the modern glacier front imply a readvance had most likely occurred by c. 1.7–1.4 cal. ka BP;
 - (ii) Geomorphic and lake stratigraphic (varve, ^{210}Pb dating) evidence for a <0.7 cal. ka BP readvance, most likely between 0.5 and 0.1 cal. ka BP;
 - (iii) Aerial images showing the Warszawa Icefield was ~700 m in front of its present day limit by 1956 CE.
 - (5) Recent warming and deglaciation has exposed the glacier foreland to periglacial, paraglacial, mass wasting and glaciofluvial processes.
- The timing of Holocene deglaciation and readvances on Potter Peninsula is broadly coeval with sites elsewhere on KGI, the SSI and the northern AP.
 - Early Holocene deglaciation occurred during phases of increased solar irradiance and increasing spring/summer insolation and during a sustained phase of more positive SAM-like conditions that have been associated with increased warmth and glacier retreat across the northern AP.
 - Mid-late Holocene glacier readvances occurred during phases of reduced solar irradiance, and when more negative (colder) SAM-like conditions existed.
 - Field evidence for increased local late Holocene ice loading and readvances on Potter Peninsula is not well-represented in regional-scale ice sheet and glacio-isostatic adjustment models.

Author Contributions

PHB, JS, SR, GK conceived the research questions, obtained funding, wrote the manuscript, and constructed figures and tables; PHB, JS, SR, MB, EP, TMC undertook fieldwork and collected samples; PHB made the geomorphological map and analysed the landscape assemblages; PHB, CS, LW, SN, SR MB, TMC BS undertook cosmogenic and chronological sampling and analysis; SR, SD, MG, SA, BP undertook lake sediment analysis; all authors undertook data analysis and edited the final manuscript.

Conflict of Interest

The authors declare that the research was conducted in the absence of any commercial or financial relationships that could be construed as a potential conflict of interest.

Data availability

Original data presented in this study are included in the article and in the [Supplementary Material](#). Further inquiries should be directed to the first and corresponding authors. Datasets can be obtained from the UK Polar Data Centre ([UK PDC](#)) as follows: [Stratigraphic data](#); Lake sediment data ([Lake L5](#), [Lake L15](#)) (final doi assignments pending); [Advance/retreat database](#). All code, data, packages and package references, are available on [Github](#).

Funding

This study was funded by Centro de Investigaciones en Ciencias de la Tierra (CICTERRA), the Dirección Nacional del Antártico/Instituto Antártico Argentino (DNA/IAA) in the framework of the Project PICTA, 2011 – 0102, IAA “Geomorfología y Geología Glaciar del Archipiélago James Ross e Islas Shetland del Sur, Sector Norte de la Península Antártica”, and by the Alfred Wegener Institute (AWI) research program Polar regions and Coasts in a changing Earth System (PACES II). PHB, GK, JS, SR, EP, TMC were funded by IMCONet (FP7 IRSES, action no. 318718) led by Doris Abele (AWI); EP, SR received additional funding from the Natural Environment Research Council (NERC/BAS-CGS Grant no.81). SR, MB were funded by the NERC/BAS science programmes CACHE-PEP: Natural climate variability – extending the Americas palaeoclimate transect through the Antarctic Peninsula to the pole and GRADES-QWAD: Quaternary West Antarctic Deglaciations.

Acknowledgments

We thank the crews of the Argentine research station “Carlini” and the adjoined German Dallmann (AWI) Laboratory, the Uruguayan research station “Artigas”, the Russian Bellingshausen Station,

the Chinese Great Wall Station, Base Presidente Eduardo Frei Montalva, the Brazilian Navy Almirante Maximiano, the UK Navy (HMS Endurance) and NERC/BAS James Clark Ross for their cordial hospitality and invaluable logistical support during the 2006, 2011, 2014 and 2015 field seasons. Fieldwork assistance by M. Barrionuevo, M. Makeschin, M. Argota, D. Mengedoht, I. Schutter, B. Maltman was greatly appreciated, as were field pictures provided by M. Martini. We also thank S. Wiebe and R. Fröhlking, for their support with textural analyses, C. Schott, A. Toltz, M. Medina and E. Schnabel for sample processing, mineralogy determination and noble gas analysis for ^3He exposure dating, and Mari Whitelaw from the UKRI Polar Data Centre. We thank Tim Heaton (Marine20 radiocarbon calibration) and Bethan Davies (geomorphology/landsystems) for discussions and suggestions, and Daniel Nývlt and Yuribia Munoz for constructive review comments which helped improve the original manuscript.

This paper is dedicated to the memory of Doris Abele and Christian Haas, inspirational scientists, and good friends, who made the IMCONet Exchange Program possible and very enjoyable.

References

- Abram NJ, Wolff EW, and Curran MAJ. (2013) A review of sea ice proxy information from polar ice cores. *Quaternary Science Reviews* 79: 168-183.
- Angiel PJ and Dąbski M. (2012) Lichenometric ages of the Little Ice Age moraines on King George Island and of the last volcanic activity on Penguin Island (West Antarctica). *Geografiska Annaler: Series A, Physical Geography* 94: 395-412.
- Appleby PG and Oldfield F. (1978) The calculation of lead-210 dates assuming a constant rate of supply of unsupported ^{210}Pb to the sediment. *CATENA* 5: 1-8.
- Ariztegui, D., Gilli, A., Anselmetti, F.S., Goñi, R.A., Belardi, J.B., and Espinosa, S. (2010). Lake-level changes in central Patagonia (Argentina): crossing environmental thresholds for Lateglacial and Holocene human occupation. *Journal of Quaternary Science* 25: 1092-1099.
- Baggenstos D, Häberli M, Schmitt J, Shackleton SA, Birner B, Severinghaus JP, et al. (2019) Earth's radiative imbalance from the Last Glacial Maximum to the present. *Proceedings of the National Academy of Sciences* 116: 14881-14886.
- Balco G, Stone JO, Lifton NA, Dunai TJ. (2008). A complete and easily accessible means of calculating surface exposure ages or erosion rates from ^{10}Be and ^{26}Al measurements. *Quaternary Geochronology* 3: 174-195.
- Ballantyne CK. (2002) Paraglacial geomorphology. *Quaternary Science Reviews* 21: 1935-2017.
- Benn DI and Evans DJA. (2010) *Glaciers and Glaciation*: Hodder Education.
- Bennett MR, Hambrey MJ, Huddart D, et al. (1999) The landform and sediment assemblage produced by a tidewater glacier surge in Kongsfjorden, Svalbard. *Quaternary Science Reviews* 18: 1213-1246.
- Bentley MJ, Hodgson DA, Smith JA, et al. (2005) Relative sea level curves for the South Shetland Islands and Marguerite Bay, Antarctic Peninsula. *Quaternary Science Reviews* 24: 1203-1216.
- Bentley MJ, Evans DJA, Fogwill CJ, et al. (2007) Glacial geomorphology and chronology of deglaciation, South Georgia, sub-Antarctic. *Quaternary Science Reviews* 26: 644-677.
- Bentley MJ, Hodgson DA, Smith JA, et al. (2009) Mechanisms of Holocene palaeoenvironmental change in the Antarctic Peninsula region. *The Holocene* 19: 51-69.

- Bentley MJ, Ó Cofaigh C, Anderson JB, Conway H, Davies B, Graham AG, et al. (2014) A community-based geological reconstruction of Antarctic Ice Sheet deglaciation since the Last Glacial Maximum. *Quaternary Science Reviews* 100: 1-9.
- Bevan A. (2021) rcarbon: Calibration and Analysis of Radiocarbon Dates. <https://github.com/ahb108/rcarbon/>.
- Birkenmajer K. (1998) Quaternary geology at Potter Peninsula, King George Island (South Shetland Islands, West Antarctica). *Bulletin of the Polish Academy of Sciences. Earth Sciences* 46: 9-20.
- Björck S, Håkansson H, Zale R, et al. (1991a) A late Holocene lake sediment sequence from Livingston Island, South Shetland Islands, with palaeoclimatic implications. *Antarctic Science* 3: 61-72.
- Björck S, Nils Malmer, Christian Hjort, Per Sandgren, Ólafur Ingólfsson, Bo Wallén, Ronald Ian Lewis Smith, and Bodil Liedberg Jónsson. (1991b) Stratigraphic and Paleoclimatic Studies of a 5500-Year-Old Moss Bank on Elephant Island, Antarctica. *Arctic and Alpine Research* 23: 361-374.
- Björck S, Hjort C, Ingólfsson O, et al. (1991c) Radiocarbon dates from the Antarctic Peninsula region — problems and potential. In: Lowe JJ (ed) *Radiocarbon dating: recent applications and future potential*. Quaternary Proceedings, 55–65.
- Björck S, Hjort C, Ingólfsson Ó, Zale R, Ising J. (1996). Holocene deglaciation chronology from lake sediments. In López-Martínez, J., Thomson, M.R.A. et al., eds. *Geomorphological map of Byers Peninsula, Livingston Island*. BAS GEOMAP Series, Sheet 5-A. Cambridge: British Antarctic Survey, 49–51.
- Blaauw M and Christen JA. (2011) Flexible paleoclimate age-depth models using an autoregressive gamma process. *Bayesian Anal.* 6: 457-474.
- Blindow N, Suckro SK, Rückamp M, et al. (2010) Geometry and thermal regime of the King George Island ice cap, Antarctica, from GPR and GPS. *Annals of Glaciology* 51: 103-109.
- Bockheim J, Vieira G, Ramos M, et al. (2013) Climate warming and permafrost dynamics in the Antarctic Peninsula region. *Global and Planetary Change* 100: 215-223.
- Borchers B, Marrero S, Balco G, et al. (2016) Geological calibration of spallation production rates in the CRONUS-Earth project. *Quaternary Geochronology* 31: 188-198.
- Braun M and Gossmann H. (2002) Glacial Changes in the Areas of Admiralty Bay and Potter Cove, King George Island, Maritime Antarctica. In: Beyer L and Bölter M (eds) *Geoecology of Antarctic Ice-Free Coastal Landscapes*. Berlin, Heidelberg: Springer Berlin Heidelberg, 75-89.
- Bronk Ramsey C. (2009) Bayesian Analysis of Radiocarbon Dates. *Radiocarbon* 51: 337-360.
- Butz C, Grosjean M, Fischer D, et al. (2015) Hyperspectral imaging spectroscopy: a promising method for the biogeochemical analysis of lake sediments. *Journal of Applied Remote Sensing* 9: 096031.
- Butz C, Grosjean M, Goslar T, et al. (2017) Hyperspectral imaging of sedimentary bacterial pigments: a 1700-year history of meromixis from varved Lake Jacznó, northeast Poland. *Journal of Paleolimnology* 58: 57-72.
- Čejka T, Nývlt D, Kopalová K, Bulínová M, Kavan J, Lirio JM, et al. (2020) Timing of the neoglacial onset on the North-Eastern Antarctic Peninsula based on lacustrine archive from Lake Anónima, Vega Island. *Global and Planetary Change* 184: 103050.
- Charman DJ, Roland TP, Amesbury MJ, et al. (2018) Spatially coherent late Holocene Antarctic Peninsula surface air temperature variability. *Geology* 46: 1071-1074.
- Clapperton CM and Sugden DE. (1988) Holocene glacier fluctuations in South America and Antarctica. *Quaternary Science Reviews* 7: 185-198.
- Curl JE. (1980) A glacial history of the South Shetland Islands, Antarctica. *Institute of Polar Studies Report No. 63*. The Ohio State University, 129.
- Davies BJ, Glasser NF, Carrivick JL, et al. (2013) Landscape evolution and ice-sheet behaviour in a semi-arid polar environment: James Ross Island, NE Antarctic Peninsula. *Geological Society, London, Special Publications* 381: 353-395.

- Davies BJ, Golledge NR, Glasser NF, et al. (2014) Modelled glacier response to centennial temperature and precipitation trends on the Antarctic Peninsula. *Nature Climate Change* 4: 993-998.
- Davies SJ, Lamb HF and Roberts SJ. (2015) Micro-XRF Core Scanning in Palaeolimnology: Recent Developments. In: Croudace IW and Rothwell RG (eds) *Micro-XRF Studies of Sediment Cores: Applications of a non-destructive tool for the environmental sciences*. Dordrecht: Springer Netherlands, 189-226.
- de Pablo MA, Blanco JJ, Molina A, Ramos M, Quesada A and Vieira G. (2013) Interannual active layer variability at the Limnopolar Lake CALM site on Byers Peninsula, Livingston Island, Antarctica. *Antarctic Science* 25: 167-180.
- del Valle RA, Montalti D, and Inbar M. (2002) Mid-Holocene macrofossil-bearing raised marine beaches at Potter Peninsula, King George Island, South Shetland Islands. *Antarctic Science* 14: 263-269.
- del Valle RA, Tatur A, Lusky J, and Gómez Izquierdo D. (2004) Cambios morfológicos recientes en lagos de la península Potter, isla 25 de Mayo, islas Shetland del Sur, Antártida. *Revista de la Asociación Geológica Argentina* 59: 443-450.
- del Valle RA, Montalti D, Inbar M, and Boaretto E. (2007) Holoceno marino en la península Potter, Isla 25 de Mayo, Antártida. *Revista de la Asociación Geológica Argentina* 62: 35-43.
- Deregibus D, Scharf FK, Pasotti F, Ruiz Barlett E, Servetto N, and Abele D. (2015) IMCONet Research Areas Map of Potter Cove, King-George Island (I. 25 de Mayo), with links to maps. 10.1594/PANGAEA.853859
- Dickens WA, Kuhn G, Leng MJ, et al. (2019) Enhanced glacial discharge from the eastern Antarctic Peninsula since the 1700s associated with a positive Southern Annular Mode. *Scientific Reports* 9: 14606.
- Dunlea AG, Murray RW, Tada R, et al. (2020) Intercomparison of XRF Core Scanning Results From Seven Labs and Approaches to Practical Calibration. *Geochemistry, Geophysics, Geosystems* 21: e2020GC009248.
- Etourneau J, Collins LG, Willmott V, et al. (2013) Holocene climate variations in the western Antarctic Peninsula: evidence for sea ice extent predominantly controlled by changes in insolation and ENSO variability. *Clim. Past* 9: 1431-1446.
- Evans DJA and Hiemstra JF. (2005) Till deposition by glacier submarginal, incremental thickening. *Earth Surface Processes and Landforms* 30: 1633-1662.
- Falk U, López DA and Silva-Busso A. (2018) Multi-year analysis of distributed glacier mass balance modelling and equilibrium line altitude on King George Island, Antarctic Peninsula. *The Cryosphere* 12: 1211-1232.
- Falk U and Silva-Busso A. (2020) Discharge of groundwater flow to the Potter Cove on King George Island, Antarctic Peninsula. *Hydrol. Earth Syst. Sci. Discuss.* 2020: 1-24.
- Foster LC, Pearson EJ, Juggins S, et al. (2016) Development of a regional glycerol dialkyl glycerol tetraether (GDGT)-temperature calibration for Antarctic and sub-Antarctic lakes. *Earth and Planetary Science Letters* 433: 370-379.
- Fourcade NH. (1960) *Estudio geológico-petrográfico de Caleta Potter, Isla 25 de Mayo, Islas Shetland del Sur*, Vol. 8. Buenos Aires. pp. 119
- Fretwell PT, Hodgson DA, Watcham EP, et al. (2010) Holocene isostatic uplift of the South Shetland Islands, Antarctic Peninsula, modelled from raised beaches. *Quaternary Science Reviews* 29: 1880-1893.
- Gibbard, P.L., and Head, M.J. (2020). Chapter 30 - The Quaternary Period, in *Geologic Time Scale* 2020, eds. F.M. Gradstein, J.G. Ogg, M.D. Schmitz & G.M. Ogg. Elsevier), 1217-1255.
- Giralt S, Hernández A, Pla-Rabes S, Antoniades D, Toro M, Granados I., et al. (2020) Chapter 3 - Holocene environmental changes inferred from Antarctic lake sediments. In: Oliva M and Ruiz-Fernández J (eds) *Past Antarctica*. Academic Press, 51-66.
- Glasser NF and Bennett MR. (2004) Glacial erosional landforms: origins and significance for palaeoglaciology. *Progress in Physical Geography: Earth and Environment* 28: 43-75.

- Gomez N, Weber ME, Clark PU, et al. (2020) Antarctic ice dynamics amplified by Northern Hemisphere sea-level forcing. *Nature* 587: 600-604.
- González-Ferrán O and Katsui Y. (1970) *Estudio integral del volcanismo cenozoico superior de las Islas Shetland del Sur, Antártida*. Vol. 1, 123-174. Santiago de Chile.
- Goodwin BP, Mosley-Thompson E, Wilson AB, et al. (2016) Accumulation Variability in the Antarctic Peninsula: The Role of Large-Scale Atmospheric Oscillations and Their Interactions. *Journal of Climate* 29: 2579-2596.
- Gordon JE and Harkness DD. (1992) Magnitude and geographic variation of the radiocarbon content in Antarctic marine life: Implications for reservoir corrections in radiocarbon dating. *Quaternary Science Reviews* 11: 697-708.
- Guglielmin M, Convey P, Malfasi F, et al. (2016) Glacial fluctuations since the ‘Medieval Warm Period’ at Rothera Point (western Antarctic Peninsula). *The Holocene* 26: 154-158.
- Gunn, D.E., and Best, A.I. (1998). A new automated nondestructive system for high resolution multi-sensor core logging of open sediment cores. *Geo-Marine Letters* 18, 70-77.
- Hall BL. (2003) An Overview of Late Pleistocene Glaciation in the South Shetland Islands. *Antarctic Peninsula Climate Variability: Historical and Paleoenvironmental Perspectives*: 103-113.
- Hall BL. (2007) Late-Holocene advance of the Collins Ice Cap, King George Island, South Shetland Islands. *The Holocene* 17: 1253-1258.
- Hall BL. (2010) Holocene relative sea-level changes and ice fluctuations in the South Shetland Islands. *Global and Planetary Change* 74: 15-26.
- Hall BL. (2013) An Overview of Late Pleistocene Glaciation in the South Shetland Islands. *Antarctic Peninsula Climate Variability: Historical and Paleoenvironmental Perspectives*. American Geophysical Union, 103-113.
- Hambrey MJ and Glasser NF. (2012) Discriminating glacier thermal and dynamic regimes in the sedimentary record. *Sedimentary Geology* 251-252: 1-33.
- Hambrey MJ and McKelvey B. (2000) Major Neogene fluctuations of the East Antarctic ice sheet: Stratigraphic evidence from the Lambert Glacier region. *Geology* 28: 887-890.
- Hambrey MJ, Davies BJ, Glasser NF, et al. (2015) Structure and sedimentology of George VI Ice Shelf, Antarctic Peninsula: implications for ice-sheet dynamics and landform development. *Journal of the Geological Society* 172: 599-613.
- Haslett J and Parnell A. (2008) A simple monotone process with application to radiocarbon-dated depth chronologies. *Journal of the Royal Statistical Society: Series C (Applied Statistics)* 57: 399-418.
- Hass HC, Kuhn G, Monien P, et al. (2010) Climate fluctuations during the past two millennia as recorded in sediments from Maxwell Bay, South Shetland Islands, West Antarctica. *Geological Society, London, Special Publications* 344: 243-260.
- Heaton TJ, Köhler P, Butzin M, Bard E, Reimer RW, Austin WEN, et al. (2020) Marine20—The Marine Radiocarbon Age Calibration Curve (0–55,000 cal BP). *Radiocarbon* 62: 779-820.
- Heaton, T.J., Bard, E., Bronk Ramsey, C., Butzin, M., Hatté, C., Hughen, K.A., Köhler, P., and Reimer, P.J. (2022). A response to community questions on the Marine20 radiocarbon age calibration curve: marine reservoir ages and the calibration of ¹⁴C samples from the oceans. *Radiocarbon*: 1-27. doi:10.1017/RDC.2022.66
- Henkel S, Kasten S, Sala H, Busso AS, and Staubwasser M. (2013) Effect of increased glacier melt on diagenetic Fe cycling in marine sediments at King George Island (Antarctica). *Mineralogical Magazine - H: Goldschmidt Abstracts* 2013 77: 1287-1287.
- Henkel S, Kasten S, Hartmann JF, Silva-Busso A, and Staubwasser M. (2018) Iron cycling and stable Fe isotope fractionation in Antarctic shelf sediments, King George Island. *Geochimica et Cosmochimica Acta* 237: 320-338.
- Heredia Barión, P., S. Lindhorst, I. Schutter, U. Falk and G. Kuhn (2019). Reaction of a polar gravel-spit system to atmospheric warming and glacier retreat as reflected by morphology and internal sediment geometries (South Shetland Islands, Antarctica). *Earth Surface Processes and Landforms* 44(5): 1148-1162.

- Heredia Barión P, Roberts SJ, Spiegel C, Binnie SA, Wacker L, Davies J, et al. (in review) Mid-late Holocene deglaciation and glacier readvances on the Fildes Peninsula, King George Island, NW Antarctic Peninsula. The Holocene. <https://doi.org/10.31223/X59S7S>.
- Heroy DC, Sjunneskog C and Anderson JB. (2008) Holocene climate change in the Bransfield Basin, Antarctic Peninsula: evidence from sediment and diatom analysis. *Antarctic Science* 20: 69-87.
- Hochschild V. (1995) Geomorphologische Kartierung und Untersuchung der Auftaudynamik mit ERS-1-SAR-Daten im Bereich der Antarktischen Halbinsel. Bremen: Universität Bremen: Vertrieb, Universitätsbuchhandlung Bremen.
- Hodgson DA, Roberts SJ, Smith JA, et al. (2013) Late Quaternary environmental changes in Marguerite Bay, Antarctic Peninsula, inferred from lake sediments and raised beaches. *Quaternary Science Reviews* 68: 216-236.
- Hogg AG, Heaton TJ, Hua Q, Palmer JG, Turney CSM, Southon J, et al. (2020) SHCal20 Southern Hemisphere Calibration, 0–55,000 Years cal BP. *Radiocarbon* 62: 759-778.
- Hu Q-H, Sun L-G, Xie Z-Q, et al. (2013) Increase in penguin populations during the Little Ice Age in the Ross Sea, Antarctica. *Scientific Reports* 3: 2472.
- Hua Q, Barbetti M, and Rakowski AZ (2013). Atmospheric radiocarbon for the period 1950-2010. *Radiocarbon* 55, 1–14.
- Hughes, P.D., Gibbard, P.L., and Ehlers, J. (2013). Timing of glaciation during the last glacial cycle: evaluating the concept of a global 'Last Glacial Maximum' (LGM). *Earth-Science Reviews* 125: 171-198.
- Ingólfsson Ó, Hjort C and Humlum O. (2003) Glacial and Climate History of the Antarctic Peninsula since the Last Glacial Maximum. *Arctic, Antarctic, and Alpine Research* 35: 175-186.
- Jeong GY. (2006) Radiocarbon ages of sorted circles on King George Island, South Shetland Islands, West Antarctica. *Antarctic Science* 18: 265-270.
- Jerosch K, Pehlke H, Monien P, Scharf F, Weber L, Kuhn G, Braun MH, Abele D. 2018. Benthic meltwater fjord habitats formed by rapid glacier recession on King George Island, Antarctica. *Philosophical Transactions of the Royal Society A: Mathematical, Physical and Engineering Sciences* 376: 20170178.
- John BS and Sugden DE. (1971) Raised marine features and phases of glaciation in the South Shetland Islands. *British Antarctic Survey Bulletin* 24: 45-111.
- Johnson JS, Venturelli RA, Balco G, Allen CS, Braddock S, Campbell S, et al. (2022) Review article: Existing and potential evidence for Holocene grounding line retreat and readvance in Antarctica. *The Cryosphere* 16: 1543-1562.
- Juggins S. (2007) C2 Version 1.5 User Guide. Software for ecological and palaeoecological data analysis and visualisation. Newcastle University.
- Juggins S. (2012) Rioja: Analysis of Quaternary Science Data, R package version (0.8-5).
- Kääb A. (2007) Rock glaciers and protalus forms. In: Elias S (ed) *Encyclopedia of Quaternary Science*. Amsterdam: Elsevier, 2236-2242.
- Kaplan, M.R., Schaefer, J.M., Strelin, J.A., Denton, G.H., Anderson, R.F., Vandergoes, M.J., Finkel, R.C., Schwartz, R., Travis, S.G., Garcia, J.L., Martini, M.A., and Nielsen, S.H.H. (2016). Patagonian and southern South Atlantic view of Holocene climate. *Quaternary Science Reviews* 141: 112-125.
- Kaplan MR, Strelin JA, Schaefer JM, et al. (2020) Holocene glacier behaviour around the northern Antarctic Peninsula and possible causes. *Earth and Planetary Science Letters* 534: 116077.
- Kaufman D, McKay N, Routson C, et al. (2020) A global database of Holocene paleotemperature records. *Scientific Data* 7: 115.
- Kejna M, Arażny A and Sobota I. (2013) Climatic change on King George Island in the years 1948–2011. *Polish Polar Research* 34: 213-235.
- Klages JP, Kuhn G, Hillenbrand CD, et al. (2013) First geomorphological record and glacial history of an inter-ice stream ridge on the West Antarctic continental shelf. *Quaternary Science Reviews* 61: 47-61.

- Kraus S and del Valle R. (2008a) Geology, tectonics and Ar–Ar ages of the magmatic dykes from Potter Peninsula (King George Island, South Shetland Islands). In: Wiencke C, Ferreyra GA, Abele D, et al. (eds) *The Antarctic Ecosystem of Potter Cove, King– George Island (Isla 25 de Mayo): Synopsis of Research performed*. Bremerhaven, Germany: Alfred Wegener Institut für Polar- und Meeresforschung, Helmholtz Gemeinschaft, 20-30.
- Kraus S and del Valle R. (2008b) Geological map of Potter Peninsula (King George Island, South Shetland Islands, Antarctic Peninsula). Instituto Antártico Chileno, Punta Arenas, Chile & Instituto Antártico Argentino, Buenos Aires, Argentina. 10.1594/PANGAEA.667386.
- Kylander ME, Ampel L, Wohlfarth B, et al. (2011) High-resolution X-ray fluorescence core scanning analysis of Les Echets (France) sedimentary sequence: new insights from chemical proxies. *Journal of Quaternary Science* 26: 109-117.
- Lal D. (1991) Cosmic ray labelling of erosion surfaces: in situ nuclide production rates and erosion models. *Earth and Planetary Science Letters* 104: 424-439.
- Lamy F, Kilian R, Arz HW, et al. (2010) Holocene changes in the position and intensity of the southern westerly wind belt. *Nature Geoscience* 3: 695-699.
- Laskar J, Robutel P, Joutel F, et al. (2004) A long-term numerical solution for the insolation quantities of the Earth. *A&A* 428: 261-285.
- Leavitt PR and Hodgson DA. (2001) Sedimentary Pigments. In: Smol JP, Birks HJB, Last WM, et al. (eds) *Tracking Environmental Change Using Lake Sediments: Terrestrial, Algal, and Siliceous Indicators*. Dordrecht: Springer Netherlands, 295-325.
- Lifton N, Sato T and Dunai TJ. (2014) Scaling in situ cosmogenic nuclide production rates using analytical approximations to atmospheric cosmic-ray fluxes. *Earth and Planetary Science Letters* 386: 149-160.
- Lindhorst S and Schutter I. (2014) Polar gravel beach-ridge systems: Sedimentary architecture, genesis, and implications for climate reconstructions (South Shetland Islands/Western Antarctic Peninsula). *Geomorphology* 221: 187-203.
- Liu XD, Sun LG, Xie ZQ, et al. (2005) A 1300-year record of penguin populations at Ardley Island in the Antarctic, as deduced from the geochemical data in the ornithogenic lake sediments. *Arctic Antarctic and Alpine Research* 37: 490-498.
- López-Martínez J, Serrano E, Schmid T, et al. (2012) Periglacial processes and landforms in the South Shetland Islands (northern Antarctic Peninsula region). *Geomorphology* 155–156: 62-79.
- Lukas S. (2011) Ice-Cored Moraines. In: Singh VP, Singh P and Haritashya UK (eds) *Encyclopedia of Snow, Ice and Glaciers*. Dordrecht: Springer Netherlands, 616-619.
- Majewski W, Wellner JS, Szczuciński W, et al. (2012) Holocene oceanographic and glacial changes recorded in Maxwell Bay, West Antarctica. *Marine Geology* 326–328: 67-79.
- Makri S, Rey F, Gobet E, et al. (2020) Early human impact in a 15,000-year high-resolution hyperspectral imaging record of paleoproduction and anoxia from a varved lake in Switzerland. *Quaternary Science Reviews* 239: 106335.
- Mann ME, Zhang Z, Rutherford S, et al. (2009) Global Signatures and Dynamical Origins of the Little Ice Age and Medieval Climate Anomaly. *Science* 326: 1256-1260.
- Marrero SM, Phillips FM, Borchers B, Lifton N, Aumer R and Balco G. (2016) Cosmogenic nuclide systematics and the CRONUScal program. *Quaternary Geochronology* 31: 160-187.
- Marshall GJ. (2007) Half-century seasonal relationships between the Southern Annular mode and Antarctic temperatures. *International Journal of Climatology* 27: 373-383.
- Marshall GJ, Thompson DWJ and van den Broeke MR. (2017) The Signature of Southern Hemisphere Atmospheric Circulation Patterns in Antarctic Precipitation. *Geophysical Research Letters* 44: 11,580-11,589.
- Matsuoka N. (2001) Solifluction rates, processes and landforms: a global review. *Earth-Science Reviews* 55: 107-134.
- Mäusbacher R, Müller J and Schmidt R. (1989) Evolution of postglacial sedimentation in Antarctic lakes (King George Island). *Zeitschrift für Geomorphologie* 33: 219–234.

- Mercer JH. (1961) The response of fjord glaciers to changes in the firn limit. *Journal of Glaciology* 3: 850-858.
- Meredith MP and King JC. (2005) Rapid climate change in the ocean west of the Antarctic Peninsula during the second half of the 20th century. *Geophysical Research Letters* 32: L19604.
- Milliken KT, Anderson JB, Wellner JS, et al. (2009) High-resolution Holocene climate record from Maxwell Bay, South Shetland Islands, Antarctica. *Geological Society of America Bulletin* 121: 1711-1725.
- Moreno PI, Vilanova I, Villa-Martínez R, Dunbar RB, Mucciarone DA, Kaplan MR, et al. (2018) Onset and Evolution of Southern Annular Mode-Like Changes at Centennial Timescale. *Scientific Reports* 8: 3458.
- Monien P, Schnetger B, Brumsack H-J, et al. (2011) A geochemical record of late Holocene palaeoenvironmental changes at King George Island (maritime Antarctica). *Antarctic Science* 23: 255-267.
- Monien D, Monien P, Brünjes R, Widmer T, Kappenberg A, Silva Busso AA, Schnetger B, Brumsack H-J (2017) Meltwater as a source of potentially bioavailable iron to Antarctica waters. *Antarctic Science* 29: 277-291.
- Mulvaney R, Abram NJ, Hindmarsh RCA, et al. (2012) Recent Antarctic Peninsula warming relative to Holocene climate and ice-shelf history. *Nature* 489: 141-144.
- Munoz YP and Wellner JS. (2018) Seafloor geomorphology of western Antarctic Peninsula bays: a signature of ice flow behaviour. *The Cryosphere* 12: 205-225.
- Nývlt D, Glasser NF, Hocking E, Oliva M, Roberts SJ, and Roman M., et al. (2020) Chapter 5 - Tracing the deglaciation since the Last Glacial Maximum. In: Oliva M and Ruiz-Fernández J (eds) *Past Antarctica*. Academic Press, 89-107.
- Ó Cofaigh C, Davies BJ, Livingstone SJ, et al. (2014) Reconstruction of ice-sheet changes in the Antarctic Peninsula since the Last Glacial Maximum. *Quaternary Science Reviews* 100: 87-110.
- Oksanen J. (2014) Vegan: Community Ecology Package. R package version 2.3-0. <http://cran.r-project.org/web/packages/vegan/index.html>.
- Oliva M and Ruiz-Fernández J. (2017) Geomorphological processes and frozen ground conditions in Elephant Point (Livingston Island, South Shetland Islands, Antarctica). *Geomorphology* 293: 368-379.
- Oliva M, Antoniades D, Giralt S, et al. (2016a) La deglaciación de las áreas libres de hielo de las islas Shetland del Sur (Antártida). Ejemplos de Byers (Livingston) y Barton (King George). *Cuaternario y Geomorfología*: 14.
- Oliva M, Antoniades D, Giralt S, et al. (2016b) The Holocene deglaciation of the Byers Peninsula (Livingston Island, Antarctica) based on the dating of lake sedimentary records. *Geomorphology* 261: 89-102.
- Oliva M, Navarro F, Hrbáček F, et al. (2017) Recent regional climate cooling on the Antarctic Peninsula and associated impacts on the cryosphere. *Science of The Total Environment* 580: 210-223.
- Oliva M, Antoniades D, Serrano E, et al. (2019) The deglaciation of Barton Peninsula (King George Island, South Shetland Islands, Antarctica) based on geomorphological evidence and lacustrine records. *Polar Record* 55: 177-188.
- Oliva M, Mercier D, Ruiz-Fernández J, et al. (2020) Paraglacial processes in recently deglaciated environments. *Land Degradation & Development* 31: 1871-1876.
- Osmanoğlu B, Braun M, Hock R, et al. (2013) Surface velocity and ice discharge of the ice cap on King George Island, Antarctica. *Annals of Glaciology* 54: 111-119.
- Palacios D, Ruiz-Fernández J, Oliva M, Andrés N, Fernández-Fernández JM, Schimmelpfennig I, et al. (2020) Timing of formation of neoglacial landforms in the South Shetland Islands (Antarctic Peninsula): Regional and global implications. *Quaternary Science Reviews* 234: 106248.

- Pallàs R, James T, Sàbat F, Vilaplana J, Grant D and Ricci C. (1997) Holocene uplift in the South Shetland Islands: evaluation of tectonics and glacio-isostasy. In: Ricci C (ed) *The Antarctic Region: Geological Evolution and Processes*. Siena, Italy: Terra Antarctica Publication, 861–868.
- Parnell AC. (2021) Bchron: Radiocarbon Dating, Age-Depth Modelling, Relative Sea Level Rate Estimation, and Non-Parametric Phase Modelling. <https://github.com/andrewcparnell/Bchron/>.
- Pasotti F, Manini E, Giovannelli D, et al. (2015a) Antarctic shallow water benthos in an area of recent rapid glacier retreat. *Marine Ecology* 36: 716-733.
- Pasotti F, Saravia LA, De Troch M, et al. (2015b) Benthic Trophic Interactions in an Antarctic Shallow Water Ecosystem Affected by Recent Glacier Retreat. *PLoS ONE* 10: e0141742.
- Pearson EJ, Juggins S, Talbot HM, Weckström J, Rosén P, Ryves DB, et al. (2011) A lacustrine GDGT-temperature calibration from the Scandinavian Arctic to Antarctic: Renewed potential for the application of GDGT-paleothermometry in lakes. *Geochimica et Cosmochimica Acta* 75: 6225-6238.
- Peck VL, Allen CS, Kender S, et al. (2015) Oceanographic variability on the West Antarctic Peninsula during the Holocene and the influence of upper circumpolar deep water. *Quaternary Science Reviews* 119: 54-65.
- Perren B, Hodgson DA, Roberts SJ, et al. (2020) Southward migration of the Southern Hemisphere westerly winds corresponds with warming climate over centennial timescales. *Communications Earth & Environment* 1(1): 58.
- Quade, J., and Kaplan, M.R. (2017). Lake-level stratigraphy and geochronology revisited at Lago (Lake) Cardiel, Argentina, and changes in the Southern Hemispheric Westerlies over the last 25 ka. *Quaternary Science Reviews* 177: 173-188.
- Quartino ML, Deregibus D, Campana GL, et al. (2013) Evidence of macroalgal colonization on newly ice-free areas following glacial retreat in Potter Cove (South Shetland Islands), Antarctica. *PLoS ONE* 8: e58223.
- Reimer RW, and Reimer PJ. (2004). CALIBomb - calibration of post-bomb C-14 data (www.calib.org).
- Rein B and Sirocko F. (2002) In-situ reflectance spectroscopy – analysing techniques for high-resolution pigment logging in sediment cores. *International Journal of Earth Sciences* 91: 950-954.
- Reynhout SA, Sagredo EA, Kaplan MR, et al. (2019) Holocene glacier fluctuations in Patagonia are modulated by summer insolation intensity and paced by Southern Annular Mode-like variability. *Quaternary Science Reviews* 220: 178-187.
- Roberts SJ, Hodgson DA, Shelley S, et al. (2010) Establishing Lichenometric Ages for Nineteenth- and Twentieth-Century Glacier Fluctuations on South Georgia (South Atlantic). *Geografiska Annaler Series a-Physical Geography* 92A: 125-139.
- Roberts SJ, Hodgson DA, Sterken M, et al. (2011) Geological constraints on glacio-isostatic adjustment models of relative sea-level change during deglaciation of Prince Gustav Channel, Antarctic Peninsula. *Quaternary Science Reviews* 30: 3603-3617.
- Roberts SJ, Monien P, Foster LC, et al. (2017) Past penguin colony responses to explosive volcanism on the Antarctic Peninsula. *Nature Communications* 8: 14914.
- Roberts SJ, McCulloch RD, Emmings JF, Davies SJ, Van Nieuwenhuyze W, Sterken M, et al. (2022) Late Glacial and Holocene Palaeolake History of the Última Esperanza Region of Southern Patagonia. *Frontiers in Earth Science* 10. doi:10.3389/feart.2022.813396
- Rückamp M, Blindow N, Suckro S, et al. (2010) Dynamics of the ice cap on King George Island, Antarctica: field measurements and numerical simulations. *Annals of Glaciology* 51: 80-90.
- Rückamp M, Braun M, Suckro S, et al. (2011) Observed glacial changes on the King George Island ice cap, Antarctica, in the last decade. *Global and Planetary Change* 79: 99-109.
- Ruiz-Fernández, J., Oliva, M., Nývlt, D., Cannone, N., García-Hernández, C., Guglielmin, M., Hrbáček, F., Roman, M., Fernández, S., López-Martínez, J., and Antoniades, D. (2019).

- Patterns of spatio-temporal paraglacial response in the Antarctic Peninsula region and associated ecological implications. *Earth-Science Reviews* 192: 379-402.
- Sahade R, Lagger C, Torre L, et al. (2015) Climate change and glacier retreat drive shifts in an Antarctic benthic ecosystem. *Science Advances* 1:e1500050.
- Sánchez-Lugo A, Morice C, Berrisford P, and Argüez A, et al. (2018) Global surface temperatures. In: Blunden J, Arndt DS and Hartfield G (eds) *State of the Climate in 2017. Bulletin of the American Meteorological Society* 99 (8): 11-13.
- Saunders KM, Roberts SJ, Perren B, et al. (2018) Holocene dynamics of the Southern Hemisphere westerly winds and possible links to CO₂ outgassing. *Nature Geoscience* 11: 650-655.
- Schneider T, Rimer D, Butz C, et al. (2018) A high-resolution pigment and productivity record from the varved Ponte Tresa basin (Lake Lugano, Switzerland) since 1919: insight from an approach that combines hyperspectral imaging and high-performance liquid chromatography. *Journal of Paleolimnology* 60: 381-398.
- Seong YB, Owen LA, Lim HS, et al. (2008) Rate of late Quaternary ice-cap thinning on King George Island, South Shetland Islands, West Antarctica defined by cosmogenic ³⁶Cl surface exposure dating. *Boreas* 38: 207-213.
- Serrano E and López-Martínez J. (2000) Rock glaciers in the South Shetland Islands, Western Antarctica. *Geomorphology* 35: 145-162.
- Serrano E, Giner J, Gumiel P, et al. (2012) El glaciar rocoso de Hurd: Estructura e inserción en el sistema de transferencia de derrubios Antártico Marítimo (Isla Livingston, Islas Shetland de Sur, Antártida). *Cuaternario y Geomorfología* 18: 13-25.
- Shevenell AE, Ingalls AE, Domack EW, et al. (2011) Holocene Southern Ocean surface temperature variability west of the Antarctic Peninsula. *Nature* 470: 250-254.
- Simms AR, Milliken KT, Anderson JB, et al. (2011) The marine record of deglaciation of the South Shetland Islands, Antarctica since the Last Glacial Maximum. *Quaternary Science Reviews* 30: 1583-1601.
- Simms AR, Ivins ER, DeWitt R, et al. (2012) Timing of the most recent Neoglacial advance and retreat in the South Shetland Islands, Antarctic Peninsula: insights from raised beaches and Holocene uplift rates. *Quaternary Science Reviews* 47: 41-55.
- Simms AR, Bentley MJ, Simkins LM, Zurbuchen J, Reynolds LC, DeWitt R, et al. (2021) Evidence for a “Little Ice Age” glacial advance within the Antarctic Peninsula – Examples from glacially-overrun raised beaches. *Quaternary Science Reviews* 271: 107195.
- Smellie JL, Pankhurst R, Thomson M, et al. (1984) The geology of the South Shetland Islands: VI. Stratigraphy, geochemistry and evolution: British Antarctic Survey.
- Spada G, Bamber JL and Hurkmans RTWL. (2013) The gravitationally consistent sea-level fingerprint of future terrestrial ice loss. *Geophysical Research Letters* 40: 482-486.
- Steig EJ, Schneider DP, Rutherford SD, et al. (2009) Warming of the Antarctic ice-sheet surface since the 1957 International Geophysical Year. *Nature* 457: 459.
- Steinhilber F, Beer J and Fröhlich C. (2009) Total solar irradiance during the Holocene. *Geophysical Research Letters* 36: L19704.
- Stewart TG, Anderson JB, and Ashley GM. (1991) Glacial marine sedimentation from tidewater glaciers in the Canadian High Arctic. *Glacial marine sedimentation; Paleoclimatic significance*. Geological Society of America, 261: 10.1130/SPE261-p95.
- Strelin JA, Sone T, Mori J, et al. (2006) New Data Related to Holocene Landform Development and Climatic Change from James Ross Island, Antarctic Peninsula. In: Fütterer DK, Damaske D, Kleinschmidt G, et al. (eds) *Antarctica: Contributions to Global Earth Sciences*. Berlin, Heidelberg: Springer Berlin Heidelberg, p. 455-459.
- Strelin JA, Heredia Barión PA., Martini MA., Kaplan MM. Kuhn G. (2014) The age of the first Holocene marine transgression in Potter Cove, Isla 25 de Mayo (King George Island), South Shetland Islands. *Contributions to the XIX Congreso Geológico Argentino* Martino RD., Lira R., Guerreschi A., Baldo E., Franzese J., Krohling D., Manassero, M., Ortega G., Pinotti L., (eds) T1-51, Córdoba, Argentina, 455-459.

- Stone JO. (2000) Air pressure and cosmogenic isotope production. *Journal of Geophysical Research: Solid Earth* 105: 23753-23759.
- Strother SL, Salzmann U, Roberts SJ, et al. (2015) Changes in Holocene climate and the intensity of Southern Hemisphere Westerly Winds based on a high-resolution palynological record from sub-Antarctic South Georgia. *The Holocene* 25: 263-279.
- Sugden DE and John BS. (1973) The ages of glacier fluctuations in the South Shetland Islands, Antarctica. In: van Zinderen; Bakker EM (ed) *Palaeoecology of Africa, the Surrounding Islands and Antarctica*. Balkema, Cape Town, 141-159.
- Sun LG, Liu XD, Yin XB, et al. (2005) Sediments in palaeo-notches: potential proxy records for palaeoclimatic changes in Antarctica. *Palaeogeography Palaeoclimatology Palaeoecology* 218: 175-193.
- Thomas ER, Marshall GJ and McConnell JR. (2008) A doubling in snow accumulation in the western Antarctic Peninsula since 1850. *Geophysical Research Letters* 35: L01706, doi:10.1029/2007GL032529.
- Toro M, Granados I, Pla S, Giralt S, Antoniades D, Galán L, et al. (2013) Chronostratigraphy of the sedimentary record of Limnopolar Lake, Byers Peninsula, Livingston Island, Antarctica. *Antarctic Science* 25: 198-212.
- Turner J, Lachlan-Cope TA, Marshall GJ, et al. (2002) Spatial variability of Antarctic Peninsula net surface mass balance. *Journal of Geophysical Research: Atmospheres* 107: AAC 4-1-AAC 4-18.
- Turner J, Lu H, White I, et al. (2016) Absence of 21st century warming on Antarctic Peninsula consistent with natural variability. *Nature* 535: 411-415.
- van der Bilt WGM, Bakke J, Werner JP, et al. (2017) Late Holocene glacier reconstruction reveals retreat behind present limits and two-stage Little Ice Age on subantarctic South Georgia. *Journal of Quaternary Science* 32: 888-901.
- van der Veen CJ. (1995) Controls on calving rate and basal sliding: observations from Columbia Glacier, Alaska, prior to and during its rapid retreat, 1976–1993. *Byrd Polar Research Center Report* 11.
- Varma V, Prange M, Spanghel T, et al. (2012) Impact of solar-induced stratospheric ozone decline on Southern Hemisphere westerlies during the Late Maunder Minimum. *Geophysical Research Letters* 39: L20704.
- Vaughan DG, Marshall GJ, Connolley WM, et al. (2003) Recent Rapid Regional Climate Warming on the Antarctic Peninsula. *Climatic Change* 60: 243-274.
- Vaughan DG, Comiso JC, Allison I, et al. (2013) Observations: Cryosphere. In: Stocker TF, Qin D, Plattner G-K, et al. (eds) *Climate Change 2013: The Physical Science Basis. Contribution of Working Group I to the Fifth Assessment Report of the Intergovernmental Panel on Climate Change*. Cambridge, United Kingdom and New York, NY, USA: Cambridge University Press, 317–382.
- Verfaillie D, Charton J, Schimmelpfennig I, et al. (2021) Evolution of the Cook Ice Cap (Kerguelen Islands) between the last centuries and ice based on cosmogenic dating and glacio-climatic modelling. *Antarctic Science* 33: 301-317.
- Wang G and Cai W. (2013) Climate-change impact on the 20th-century relationship between the Southern Annular Mode and global mean temperature. *Scientific Reports* 3: 2039.
- Watcham EP, Bentley MJ, Hodgson DA, et al. (2011) A new Holocene relative sea level curve for the South Shetland Islands, Antarctica. *Quaternary Science Reviews* 30: 3152-3170.
- Whitehouse PL, Bentley MJ and Le Brocq AM. (2012a) A deglacial model for Antarctica: geological constraints and glaciological modelling as a basis for a new model of Antarctic glacial isostatic adjustment. *Quaternary Science Reviews* 32: 1-24.
- Whitehouse PL, Bentley MJ, Milne GA, King MA and Thomas ID. (2012b) A new glacial isostatic adjustment model for Antarctica: calibrated and tested using observations of relative sea-level change and present-day uplift rates. *Geophysical Journal International* 190: 1464-1482.
- Wichard T, Mishra B, Myneni SCB, et al. (2009) Storage and bioavailability of molybdenum in soils increased by organic matter complexation. *Nature Geoscience* 2: 625-629.

- Weatherall P, Marks KM, Jakobsson M, et al. (2015) A new digital bathymetric model of the world's oceans. *Earth and Space Science* 2: 331-345.
- Wöfl A-C, Wittenberg N, Feldens P, et al. (2016) Submarine landforms related to glacier retreat in a shallow Antarctic fjord. *Antarctic Science*: 28, 475-486.
- Yang L, Gao Y, Sun L, et al. (2019) Enhanced westerlies drove penguin movement at 1000 yr BP on Ardley Island, west Antarctic Peninsula. *Quaternary Science Reviews* 214: 44-53.
- Yoon HI, Yoo K-C, Park B-K, et al. (2004) The origin of massive diamicton in Marian and Potter coves, King George Island, West Antarctica. *Geosciences Journal* 8: 1-10.
- Zervas D, Nichols GJ, Hall R, et al. (2009) SedLog: A shareware program for drawing graphic logs and log data manipulation. *Computers & Geosciences* 35: 2151-2159.
- Zervas, D., Nichols, G.J., Hall, R., Smyth, H.R., Lüthje, C., and Murtagh, F. (2009). SedLog: A shareware program for drawing graphic logs and log data manipulation. *Computers & Geosciences* 35, 2151-2159.